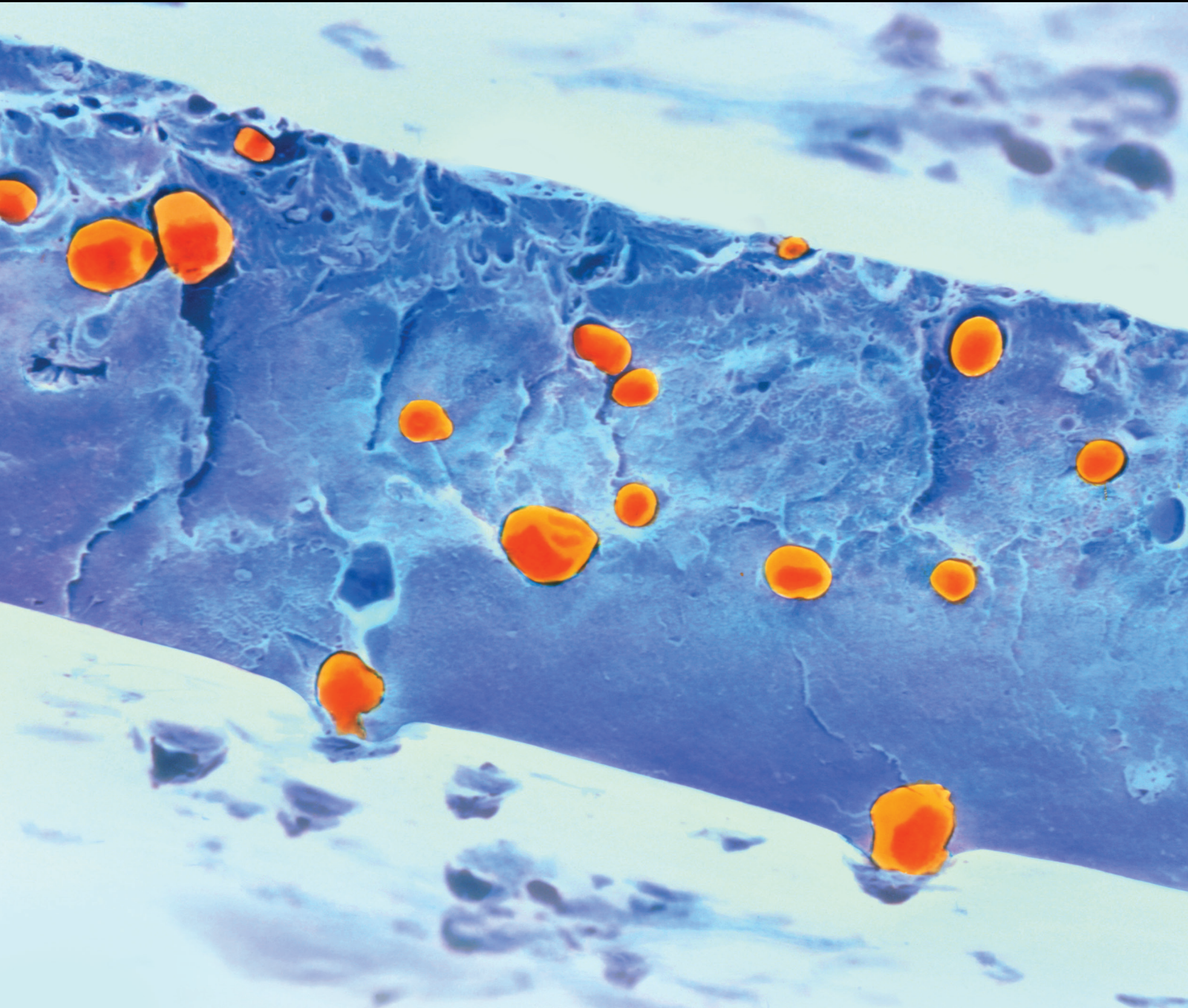


Applications of Fiber Reinforced Polymer Composites

Guest Editors: Togay Ozbakkaloglu, Jian-Fei Chen, Scott T. Smith,
and Jian-Guo Dai





Applications of Fiber Reinforced Polymer Composites

International Journal of Polymer Science

Applications of Fiber Reinforced Polymer Composites

Guest Editors: Togay Ozbakkaloglu, Jian-Fei Chen,
Scott T. Smith, and Jian-Guo Dai



Copyright © 2016 Hindawi Publishing Corporation. All rights reserved.

This is a special issue published in "International Journal of Polymer Science." All articles are open access articles distributed under the Creative Commons Attribution License, which permits unrestricted use, distribution, and reproduction in any medium, provided the original work is properly cited.

Editorial Board

Domenico Acierno, Italy
Sharif Ahmad, India
Mats R. Andersson, Australia
Luc Averous, France
Massimiliano Barletta, Italy
Christopher Batich, USA
Giuseppe Battaglia, UK
Marc Behl, Germany
Laurent Billon, France
David G. Bucknall, USA
Andrea Camposeo, Italy
Wen Shyang Chow, Malaysia
Jesper Christiansen, Denmark
Yoshiki Chujo, Japan
Angel Concheiro, Spain
Marek Cypryk, Poland
Li Ming Dai, USA
Yulin Deng, USA
Maria Laura Di Lorenzo, Italy
Eliane Espuche, France
Antonio Facchetti, USA
Marta Fernández-García, Spain
Benny Dean Freeman, USA
Jean-François Gérard, France
Peng He, USA
Jan-Chan Huang, USA
Wei Huang, China
Nabil Ibrahim, Egypt
Tadashi Inoue, Japan
Avraam I. Isayev, USA

Koji Ishizu, Japan
Tadahisa Iwata, Japan
Patric Jannasch, Sweden
Nobuhiro Kawatsuki, Japan
J.M. Kenny, Italy
Mubarak A. Khan, Bangladesh
Ruhul A. Khan, Canada
Saad Khan, USA
Jui-Yang Lai, Taiwan
Jose Ramon Leiza, Spain
Guiping Ma, China
Evangelos Manias, USA
Ulrich Maschke, France
Jani Matisons, Australia
Geoffrey R. Mitchell, UK
Subrata Mondal, India
Christian B. Nielsen, UK
Toribio F. Otero, Spain
Qinmin Pan, Canada
Alessandro Pegoretti, Italy
"Onder Pekcan, Turkey
Zhonghua Peng, USA
Beng T. Poh, Malaysia
Antje Potthast, Austria
Debora Puglia, Italy
Miriam Rafailovich, USA
Arthur J. Ragauskas, USA
Subramaniam Ramesh, Malaysia
Bernabé Luis Rivas, Chile
Juan Rodriguez-Hernandez, Spain

Hossein Roghani-Mamaqani, Iran
Pietro Russo, Italy
Jean-Marc Saiter, France
Mehdi Salami-Kalajahi, Iran
Erol Sancaktar, USA
Albert P. H. J. Schenning, Netherlands
Matthias Schnabelrauch, Germany
Shu Seki, Japan
Vitor Sencadas, Australia
Robert A Shanks, Australia
Mikhail Shtilman, Russia
Basavarajaiah Siddaramaiah, India
Dennis W. Smith Jr., USA
Atsushi Sudo, Japan
Kohji Tashiro, Japan
Hideto Tsuji, Japan
Masaki Tsuji, Japan
Stefano Turri, Italy
Hiroshi Uyama, Japan
Cornelia Vasile, Romania
Alenka Vesel, Slovenia
Yakov S. Vygodskii, Russia
De-Yi Wang, Spain
Qinglin Wu, USA
Frederik Wurm, Germany
Huining Xiao, Canada
Yiqi Yang, USA
Long Yu, Australia
Philippe Zinck, France

Contents

Applications of Fiber Reinforced Polymer Composites

Togay Ozbakkaloglu, Jian-Fei Chen, Scott T. Smith, and Jian-Guo Dai
Volume 2016, Article ID 5804145, 1 page

Flexural Strength of Carbon Fiber Reinforced Polymer Repaired Cracked Rectangular Hollow Section Steel Beams

Tao Chen, Ming Qi, Xiang-Lin Gu, and Qian-Qian Yu
Volume 2015, Article ID 204861, 9 pages

Development of Ecoefficient Engineered Cementitious Composites Using Supplementary Cementitious Materials as a Binder and Bottom Ash Aggregate as Fine Aggregate

Jin Wook Bang, G. Ganesh Prabhu, Yong Il Jang, and Yun Yong Kim
Volume 2015, Article ID 681051, 12 pages

Application of a Neural Network Model for Prediction of Wear Properties of Ultrahigh Molecular Weight Polyethylene Composites

Halil Ibrahim Kurt and Murat Oduncuoglu
Volume 2015, Article ID 315710, 11 pages

High-Density Polyethylene and Heat-Treated Bamboo Fiber Composites: Nonisothermal Crystallization Properties

Yanjun Li, Lanxing Du, Zhen Zhang, and Qinglin Wu
Volume 2015, Article ID 658584, 7 pages

Carbon Fiber Composites of Pure Polypropylene and Maleated Polypropylene Blends Obtained from Injection and Compression Moulding

D. Pérez-Rocha, A. B. Morales-Cepeda, F. Navarro-Pardo, T. Lozano-Ramírez, and P. G. LaFleur
Volume 2015, Article ID 493206, 8 pages

Parametric Study on Dynamic Response of Fiber Reinforced Polymer Composite Bridges

Woraphot Prachasaree, Attapon Sangkaew, Suchart Limkatanyu, and Hota V. S. GangaRao
Volume 2015, Article ID 565301, 13 pages

Editorial

Applications of Fiber Reinforced Polymer Composites

Togay Ozbakkaloglu,¹ Jian-Fei Chen,² Scott T. Smith,³ and Jian-Guo Dai⁴

¹University of Adelaide, Adelaide, SA 5005, Australia

²Queen's University Belfast, Belfast BT7 1NN, UK

³Southern Cross University, Lismore, NSW 2480, Australia

⁴Hong Kong Polytechnic University, Kowloon, Hong Kong

Correspondence should be addressed to Togay Ozbakkaloglu; togay.ozbakkaloglu@adelaide.edu.au

Received 19 January 2016; Accepted 20 January 2016

Copyright © 2016 Togay Ozbakkaloglu et al. This is an open access article distributed under the Creative Commons Attribution License, which permits unrestricted use, distribution, and reproduction in any medium, provided the original work is properly cited.

Fueled by the need to surpass the limitations of conventional materials, recent years have seen a large increase in engineering applications of advanced fiber reinforced polymer (FRP) composite materials in many major industries, such as aerospace and defense, automotive, construction, marine, and oil and gas. FRP composites are very attractive for these applications due to their highly favorable material properties, including high strength-to-weight and stiffness-to-weight ratios, and corrosion resistance. Studies conducted to date have demonstrated the numerous advantages offered by FRP composites in various engineering applications. However, there are still a number of technical and implementation issues that need to be resolved prior to broader uptake of the application of FRP composites by some engineering communities such as civil construction. This special issue is aimed at disseminating the most recent advances and developments in this exciting field.

A total of 17 papers were submitted to the special issue and after a rigorous peer-review process six of them were accepted to appear in the issue as original research articles. These six papers deal with a range of topics on the structural behavior of composite members/structures and mechanical properties and development of composite materials. The studies on the former investigate the dynamic behavior of composite FRP bridge systems and flexural behavior of previously damaged steel beams repaired with FRP. The studies on the latter are concerned with the development of ecoefficient engineered cementitious composites, mechanical properties of carbon fiber composites obtained using different molding

techniques, and properties of high-density and ultra-high molecular weight polyethylene and heat-treated bamboo fiber composites.

We hope that some of the most recent advances on the development and applications of FRP composites that have been disseminated in this special issue will be of interest to readers and contribute toward the advancement of research in the field.

Acknowledgments

We would like to thank all the authors for their contributions and reviewers for their valuable comments and suggestions.

*Togay Ozbakkaloglu
Jian-Fei Chen
Scott T. Smith
Jian-Guo Dai*

Research Article

Flexural Strength of Carbon Fiber Reinforced Polymer Repaired Cracked Rectangular Hollow Section Steel Beams

Tao Chen, Ming Qi, Xiang-Lin Gu, and Qian-Qian Yu

Department of Structural Engineering, Tongji University, Shanghai 200092, China

Correspondence should be addressed to Xiang-Lin Gu; gxl@tongji.edu.cn

Received 5 June 2015; Revised 20 September 2015; Accepted 29 September 2015

Academic Editor: Togay Ozbakkaloglu

Copyright © 2015 Tao Chen et al. This is an open access article distributed under the Creative Commons Attribution License, which permits unrestricted use, distribution, and reproduction in any medium, provided the original work is properly cited.

The flexural behavior of rectangular hollow section (RHS) steel beams with initial crack strengthened externally with carbon fiber reinforced polymer (CFRP) plates was studied. Eight specimens were tested under three-point loading to failure. The experimental program included three beams as control specimens and five beams strengthened with CFRP plates with or without prestressing. The load deflection curves were graphed and failure patterns were observed. The yield loads and ultimate loads with or without repairing were compared together with the strain distributions of the CFRP plate. It was concluded that yield loads of cracked beams could be enhanced with repairing. Meanwhile, the ultimate loads were increased to some extent. The effect of repair became significant with the increase of the initial crack depth. The failure patterns of the repaired specimens were similar to those of the control ones. Mechanical clamping at the CFRP plate ends was necessary to avoid premature peeling between the CFRP plate and the steel beam. The stress levels in CFRP plates were relatively low during the tests. The use of prestressing could improve the utilization efficiency of CFRP plates. It could be concluded that the patching repair could be used to restore the load bearing capacity of the deficient steel beams.

1. Introduction

Hollow section steel members have gained more widespread usage as load bearing in all directions and aesthetic appearance. They have been widely adopted as structural and nonstructural elements for onshore and offshore structures. Such existing steel structures are now facing the deficient loading bearing capacity due to corrosion, fatigue cracks, and increasing live loads. The conventional rehabilitation techniques are mainly externally bonding/welded steel plates. Steel plates showed their effectiveness in enhancing load bearing capacity. But they are cumbersome and prone to corrosion. More efficient retrofitting methods are required. Carbon fiber reinforced polymer (CFRP) patching method has become an attractive method due to its superior high strength, light weight, and lifetime properties. The technique was mainly used in the aviation industry and the effects were found to be effective [1, 2]. The method was extended to the repairing of damaged steel structures in civil engineering. Experimental tests and site applications [3–5] indicate that damaged steel structures patched by FRP can restore loading

bearing capacity. Tickford bridge [6] was repaired with composite materials to increase its bearing capacity. This was also achieved with experimental tests of steel beams strengthened with carbon fiber reinforced polymer (CFRP) plates [7].

However, only a limited amount of research has been focused on the flexural behavior of hollow section steel beams. Haedir et al. [8, 9] wrapped steel circular hollow section (CHS) beams with CFRP sheets. Pure bending test results indicated that the reinforcement was favorable to the bending strength. The strengthening technique was also extended to offshore tubular steel members. Six 2.4 m long steel tubes wrapped with CFRP composites were subjected to four-point bending test [10]. It was concluded that the ultimate bending strength and flexural stiffness were increased. Photiou et al. [11] compared two retrofitting systems for degraded rectangular hollow section steel beams. It was observed that the U-shaped system could prevent peel failure and was regarded as an efficient rehabilitation method in comparison with flat plate repairing system. Elchalakani [12] also conducted series tests on rectangular hollow section steel

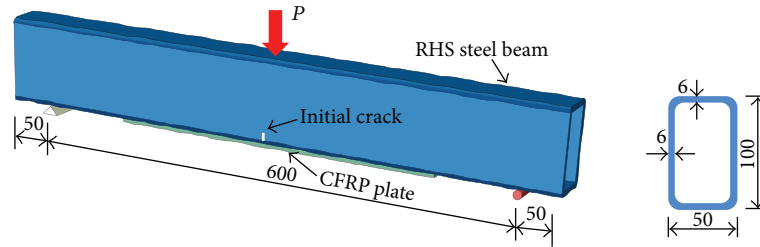


FIGURE 1: Geometry configurations.

beams wrapped with CFRP sheets or patched with CFRP plates. Both undegraded and artificially degraded beams were investigated. Considered parameters were reduction of thickness, section slenderness, and the amount of the CFRP materials. The strength increase ranges from 7% to 31% for degraded specimens. The previous research employed thinning areas to simulate the corrosion defects. However, cracks are usually found due to fatigue damage or other reasons. The defect of crack can also impair the bearing capacity and make the structures prone to brittle fracture. To restore the bearing capacity or retard crack propagation, CFRP plate was prestressed and patched to a steel pendulum with rectangular hollow section [13]. Scaled fatigue tests were conducted before the technique was applied to a site rehabilitation project. The long term field monitoring was carried out and results indicated that the patching repair was effective in mitigating stress around potential defects. Similar flat plate repairing system was also adopted by several researchers [14, 15].

In practice, hollow section members are suffering significant deterioration caused by the combination of external loading, corrosion, and cracking. Previous research has been focused on the strengthening of intact specimens or specimens with reduced thickness. Efforts have also been made to the strengthening of cracked RHS beams with a constant crack depth. Nevertheless, the specimens with different initial damage degrees have not been investigated. The knowledge gap should be fulfilled with regard to the strengthening effects on specimens with various crack depths. The purpose of this experimental study is to compare the performance of cracked rectangular hollow section (RHS) steel beams with various damage degrees repaired by CFRP plates or prestressed CFRP plates.

2. Experimental Program

2.1. Material Properties. The materials were steel tubes, CFRP, and adhesive. The steel tubes had nominal yield strength of 298 MPa and an ultimate strength of 368 MPa and the modulus of elasticity was 1.87×10^5 MPa by coupon test. It should be noted that the elastic modulus is relatively low for conventional steel. This might be due to manufacture process. The chemical compositions were listed in Table 1. The tensile strength of the CFRP plates with 1.4 mm thickness was 3089 MPa and elastic modulus was 1.91×10^5 MPa provided by the manufacturer. The two-component epoxy adhesives

TABLE 1: Chemical compositions of steel (%).

C	Mn	Si	P	S
0.13–0.18	0.42–0.46	0.16–0.24	0.014–0.026	0.027–0.040

were mixed with a proportion of 2.5 : 1. The two-component epoxy adhesive was mixed with a proportion of 2.5 : 1. It was supplied by Shanghai Yichang Carbon Fiber Material Co., Ltd. The tensile strength and elastic modulus were 40 MPa and 2500 MPa, respectively.

2.2. Test Specimens. A total of eight steel beams with rectangular hollow section (RHS) were designed with various depths of initial crack. Considering workability and test facility at laboratory, the length of the specimen was chosen as 700 mm and the effective span was 600 mm for a three-point bending test. The cross section of RHS is 100 mm \times 50 mm \times 6 mm. The basic geometry of the cracked RHS steel beams and test setup is shown in Figure 1. Initial crack was cut on the bottom of the beam for simulating different damage degrees. The depths, which were cut with saw, were 3 mm, 6 mm, and 30 mm, respectively. The specimens were classified as three groups. Three beams were not repaired and were used as control beams. Another three beams were repaired with CFRP plates without prestressing. Two beams were patched with prestressed CFRP plates. With regard to nonprestressed CFRP plate repaired specimens, one CFRP plate with length of 400 mm and width of 50 mm was positioned and applied on the bottom of a specimen without prestressing. With regard to prestressed CFRP plate repaired specimens, one CFRP plate with length of 400 mm and width of 40 mm was patched to the specimen subjected to a prestress of 10% of the ultimate tensile strength of CFRP material. Full details of all the specimens are given in Table 2.

2.3. Specimen Preparation. The specimen preparation involved surface preparation, applying adhesives and patching CFRP plates. Proper surface preparation of the steel substrate is crucial to the bonding between the steel and the CFRP plate. In this study, bottom surfaces were ground with an abrasive disk to remove rust and get chemically active steel surface [16, 17]. Then surfaces were cleaned with acetone to remove dust and grease. The two-part epoxy adhesive was then mixed and uniformly spread over both the steel surface and the CFRP plate. The CFRP plate was patched to the steel

TABLE 2: Details of specimens.

Test groups	Specimen number	CFRP plate (layers)	Initial crack depth (mm)	Prestressed level (%)	Anchorage
I	RHS-I-03	0	3	—	—
	RHS-I-06	0	6	—	—
	RHS-I-30	0	30	—	—
II	RHS-II-03-P0	1	3	0	—
	RHS-II-06-P0	1	6	0	Type A
	RHS-II-30-P0	1	30	0	Type A
III	RHS-III-06-P10	1	6	10	Type B
	RHS-III-30-P10	1	30	10	Type B

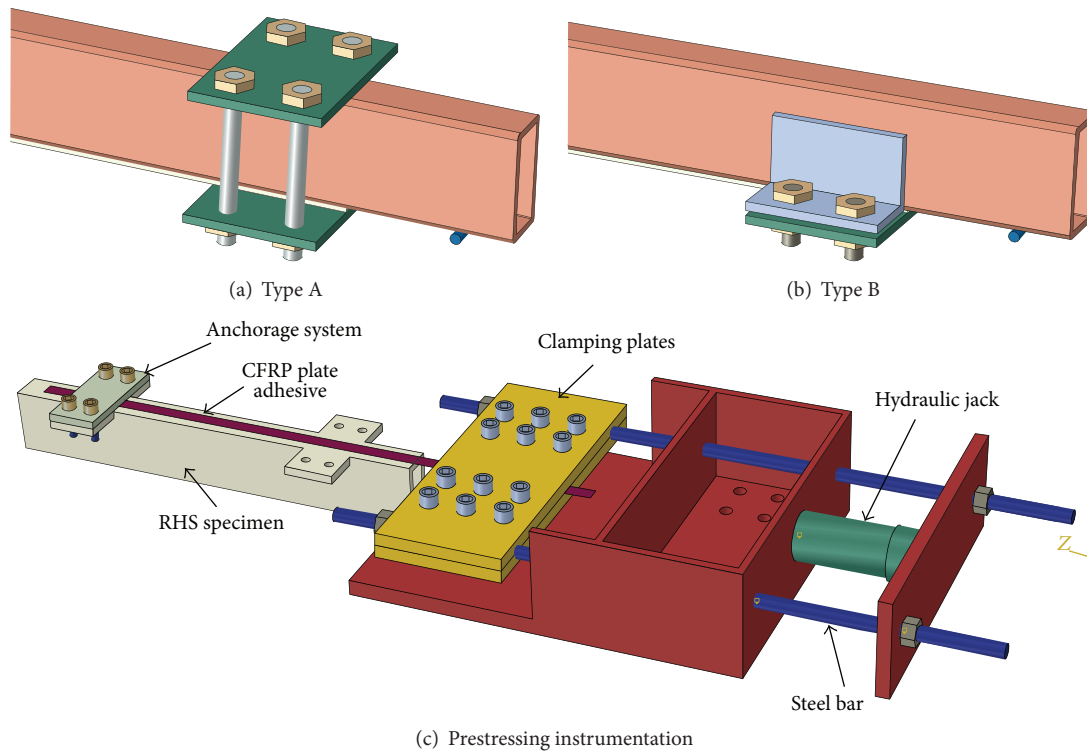


FIGURE 2: Anchorage systems and prestressing instrumentation.

surface with a controlled adhesive thickness. All of the test specimens were cured for more than one week under ambient temperature. To delay or prevent debonding of bonded CFRP plates, two anchorage systems were used for strengthened specimens, as shown in Figures 2(a) and 2(b). For type A, the CFRP plate end was clamped by two identical steel plates connected with four bolts. For type B, L shape angles were welded to the tube, and, thereafter, a steel cover plate was screwed to clamp the CFRP plate.

Figure 2(c) illustrates the prestressing instrumentation for the prestressed CFRP repaired specimens. Firstly, the CFRP plate was cleaned and fixed at one end by the anchorage system. The other end was clamped by two steel plates that connected to the far end steel plate through two steel bars. A hydraulic jack was used to fulfill the prestressing force. Meanwhile, a load cell and strain gauges were adopted to

monitor the stress level to the controlled values. After that, the bolts were screwed at the other end of the specimen. The specimens were cured for more than one week under ambient temperature.

2.4. Instrumentation and Test Setup. The beams were tested with a three-point loading system as shown in Figure 3. The flexural loading was applied by imposing statically loading with a 500 kN hydraulic ram in the middle of the specimen. Load interval was determined with nominal yield bending moment. When the load-displacement curve exhibited nonlinear characteristic, the displacement controlled loading method was adopted until failure.

The deflections at middle point were monitored using three linear variable displacement transducers (LVDTs). Strain gauges were mounted along the height direction in

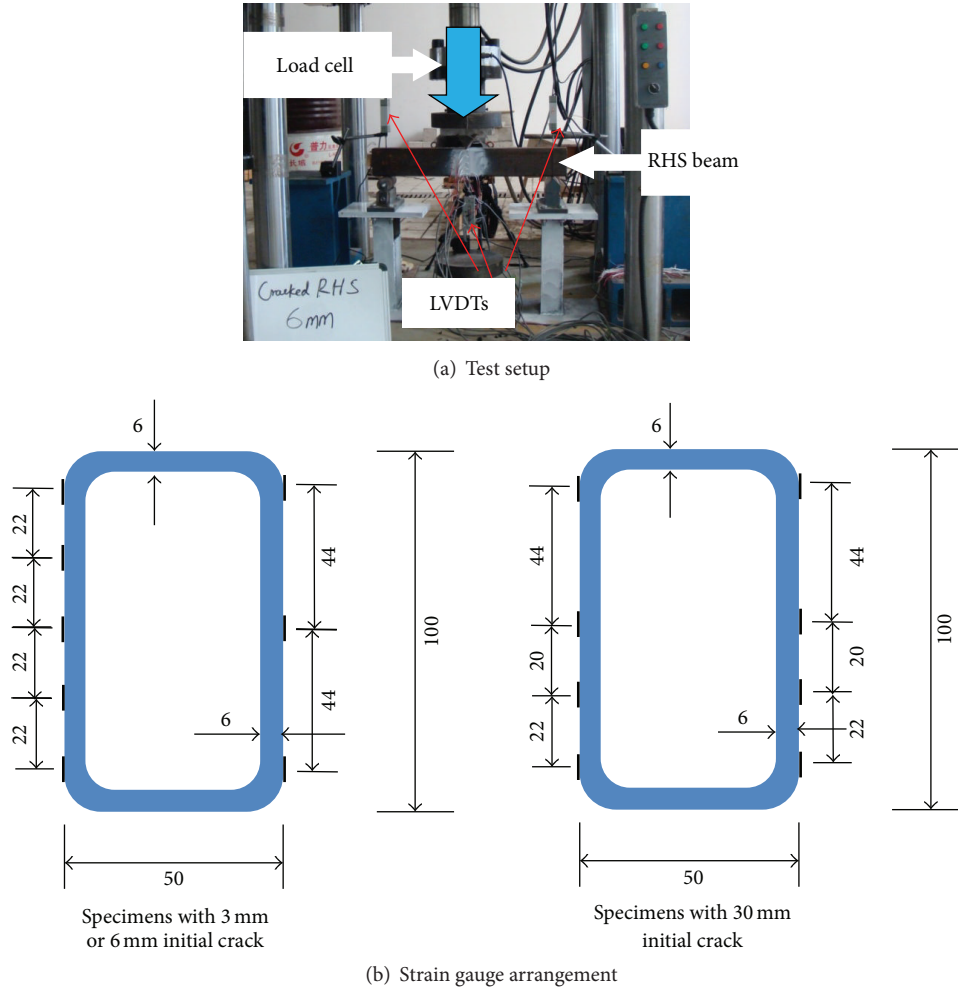


FIGURE 3: Test setup and instrumentation.

the middle span to examine the strain distribution of the cross section, as shown in Figure 3(b). Five strain gauges were mounted on the surface of the CFRP plate at a spacing of 100 mm. Meanwhile, the loads and actuator displacements were recorded with data acquisition systems.

3. Test Results

3.1. Failure Patterns. Typical failure patterns of the tested specimens are shown in Figure 4. Crack propagated along the initial vertical cut with the increase of the loading. The governing mode of failure is yielding of the cracked cross section. In the case of RHS-II-03-P0 without anchorage system, CFRP plates suddenly dropped off when load attained to peak value. This is due to the fact that interface debonding occurred and developed quickly. Meanwhile, debonding can be deferred with anchorage systems. With regard to other specimens in Group II and III, CFRP plate can be deformed with RHS steel beams until failure. Hence it suggests that the anchorage systems can effectively improve the loading and deformation capacity of repaired specimens. At failure, it was observed that CFRP cracked in the longitudinal direction.

3.2. Load-Deflection Relationships. The load-deflection responses for the control and repaired beams are plotted in Figure 5. Measured deflections were located at the bottom of the middle span. These curves provided valuable evaluation of the parameters reflecting the stiffness, strength, and flexure capacity of the specimen. All repaired specimens display lesser deflection than that of control ones. It means that the repaired specimens were stiffer than the bare steel specimens. The additional stiffness was attributed by the external bonded CFRP plate on the steel surface. The quantity of bonded CFRP plate has effect on the stiffness improvement. The stiffness of prestressed specimens should be less than the stiffness of nonprestressed ones since 40 mm width plate was used for prestressed ones instead of 50 mm width plate for nonprestressed ones. This can be justified by the fact that the curve of specimen RHS-III-30-P10 locates between the curves of RHS-I-30 and RHS-II-30-P0.

It can be observed that there is a load drop for all repaired specimens. This is due to the sudden debonding between steel and CFRP plate. With regard to the specimen RHS-II-03-P0, which was not anchored, the load decreased continuously with an increase in the deflection due to

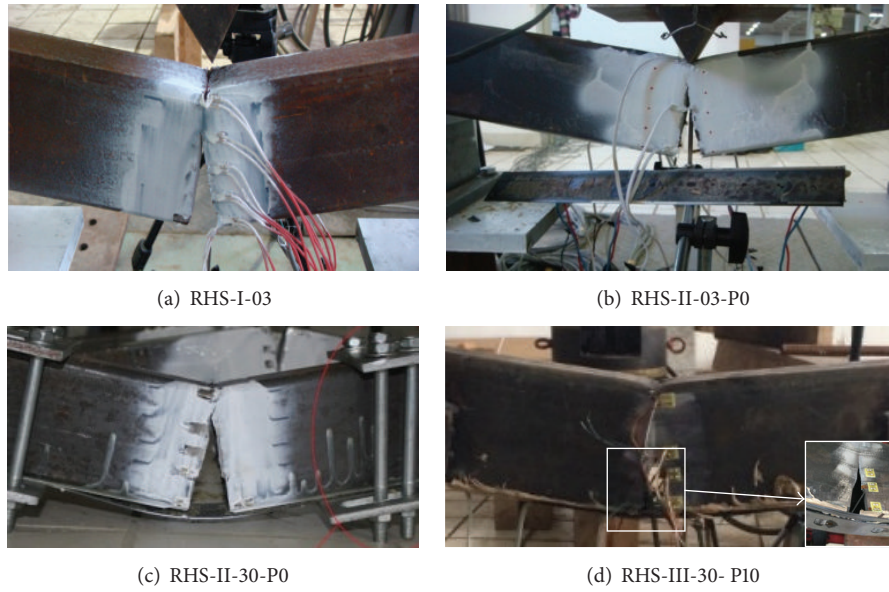


FIGURE 4: Failure patterns of the tested specimens.

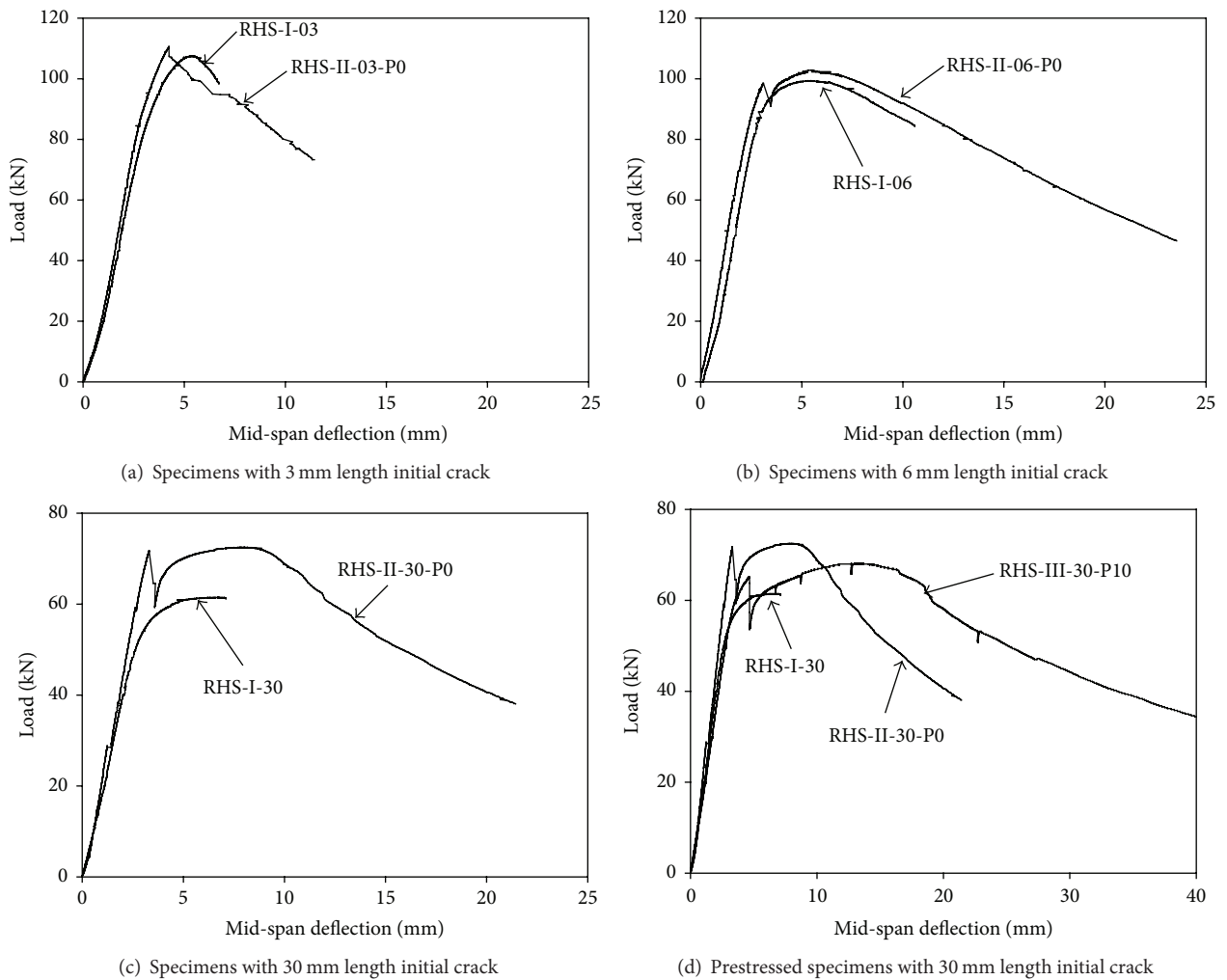


FIGURE 5: Load versus mid-span deflection curves.

TABLE 3: Yield load and ultimate load.

Specimen number	Theoretical yield load (kN)	Experimental yield load (kN)	Experimental ultimate load (kN)
RHS-I-03	64.36	63.20	107.50
RHS-I-06	45.51	50.90	99.40
RHS-I-30	25.98	25.22	61.50
RHS-II-03-P0	75.07	73.35	110.60
RHS-II-06-P0	58.39	59.85	102.80
RHS-II-30-P0	43.29	48.55	72.50
RHS-III-06-P10	67.00	70.02	104.35
RHS-III-30-P10	52.18	55.20	68.20

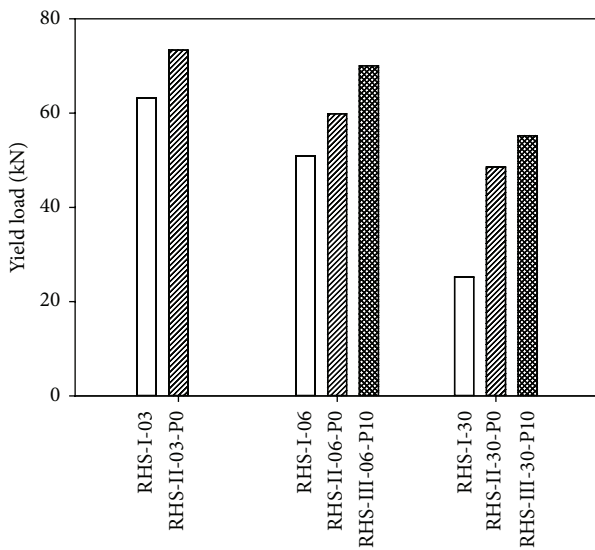


FIGURE 6: Experimental yield load.

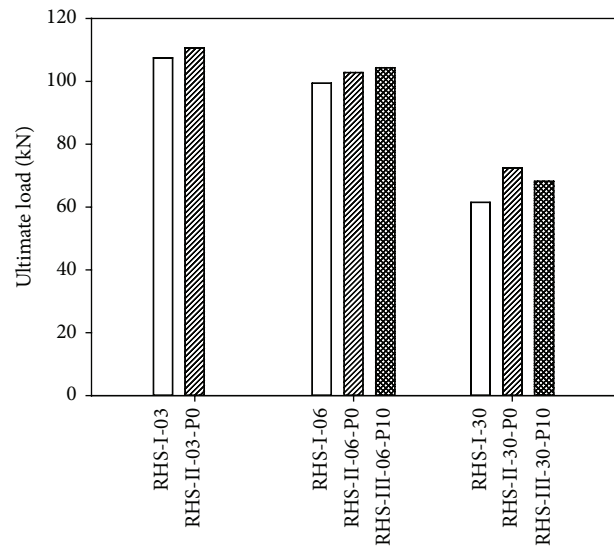


FIGURE 7: Experimental ultimate load.

the loss of CFRP plate. Meanwhile, the specimens that have mechanical anchorage regained load bearing capacity and deformed with large deflection. This indicates that CFRP plate can work together with steel beam even after debonding for the restraints provided by the anchorage. Comparing the ultimate load bearing capacities, it can be observed that repaired specimens have larger values. The increment of the load bearing capacity is more significant for deeper crack length.

3.3. Yield Load and Ultimate Load. The yield load and the ultimate load capacity obtained from the test for both the control specimens (bare steel beam) and CFRP patched specimens are shown in Table 3. Good agreement between theoretical and experimental yield loads was observed.

The effectiveness of CFRP patching was examined by comparing with the control specimens to quantify the percentage increase in yield and ultimate load carrying capacity (Figures 6 and 7). With regard to the specimens with an initial cut length of 3 mm, the yield load of a patched specimen is 75.07 kN which is slightly under the value of 79.81 kN which is the theoretical yield load of an unpatched intact specimen. This means that the CFRP repairing can restore the

yield load for slightly damaged specimens. For the specimens with the same damage degree, namely, 3 mm crack depth, the yield load of patched specimen increased by 16.06% compared to the control specimen. The ultimate load of a patched specimen with 3 mm initial crack is 110.60 kN which is less than 154.63 kN of the theoretical ultimate load of an unpatched intact specimen. This indicates that even a small crack can imperil the ultimate load of the specimen. The ultimate load of a patched specimen increased a little by 2.88% compared to the control specimen for specimens with 3 mm crack depth.

Similarly, the yield and ultimate load of patched specimen RHS-II-06-P0 increased by 17.58% and 3.42% compared to the control specimen RHS-I-06, respectively. With regard to the specimens with large initial cut length, namely, 30 mm, the yield load of patched specimen significantly increased by 92.51% compared to the control specimen. The ultimate load of patched specimen increased by 17.89% compared to the control specimen. It is apparent that repair effect is more significant for specimens with deeper initial cut. It is also observed that the increase of the ultimate load is relatively less than the increase of the yield load. The reason may be due to the fact that the CFRP debonded with the steel beam in the latter range of loading.

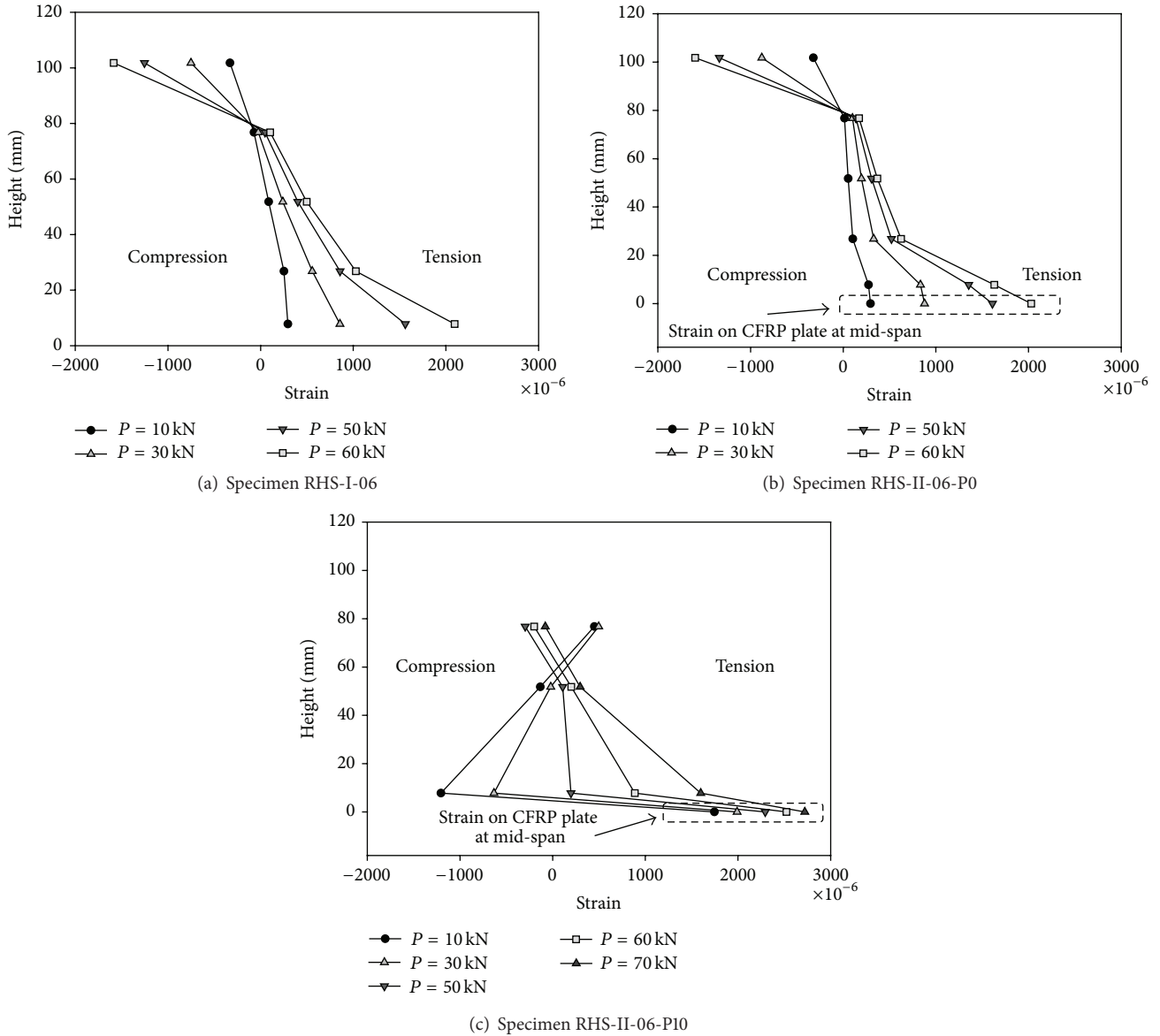


FIGURE 8: Comparison of strain distribution on cross section.

It can be observed that prestressed CFRP patching technique is beneficial to the increase of yield and ultimate load. In terms of yield strength enhancement, prestressed specimens RHS-III-06-P10 and RHS-III-30-P10 show 37.56% and 118.87% more load increment than the control beams. Likewise, the two specimens increased 4.98% and 10.89% of the ultimate load compared to the control beams.

3.4. Strain Distribution at Mid-Span. The measured strain distribution on the cross section can provide valuable information on the assessment of the steel beams under external loading. Figure 8 shows comparisons of strain distributions on cross section at mid-span when the initial crack is 6 mm. The abscissa is strain measured at the mid-span, while the ordinate is the distance from the bottom of the CFRP plate with repaired specimens. It can be observed from

Figure 8(a) that the strain distribution is almost linear along height direction except that the top strain and bottom strain are a little large. The same phenomenon is observed from Figure 8(b) which also plotted the strain on CFRP plate. This may be due to the strain concentration at the crack tip and the local influence of the load cell on the top of beam. At the same load level, strain values of repaired specimen are slightly smaller than the values of the control one by comparison of Figures 8(a) and 8(b). This indicates that CFRP plate works together with the steel beam. Meanwhile, strain of CFRP is around 2000×10^{-6} under yield load.

With regard to the specimen repaired with prestressed CFRP plate, strains on the CFRP plate are relatively large, as shown in Figure 8(c). It ranges almost from 1400×10^{-6} to 5000×10^{-6} with the increase of the loading level. The lower part of the specimen changed from compression to

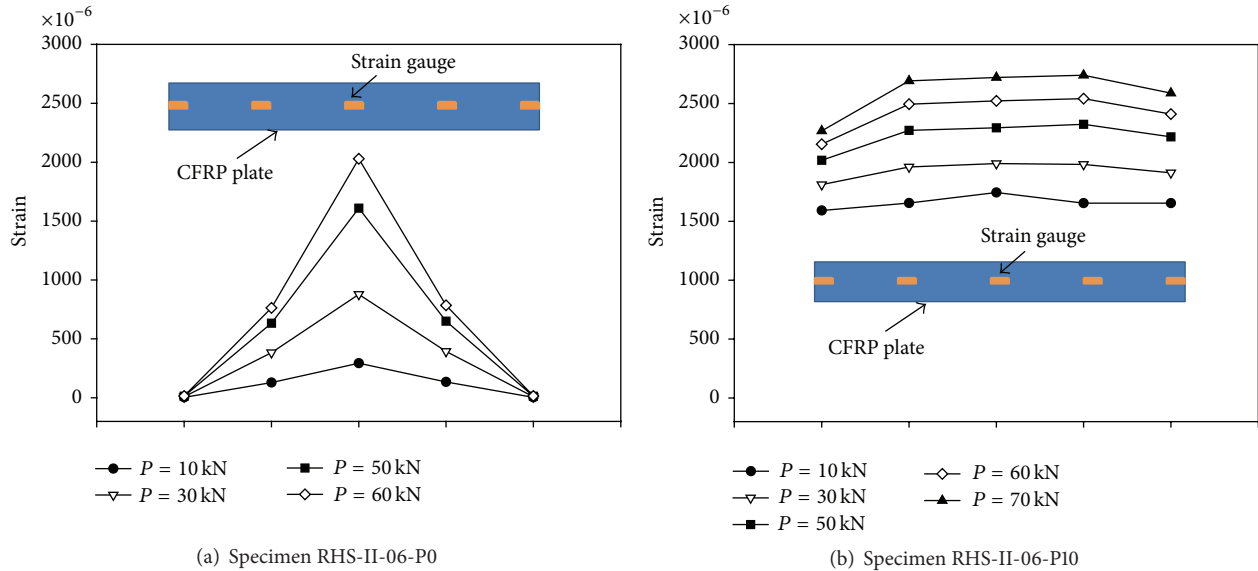


FIGURE 9: Comparison of strain distribution on CFRP plate.

tension state. This is due to the fact that prestressed CFRP plate introduced compression stage at lower part of the beam and it is predominant with relatively low loading level. This is beneficial to the serviceability since compression state can prevent crack propagation. When the loading level surpassed certain value, the lower part changed to tension state. And crack began to propagate when the effective stress intensity factor is larger than the threshold value.

3.5. Strain Distribution on CFRP Plate. To better understand the repair efficiency of CFRP plate, strains on the CFRP plates were plotted along length direction as shown in Figure 9. It clearly shows that strains distribute uniformly on CFRP plate for prestressed specimen. With regard to specimen without prestressing, a symmetrical distribution shape was observed and strain at mid-span achieved maximum value. The strain value significantly decreased away from middle span to two ends. This is a clear indication that prestressed CFRP plate utilization efficiency is better than nonprestressed one.

4. Concluding Remarks

This research has experimentally investigated CFRP repairing RHS steel beams. It is observed that external patching CFRP plate can significantly increase the yield load with the increase of the damage degree, while the repairs can only slightly increase the ultimate load. Debonding of interface between CFRP and steel is vital to the specimens under large load. Therefore two anchorage systems were proposed and they can fasten CFRP plate at both ends to specimen. The experimental results clearly indicate the techniques can significantly reduce the deformation of repaired cracked specimens. The prestressing CFRP plate can further increase the yield load and increase the utilization efficiency of the CFRP plate. This paper only presents test results of failure patterns and strain

distributions. Numerical analysis and parametric studies are necessary in the future. Besides this, fatigue test is essential since the CFRP repair can alleviate stress level of steel beam.

Conflict of Interests

The authors declare that there is no conflict of interests regarding the publication of this paper.

Acknowledgments

This project was supported by the National Program on Key Basic Research Project of China (973 Program) (Grant no. 2015CB057700) and the National Natural Science Foundation of China (Grant no. 51508406).

References

- [1] A. Baker, "Bonded composite repair of fatigue-cracked primary aircraft structure," *Composite Structures*, vol. 47, no. 1-4, pp. 431-443, 1999.
- [2] X.-L. Zhao and L. Zhang, "State-of-the-art review on FRP strengthened steel structures," *Engineering Structures*, vol. 29, no. 8, pp. 1808-1823, 2007.
- [3] P. Colombi and C. Poggi, "Strengthening of tensile steel members and bolted joints using adhesively bonded CFRP plates," *Construction and Building Materials*, vol. 20, no. 1-2, pp. 22-33, 2006.
- [4] S. S. J. Moy, *FRP Composites: Life Extension and Strengthening of Metallic Structures: ICE Design and Practice Guide*, Thomas Telford, London, UK, 2001.
- [5] M. Tavakkolizadeh and H. Saadatmanesh, "Strengthening of steel-concrete composite girders using carbon fiber reinforced polymers sheets," *Journal of Structural Engineering*, vol. 129, no. 1, pp. 30-40, 2003.

- [6] X.-L. Zhao, *FRP-Strengthened Metallic Structures*, CRC Press, Boca Raton, Fla, USA, 2013.
- [7] T. C. Miller, M. J. Chajes, D. R. Mertz, and J. N. Hastings, "Strengthening of a steel bridge girder using CFRP plates," *Journal of Bridge Engineering*, vol. 6, no. 6, pp. 514–522, 2001.
- [8] J. Haedir, M. R. Bambach, X.-L. Zhao, and R. H. Grzebieta, "Strength of circular hollow sections (CHS) tubular beams externally reinforced by carbon FRP sheets in pure bending," *Thin-Walled Structures*, vol. 47, no. 10, pp. 1136–1147, 2009.
- [9] J. Haedir and X.-L. Zhao, "Design of CFRP-strengthened steel CHS tubular beams," *Journal of Constructional Steel Research*, vol. 72, pp. 203–218, 2012.
- [10] M. V. Seica and J. A. Packer, "FRP materials for the rehabilitation of tubular steel structures, for underwater applications," *Composite Structures*, vol. 80, no. 3, pp. 440–450, 2007.
- [11] N. K. Photiou, L. C. Hollaway, and M. K. Chryssanthopoulos, "Strengthening of an artificially degraded steel beam utilising a carbon/glass composite system," *Construction and Building Materials*, vol. 20, no. 1-2, pp. 11–21, 2006.
- [12] M. Elchalakani, "CFRP strengthening and rehabilitation of degraded steel welded RHS beams under combined bending and bearing," *Thin-Walled Structures*, vol. 77, pp. 86–108, 2014.
- [13] R. E. Koller, I. Stoecklin, S. Valet, and G. P. Terrasi, "CFRP-strengthening and long-term performance of fatigue critical welds of a steel box girder," *Polymers*, vol. 6, no. 2, pp. 443–463, 2014.
- [14] A. Fam, C. MacDougall, and A. Shaat, "Upgrading steel-concrete composite girders and repair of damaged steel beams using bonded CFRP laminates," *Thin-Walled Structures*, vol. 47, no. 10, pp. 1122–1135, 2009.
- [15] E. Ghafoori, M. Motavalli, J. Botsis, A. Herwig, and M. Galli, "Fatigue strengthening of damaged metallic beams using pre-stressed unbonded and bonded CFRP plates," *International Journal of Fatigue*, vol. 44, pp. 303–315, 2012.
- [16] T. Chen, Q.-Q. Yu, X.-L. Gu, and X.-L. Zhao, "Study on fatigue behavior of strengthened non-load-carrying cruciform welded joints using carbon fiber sheets," *International Journal of Structural Stability and Dynamics*, vol. 12, no. 1, pp. 179–194, 2012.
- [17] H. Liu, R. Al-Mahaidi, and X.-L. Zhao, "Experimental study of fatigue crack growth behaviour in adhesively reinforced steel structures," *Composite Structures*, vol. 90, no. 1, pp. 12–20, 2009.

Research Article

Development of Ecoefficient Engineered Cementitious Composites Using Supplementary Cementitious Materials as a Binder and Bottom Ash Aggregate as Fine Aggregate

Jin Wook Bang,¹ G. Ganesh Prabhu,² Yong Il Jang,³ and Yun Yong Kim¹

¹Department of Civil Engineering, Chungnam National University, Daejeon 305-764, Republic of Korea

²Department of Civil Engineering, KPR Institute of Engineering and Technology, Coimbatore, Tamil Nadu 641 407, India

³Department of Construction Engineering Education, Chungnam National University, Daejeon 305-764, Republic of Korea

Correspondence should be addressed to Yun Yong Kim; yunkim@cnu.ac.kr

Received 14 February 2015; Revised 23 March 2015; Accepted 27 March 2015

Academic Editor: Togay Ozbakkaloglu

Copyright © 2015 Jin Wook Bang et al. This is an open access article distributed under the Creative Commons Attribution License, which permits unrestricted use, distribution, and reproduction in any medium, provided the original work is properly cited.

The purpose of this study is to develop ecoefficient engineered cementitious composites (ECC) using supplementary cementitious materials (SCMs), including fly ash (FA) and blast furnace slag (SL) as a binder material. The cement content of the ECC mixtures was replaced by FA and SL with a replacement rate of 25%. In addition, the fine aggregate of the ECC was replaced by bottom ash aggregate (BA) with a substitution rate of 10%, 20%, and 30%. The influences of ecofriendly aggregates on fresh concrete properties and on mechanical properties were experimentally investigated. The test results revealed that the substitution of SCMs has an advantageous effect on fresh concrete's properties; however, the increased water absorption and the irregular shape of the BA can potentially affect the fresh concrete's properties. The substitution of FA and SL in ECC led to an increase in frictional bond at the interface between PVA fibers and matrix, improved the fiber dispersion, and showed a tensile strain capacity ranging from 3.3% to 3.5%. It is suggested that the combination of SCMs (12.5% FA and 12.5% SL) and the BA aggregate with the substitution rate of 10% can be effectively used in ECC preparation.

1. Introduction

Engineered cementitious composites (ECC) are a special generation of high performance fiber reinforced cementitious composites (HPFRCC), which are characterized by pseudo strain-hardening behavior and tight crack width [1, 2]. The micromechanical design of ECC exhibits a remarkable tensile ductility capacity, even though the ECC includes short fibers in a volume fraction of around 2%. The strain-hardening behavior of ECC is very similar to the ductile metal and exhibits a strain capacity 500–600 times higher than that of normal concrete [3]. The aggregates in ECC significantly influence the strain-hardening performance through alterations in matrix fracture toughness and fiber dispersion; furthermore, in order to attain the remarkable tensile performance and avoid fiber clumping, the use of coarse aggregate has been avoided in the standard ECC mixture [1]. The fiber dispersion in ECC is the highly important property and

has led to a reduction in the number of effective fibers at the failure crack phase, causing decline in tensile capacity. Therefore, microsilica sand (SS) with an average size of 110 μm is used in ECC mixture, to maintain uniform fiber dispersion and low fracture toughness.

The use of cement content in the ECC is nearly 5 times higher than that in normal concrete, resulting in higher shrinkage, heat of hydration, and cost [3]. The increased utilization of ECC led to increased CO₂ emissions, significantly contributing to pollution health risks and global warming. Over the past several decades, the inclusion/replacement of cement using supplementary cementitious materials (SCMs) including silica fume, fly ash (FA), and granulated blast furnace slag (SL) in concrete has improved the engineering properties of the concrete. Among these SCMs, FA and SL have been widely used as successful replacement materials for cement [4–6] and in particular FA has been successfully used in concrete production around the world for over 50 years [7].

TABLE 1: Chemical composition of cement, SCMs, SS, and BA.

Chemical composition	OPC (%)	Fly ash (FA) (%)	Blast furnace slag (SL) (%)	Silica sand (SS) (%)	Bottom ash aggregate (BA) (%)
Lime (as CaO)	62.80	3.61	45.95	—	2.48
Soluble silica (as SiO ₂)	21.16	50.72	28.14	98.10	47.90
Alumina (as Al ₂ O ₃)	4.65	20.73	15.87	1.12	25.94
Iron oxide (as Fe ₂ O ₃)	3.14	6.37	1.06	0.71	4.76
Magnesia (as MgO)	2.18	1.08	4.98	—	1.10
Sulphur calculated as sulphuric anhydride (as SO ₃)	2.13	0.54	2.12	—	—
Loss on ignition (LOI)	2.18	3.04	0.35	—	—
Na ₂ O	—	—	—	—	1.38

In addition, it has been recognized that the SL with a vitreous microstructure has not only a filler but also a dispersing effect associated with the surface chemical action [8]. In recent years, the development of ecoefficient ECC using SCMs, specifically using FA and SL, has become widespread [9, 10] with the goal of reducing environmental impacts. The increase in FA content in ECC reduces the matrix toughness and increases the interface frictional bond, enhancing the tensile strain capacity as a result [11]. Furthermore, the ECC mixtures with high volumes of FA remain durable in terms of mechanical performance after an accelerated aging period and show a tensile strain capacity of more than 2% [7]. The dosage of SL in ECC controlled the multiple cracking and also enhanced the fiber/matrix bond strength [2, 10].

Even though there has been some research regarding the influence of SCMs (particularly FA and SL) on the engineering properties of ECC, more research is needed to understand the effects of an FA and SL combination (binary SCMs) on the engineering properties of ECC. In addition, the manufacturing of the SS used in standard ECC is quite expensive, and the CO₂ emissions associated with the manufacture of SS are known to create environmental problems [1]. For this reason, it has become imperative to find an alternative ecofriendly fine aggregate. Coal has been significantly used as a fuel in electricity production in Korea, and more than 6 million tons of coal has been utilized annually for the same. When coal is burned in a boiler for power generation, three types of by-products including FA, bottom ash (BA), and boiler slag are produced. FA has proved to be a valuable SCM in many applications, especially cement manufacturing. However, BA, which is removed from the bottom of the furnace, has not been reutilized effectively compared to FA. The formation of BA is about 10–15% of the total amount of coal utilized, meaning millions of tons of waste. In Korea, most BA is buried in the soil, which creates an environmental problem and soil contamination. As such, it is necessary to find ways to reuse BA in order to achieve sustainable development.

To resolve these issues, an investigation was carried out to develop an ecoefficient ECC using SCMs including FA and SL as a binder and BA as a fine aggregate. The cement content of the ECC mixtures is replaced by FA and

SL as a binary binder system (cement + FA and cement + SL) and ternary binder system (cement + FA + SL). Huang et al. [1] and Şahmaran and Li [7] found that the increase in the substitution of FA slightly improves the strain-hardening capacity of the ECC; however, it reduces the initial cracking load of the ECC, so that, in order to enhance the initial cracking strength, without compromising the strain-hardening capacity of the ECC, the replacement rate of SCMs was maintained about 25%. The fine aggregate of the ECC was replaced by BA at the rate of 10%, 20%, and 30% and this substitution was made in the ternary binder ECC mixture (cement + FA + SL). According to the test method used by the Ministry of Environment in Korea [12], the leaching test was performed to identify any toxic material present in the BA and ecoefficient ECC developed using FA, SL, and BA. The influence of ecofriendly aggregates was evaluated based on the fresh concrete properties and mechanical properties.

2. Materials and Testing Methods

2.1. Materials

2.1.1. Binders: Ordinary Portland Cement (OPC), Fly Ash (FA), and Granulated Blast Furnace Slag (SL). OPC having a density and fineness of 3.15 g/cm³ and 3,200 cm²/g, respectively, was used. A class I type of FA obtained from a Korean thermal power plant was used and the average particle size of the FA was about 25 µm. The density and fineness of the FA were about 2.16 g/cm³ and 3,645 cm²/g, respectively. SL obtained from “H” company in Korea was used in this study. The average particle size, density, and fineness of the SL were 11 µm, 2.94 g/cm³, and 4,310 cm²/g, respectively. Chemical analysis was performed for all types of binders and the composition is given in Table 1.

2.1.2. Fine Aggregate: Silica Sand (SS) and Bottom Ash (BA). SS having an average and a maximum grain size of 110 µm and 150 µm, respectively, was used. The density of the SS was about 2.64 g/cm³ and the water absorption was about 1.01%. The chemical composition of the SS is listed in Table 1. BA obtained from a thermal power plant located in Korea was

TABLE 2: Mixture proportions of all ECC mixtures.

Mixture designation	Water to binder ratio (W/B)	Unit weight (kg/m ³)					PCSP (% of binder)	HPMC (% of binder)	PVA (% in volume of ECC)
		Cement (C)	Fly ash (FA)	Blast furnace slag (SL)	Silica sand (SS)	Bottom ash aggregate (BA)			
Reference ECC		758	0	0	609	0	0		
ECC-FA		569	190	0	537	0	0.20		
ECC-SL		569	0	190	598	0	0.10		
ECC-FASL	0.60	569	95	95	568	0	0.20	0.40	
ECC-FASL-BA10%		569	95	95	511	57	0.20		
ECC-FASL-BA20%		569	95	95	454	114	0.20		
ECC-FASL-BA30%		569	95	95	397	171	0.20		

PCSP: polycarboxylic superplasticizer; HPMC: hydroxypropyl methylcellulose.

used in this study. The obtained BA was sieved and BA with a size of less than 1 mm was used. The density of BA was about 2.38 g/cm³ and the water absorption of the BA was about 2.88%, which is higher than that of the SS. The chemical analysis results showed that BA contains about 47.90% silica (SiO₂) and 25.94% alumina (Al₂O₃), which is summarized in Table 1. The particle morphology of BA and SS showed that SS has a uniform size and nearly round shape, while the BA has a nonuniform size and a mixture of round and angular shapes.

2.1.3. Polyvinyl Alcohol (PVA) Fiber. Polyvinyl alcohol (PVA) fiber was used in this study to prepare the ECC mixture. The length and diameter of the fiber were about 12 mm and 40 μm, respectively. The tensile strength and elastic modulus of the fiber were 1,560 MPa and 37 GPa, respectively. The elongation and density of the fiber were about 6~10% and 1.3 g/cm³, respectively.

2.1.4. Chemical Admixtures. The combination of polycarboxylic superplasticizer and hydroxypropyl methylcellulose was used to improve the matrix fluid properties, resulting in an enhancement in the dispersion of reinforcing fibers.

2.2. Mixture Proportion and Specimen Preparation. Among the seven ECC mixtures, cement content of three mixtures was replaced with FA and SL at a replacement level of 25% (such as 75% cement + 25% FA, 75% cement + 25% SL, and 75% cement + 12.5% FA + 12.5% SL). The other three mixtures were prepared with BA at substitution rates of 10%, 20%, and 30% and this substitution was made in the ternary binder system (80% cement + 12.5% FA + 12.5% SL). The one remaining mixture was the reference mixture and had no SCMs or fine aggregate substitution. The water binder ratio was constantly maintained for all mixtures and the value was about 0.6. The detailed mix proportions of all mixtures are summarized in Table 2. All the ECC mixtures were prepared using a 15-liter mortar mixer with the same speed and time and were prepared at room temperature. Initially, the binding materials and fine aggregate were mixed at 100 rpm for 1.5

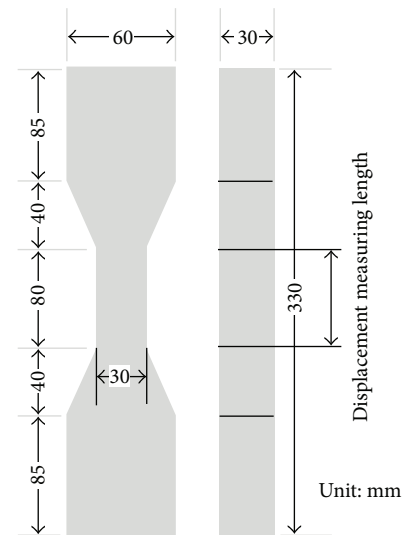


FIGURE 1: Details of specimen for direct tensile test (dog-bone shape).

minutes, followed by the water and admixtures being added to the dry mix and mixed at 200 rpm for 3 minutes. After that, PVA fibers were added to the wet mixture and the mixture was mixed at 200 rpm for 5 minutes to obtain a uniform ECC mixture. The influence of the SCMs binders and BA on the fresh concrete's properties was evaluated through the slump cone test and self-consolidating tests. After the measurement of fresh concrete properties, the specimens, including dog-bone shaped specimens (see Figure 1), cylinders, and beam specimens were cast in the moulds for tensile, compression, and flexural tests. All specimens were prepared layer by layer and each layer was moderately compacted by the table vibrator. After casting of all specimens, the specimens were covered with a plastic sheet in order to avoid moisture loss. Specimens were then kept at room temperature for 24 hrs and thereafter were demoulded and cured at room temperature of about 23°C for 28 days. To simplify the discussion of

TABLE 3: Test method and equipment for detection analysis of harmful materials [12, 13].

Test items	Test methods and equipment
Cr ⁶⁺	UV-Vis spectrophotometer
As, Hg	AAS (atomic absorption spectrophotometer)
Pb, Cd, Cu, CN	ICP (inductive coupled plasma emission spectrophotometer)
PCE ¹ , TCE ² , OP ³	ATD-GC/MS (automated thermal desorption-gas-chromatography/mass spectrophotometry)

PCE¹: tetrachloroethylene, TCE²: trichloroethylene, and OP³: organophosphates.

the mixtures, names were given to the mixtures, such as ECC-FA, ECC-SL, ECC-FASL, ECC-FASL-BA10%, ECC-FASL-BA20%, and ECC-FASL-BA30%. For example, the name ECC-FASL-BA10% indicates an ECC mixture substituted with a combination of FA and SL and 10% of bottom ash.

2.3. Test Methods

2.3.1. Fresh Properties

(1) *Slump Cone Test and Self-Consolidating Tests.* The slump cone apparatus with top and bottom diameter of 100 mm and 200 mm, respectively, was used. The height of the apparatus was about 300 mm. The cone was placed on the flat surface and filled with ECC. The ECC was then allowed to flow by lifting up the cone. The average diameter of the ECC flow was measured along two diagonals [14].

To measure the self-consolidation of the ECC, a rectangular box with a size and height of 120 mm × 200 mm and 400 mm, respectively, was used, and the box was divided into two chambers using a center partition wall. A gate with a height of 80 mm was fixed in the bottom of the partition wall. Initially, the gate was closed and one chamber of the box was filled with ECC up to the height of 400 mm. After the gate was removed, the flow of height ECC to the next chamber was measured [14].

2.3.2. *Leaching Test for Hazardous Materials.* Enforcement Regulation of the Waste Management Law [13] recommends the standard limits for deleterious substances present in the waste. In order to verify that limit, BA was subjected to a leaching test before it was used in ECC; in addition, the amount of deleterious substances present in the ecoefficient ECC developed using FA, SL, and BA was also evaluated. According to the procedure described in the Ministry of Environment waste process test method, the leaching test was performed. The test methods and equipment utilized for detection, specified in solid waste process test, Ministry of Environment Korea [12], are listed in Table 3.

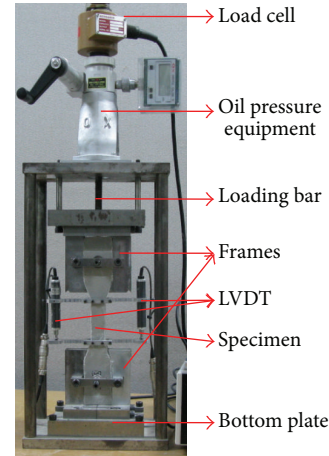


FIGURE 2: Direct tensile test setup.

2.3.3. Mechanical Properties

(1) *Direct Tensile Test.* In order to evaluate the influence of SCMs and BA on the tensile property of ECC, direct tensile tests were performed on dog-bone shaped specimens and the geometry of the specimens is presented in Figure 1. The tests were performed in a controlled manner with a loading rate of 0.2 mm/min. To measure the displacement of the specimens, two linear variable displacement transducers (LVDTs) with the gauge length of 10 mm were attached to the specimens. Figure 2 illustrates the experimental setup. During testing the crack formation and propagation and crack widths were observed and measured.

(2) *Compressive Strength Test.* To evaluate the compressive strength of ECC, cylinders with diameter 100 mm and height 200 mm were prepared and cured for 28 days at a temperature of $23 \pm 1^\circ\text{C}$. After that, the specimens were tested on the universal testing machine (UTM) with a capacity of 1,000 kN. The test was performed according to the procedure described in KS F 2405 [15].

(3) *Flexural Strength Test.* According to the procedure described in KS F 2408 [16], flexural strength tests were performed on ECC beams. The ECC beam specimens with dimensions of 400 mm × 100 mm × 20 mm were prepared and cured for 28 days at room temperature. A four-point bending setup was adopted for testing and the tests were performed on a UTM with a capacity of 200 kN. Tests were performed until failure. The deflection of the beam was controlled at a loading rate of 0.5 mm/min and the midspan deflection of the beams measured using two LVDTs with the gauge length of 25 mm. The flexural strength of the ECC beam was calculated using

$$f = \frac{(P \times l)}{(b \times d^2)}, \quad (1)$$

where f is the flexural strength; P is the maximum load; l is the span length; and b and d are the width and height of the specimen, respectively.

TABLE 4: Test results of slump cone and self-consolidation test of all ECC mixtures.

Mixture designation	Slump cone test			Self-consolidation test		
	D_1 (mm)	D_2 (mm)	FI (Γ)	H (mm)	H_0 (mm)	L
Reference ECC	655	650	9.6	157	400	0.78
ECC-FA	660	655	9.8	160	400	0.80
ECC-SL	690	685	10.8	180	400	0.90
ECC-FASL	680	670	10.4	174	400	0.87
ECC-FASL-BA10%	620	610	8.4	150	400	0.75
ECC-FASL-BA20%	615	610	8.3	150	400	0.75
ECC-FASL-BA30%	595	590	7.8	140	400	0.70

3. Results and Discussions

3.1. Fresh Properties

3.1.1. Slump Cone Test and Self-Consolidation Test. The results of the test of flow properties and self-consolidation of all ECC mixtures are summarized in Table 4. The flowability and the self-consolidation of ECC are presented in terms of flowability index (Γ) and self-consolidating index (L), respectively, and the following equations were used to calculate the flowability index (Γ) and self-consolidating index (L), respectively:

$$\Gamma = \frac{(D_1 \times D_2) - D_0^2}{D_0^2}, \quad (2)$$

$$L = \frac{2H}{H_0}, \quad (3)$$

where D_1 is the maximum diameter of the flow; D_2 is the diameter of flow perpendicular to D_1 ; D_0 is the diameter of the slump cone (200 mm); H_0 is the initial height of the fresh ECC (400 mm); H is the flow of height ECC to the next chamber.

It was observed that the substitution of SCMs showed an advantageous effect on fresh concrete properties (both flow properties and self-consolidation), and in particular the substitution of SL and the combination of SCMs showed improved fresh concrete properties as shown in Figure 3. The slump flow of mixture ECC-FA ($\Gamma = 9.8$) was relatively equal to the slump flow of reference mixture ($\Gamma = 9.6$). However, the slump flows of mixtures ECC-SL and ECC-FASL ($\Gamma = 10.8$ and $\Gamma = 10.4$) were higher than that of the reference mixture by 12.03% and 7.88%, respectively. The self-consolidating test also exhibited the perfect self-consolidation of mixtures ECC-SL and ECC-FASL of 0.90 and 0.87, respectively, which was 15.38% and 11.54%, respectively, higher than that of the reference mixture. The SCMs substitution contributed to the improved uniform fiber dispersion and as a result improved the fresh concrete properties observed. As shown in Figure 3, the substitution of BA in the ECC potentially

affects the fresh concrete properties of the ECC; in particular, the increase in BA decreases the fresh concrete properties further. However, the flow and self-consolidation properties of mixture ECC-FASL-BA10% are very similar to those of the reference mixture. The decrease in fresh concrete properties with the substitution of BA is attributed to the higher water absorption and the irregular shape of the BA. The increased water absorption property of the BA has increased the water demand in the ECC. In addition, the irregular shape and big particle size of BA created more friction against the flow of ECC, and as a result the workability of the ECC developed using BA decreased with the increase in the BA substitution rate. For example, the substitution of 10% of BA decreased the self-consolidation by 16.10%, when compared to the mixture ECC-FASL. On the other hand, the mixture ECC-FASL-BA30% decreased its self-consolidation by 24.29%. A similar trend was observed in the flowability test.

3.2. Leaching Test for Hazardous Materials. The results of leaching tests of BA and the ECC developed using FA, SL, and BA are summarized in Table 5. The results were compared with the limit for deleterious substances specified in the Enforcement Regulation of the Waste Management Law in Table 5. It was observed that the deleterious substances (Cr^{6+} , As, Cd, Pb, Cu, CN, Hg, PCE, TCE, and OP) present in the BA were very negligible, and in particular, the substances CN, Hg, PCE, TCE, and OP were not detectable, when compared to the limit value specified in the Enforcement Regulation of the Waste Management Law [13]. From this observation, it can be inferred that there are no harmful substances present in the BA, suggesting that BA can be effectively used as a substitute or alternative material in ECC applications. The results of leaching tests of ECC developed using FA, SL, and BA also revealed that the presence of deleterious substances is very negligible; in addition, many substances, specifically Cr^{6+} , As, Cd, CN, PCE, TCE, and OP, are not detectable. As can be seen from Table 5, the presence of deleterious substances in BA was reduced with the substitution in ECC. From the above observation, it can be inferred that SCMs and BA can be effectively used as an alternative material to develop the ecoefficient ECC.

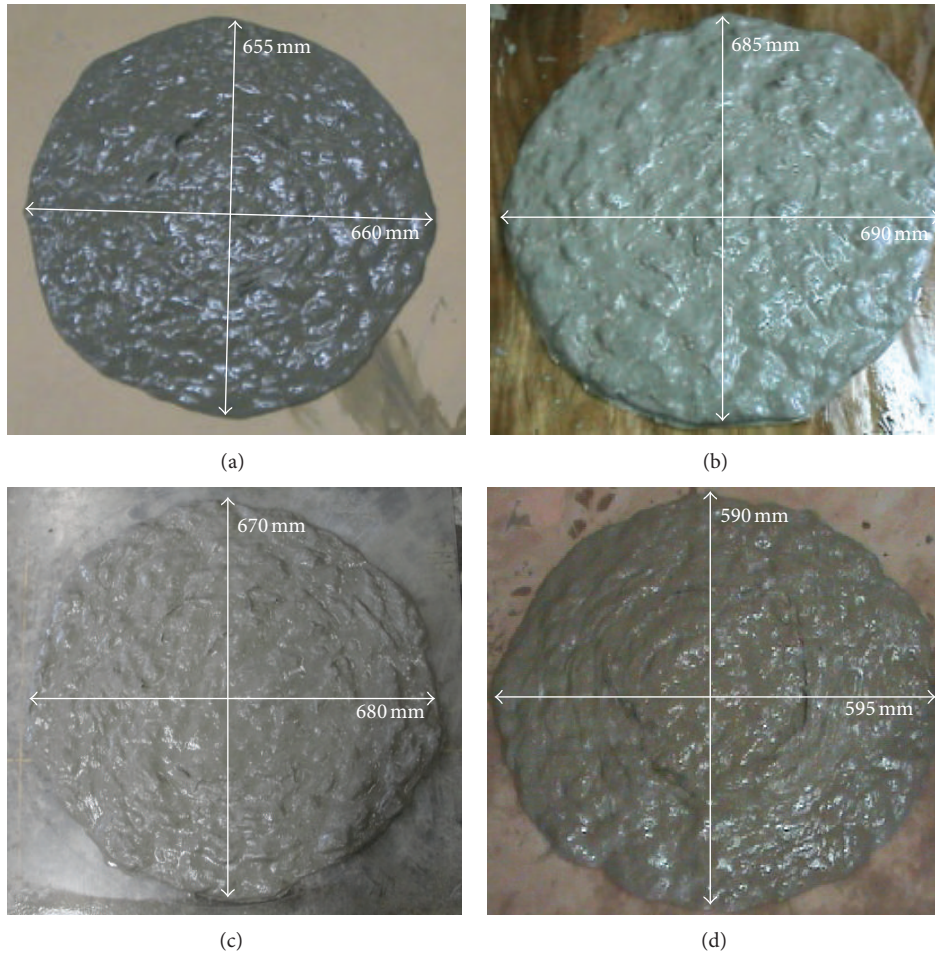


FIGURE 3: Slump flow behavior of ECC.

TABLE 5: Environment criteria and detection amount of harmful materials by solid waste management law.

Mixture designation	Test items unit: mg/L									
	Cr ⁶⁺	As	Cd	Pb	Cu	CN	Hg	PCE	TCE	OP
Environment criteria	1.5	1.5	0.3	3	3	1	0.005	0.1	0.3	1
BA	0.055	0.045	0.005	0.097	0.179	Not detected	0.000543	Not detected	Not detected	Not detected
ECC-FA	Not detected	Not detected	0.001	0.002	0.052	Not detected	0.000062	Not detected	Not detected	Not detected
ECC-SL	Not detected	Not detected	Not detected	0.004	0.039	Not detected	0.000067	Not detected	Not detected	Not detected
ECC-FASL-BA20%	Not detected	Not detected	0.002	0.003	0.049	Not detected	0.000044	Not detected	Not detected	Not detected

3.3. Mechanical Properties

3.3.1. Direct Tensile Test. The tensile properties including maximum tensile strain and ultimate tensile stress are summarized in Table 6. The uniaxial tensile behavior of all ECC mixtures is presented in Figure 4. It was observed that all of the ECC mixtures exhibited an apparent multiple cracking pattern that accompanied pseudo strain-hardening behavior with the strain capacities ranging from 1.4% to nearly 3.5%. The ECC developed by FA with the substitution rate of 25% (ECC-FS) exhibited a strain capacity of 3.3%, and its

ductility was also higher than that of the reference ECC mixture, as shown in Figure 4. However, the FA did not have an influence on the strength properties; significantly, it lowered the tensile strength development when compared to the reference ECC mixture, finding that was compatible with the previous research results [2, 7]. The substitution of FA in ECC enhanced the frictional bond at the interface between the fiber and matrix and reduced the fiber/matrix interface chemical bond and the matrix toughness [1, 7]. As a result, the ECC-FA mixture exhibited a lower tensile strength and a higher tensile strain/ductility capacity. The

TABLE 6: Mechanical properties of all ECC mixtures.

Mixture designation	Uniaxial tensile properties		Compressive strength (MPa)		Maximum deflection in flexure (mm)
	Maximum average tensile stress (MPa)	Maximum average tensile strain (%)	7 days	28 days	
Reference ECC	3.7	2.7	28.36	31.81	14.50
ECC-FA	3.4	3.3	28.12	30.05	17.02
ECC-SL	4.0	3.2	29.14	32.56	16.12
ECC-FASL	3.9	3.5	29.56	32.84	18.31
ECC-FASL-BA10%	4.0	3.3	30.21	33.12	15.56
ECC-FASL-BA20%	4.4	2.1	30.94	34.91	12.56
ECC-FASL-BA30%	4.7	1.4	30.98	35.79	9.56

substitution of SL increased the tensile strain capacity of the ECC (3.4%) and also enhanced the tensile strength capacity (4.0 MPa) of the ECC compared to those of the reference ECC mixture, which achieved the tensile strain and strength capacity of 2.7% and 3.7 MPa, respectively. The presence of slag particles contributed to the enhancement of the workability of the ECC, resulting in improved fiber dispersion. As a result, a higher enhancement in tensile strain and strength was observed. This tendency can be confirmed by fiber dispersion tests. Figure 5 shows the fiber dispersion analysis results achieved through cross-sectional fluorescence image analysis [10]. From Figure 5, it can be understood that the slag particles provide a driving force for the mortar matrix flow, which led to the improved fiber dispersion.

A comparison of the influence of FS and SL on the tensile behavior of ECC was presented in Figure 4. From Figure 4, it can be understood that the substitution of FA, while enhancing the tensile strain capacity of the ECC, showed a lower tensile strength. In contrast, the ECC with SL showed a higher tensile strength but exhibited a tensile strain of 3.2%, which is 3.13% lower than the ECC developed using FA. From the above results, it can be inferred that the tensile strain and tensile strength of ECC can be improved using FA and SL, respectively. Based on this outcome, the ECC was developed using a ternary binding system (75% cement + 12.5% FA + 12.5% SL) and the stress-strain behavior of the ECC developed using a ternary binding system is shown in Figure 4. As expected, the combination of FA and SL significantly improved the axial strain and strength capacity of the ECC, when compared to the reference ECC and the ECC developed using FA and SL. For example, the ECC developed using a ternary binding system achieved a tensile strain and strength of 3.5% and 3.9 MPa, respectively. On the other hand, the ECC developed using FA achieved a tensile strain and strength of 3.3% and 3.4 MPa, respectively, which are 6.06% and 14.71% lower. Similarly, the ECC developed using SL showed a decrease in tensile strain of 9.38% compared to that of the ECC developed using a ternary binding system. The presence of the FA in the ternary ECC leads to an increase in the frictional bond at the interface between PVA fibers and matrix and the presence of SL improved the fiber dispersion in the ECC. As a result the ECC developed using a ternary binding system exhibited higher ductility and strength than those of the ECC developed

using a binary binding system. Huang et al. [1] achieved an initial cracking strength and strain-hardening capacity of 2.5 MPa and 4.0%, respectively, with the FA substitution of 70%. In similar manner, the test results of [3, 7, 10, 11] demonstrate that the increase in the FA content did not influence the tensile strength of the ECC. Nevertheless, the ECC developed in this study using ternary binder system achieved a strain-hardening capacity and strength of 3.5% and 3.9 MPa, respectively. From this observation, it can be inferred that the ductility and the strength capacity of the ECC can be improved using a combination of different SCMs, particularly with the combination of FA and SL.

Since the ternary binder system exhibited superior performance, the BA substitution was made in the ECC developed using a ternary binder system with substitution rate of 10%, 20%, and 30%. The tensile behavior of the ECC developed using BA is shown in Figure 4. It was observed that all ECC mixtures developed using BA exhibited a strain-hardening behavior; however, substitution of BA can potentially reduce the tensile behavior of the ECC; in addition, the tensile capacity was decreased with the increase in the BA substitution rate. However, the ECC developed using BA with a substitution rate of 10% exhibited a strain capacity that was relatively equal to the strain capacity of ECC-FASL. For instance, the mixture ECC-FASL-BA10% showed a strain value of 3.3%, which is only 6.06% less than that of the ECC-FASL. However, the mixture ECC-FASL-BA30% achieved a strain capacity of 1.4% which is 150.06% less than that of the ECC-FASL. As compared to SS, the particle size of the BA was relatively high, and this particle size significantly affects the fiber dispersion, which is associated with workability (as was discussed earlier). In addition, the higher particle size reduces the available space for fiber dispersion and also increased the matrix fracture toughness by suppressing the margins between cracking strength and fiber bridging capacity and between crack tip toughness and complementary energy of fiber bridging. As a result, it lowers the tensile capacity. The distinctive characteristic of the ECC is the formation of multiple microcracks under tensile loading. Figure 6 shows the crack pattern of mixture ECC-FASL and ECC mixture developed using BA with various substitutions. From Figure 6 it can be understood that the mixture ECC-FASL exhibited a higher number of microcracks, and the crack widths were in the range of 25 μm ~50 μm . Nevertheless, as can be seen

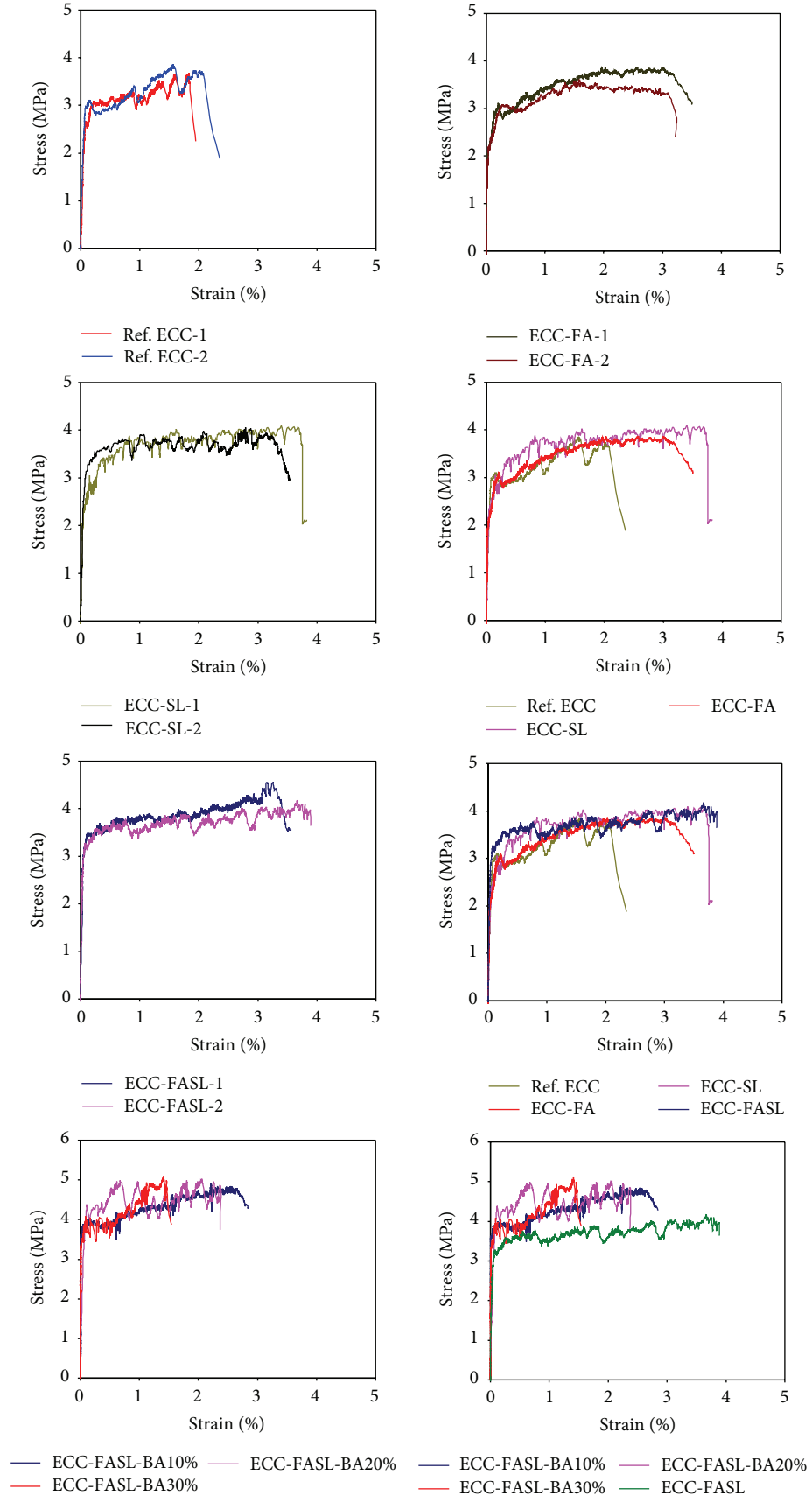


FIGURE 4: Uniaxial tensile stress-strain behavior of all ECC mixtures and comparison.

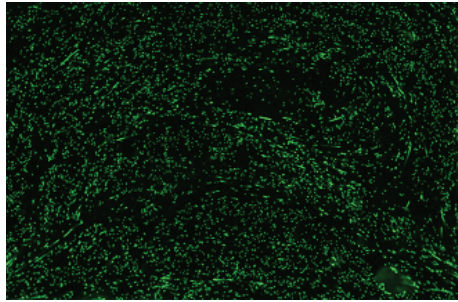


FIGURE 5: Cross-sectional fluorescence image of ECC-SL mixture [10].

from Figure 6, the substitution of BA reduced the number of microcracks; furthermore, the increase in the BA substitution rate leads to a decrease in the number of microcracks and the crack width. The average crack width of the mixtures ECC-FASL-BA10%, ECC-FASL-BA20%, and ECC-FASL-BA30% was less than $25\ \mu\text{m}$. The decrease in the number of microcracks with the substitution may be due to the higher particle size of the BA, and this size increases the matrix fracture toughness by increasing the tortuosity of fracture path along the transition zone between BA and cement paste, thus decreasing the microcracks and the crack width. From this observation, it can be inferred that the replacing of SS by BA with the substitution rate of 10% can be effectively used in ECC preparation. In addition, the decrease in the particle size of BA may have a more beneficial effect on the strain-hardening capacity of ECC.

3.3.2. Compressive Strength. The 28-day compressive strength of all mixtures is presented in Figure 7. It was observed that the substitution of SCMs (FA and SL) did not have any negative effects on the compressive strength of ECC; in addition, the compressive strength of the mixtures developed using binary and ternary cementitious materials was relatively equal to the compressive strength of the reference mixture. It is well documented that the slower secondary hydration of SCMs decreases the compressive strength of the concrete mixtures. However, even though the substitution of SCMs might affect the secondary hydration of ECC, the SCMs contributed to an enhancement of the workability of the ECC, resulting in improved fiber dispersion and this tendency was confirmed by the fiber dispersion tests in the previous chapter. As a result, the compressive strength of the mixtures ECC-FA, ECC-SL, and ECC-FASL was not decreased significantly. From Figure 7, it can be understood that the ECC developed using SL showed a slightly higher strength than that of the FA. At the age of 28 days, the mixture ECC-FA exhibited a strength of 30.05 MPa, whereas the mixture ECC-SL achieved a strength of 32.56 MPa, which is 8.35% higher. As shown in Figure 7, the mixture ECC-FASL showed an enhancement in compressive strength compared to the mixtures ECC-FA and ECC-SL; however the enhancement was not significantly higher. Compared to the mixtures ECC-FA and ECC-SL, the compressive strength of ECC-FASL was enhanced by 9.28% and 1.01%, respectively,

at the age of 28 days. It was observed that the substitution of BA in the ECC-FASL mixture enhanced the compressive strength further; moreover, the increase in the substitution rate of BA increases the compressive strength. This increase in compressive strength may be due to the higher particle size and irregular shape of the BA. The irregular shape of the BA led to stiffer bonding, which may increase the compressive strength. Compared to the mixture ECC-FASL, at the age of 28 days, the mixtures ECC-FASL-BA10%, ECC-FASL-BA20%, and ECC-FASL-BA30% showed a compressive strength of 33.12 MPa, 34.91 MPa, and 35.79 MPa, respectively, which are 1.01%, 6.31%, and 8.98% higher, respectively. It is well documented that the compressive strength of the ECC is inversely proportional to the deformation (i.e., strain-hardening). The compressive strength results obtained in this study showed fairly good agreement. From Table 6, it can be observed that when the 28-day compressive strength of ECC mixtures (ECC-FA, ECC-SL, ECC-FASL, and ECC-FASL-BA10%) is in the range of 33 MPa, or less, the deformation/tensile strain of the ECC mixtures was in the range of 2.7% to 3.5%. Nevertheless, when the ECC mixtures (ECC-FASL-BA20% and ECC-FASL-BA30%) exhibited a compressive strength ranging from 33 MPa to 35 MPa, the deformation of the ECC drastically reduced to range from 1.4 mm to 2.1 mm. From this observation, it can be inferred that, by controlling the compressive strength of ECC, a higher amount of strain-hardening behavior can be obtained. In addition, the replacement of SS by BA with a substitution rate of 10% can be made in ECC preparation without compromising the strain-hardening behavior.

3.3.3. Flexural Deflection Capacity. The deflection of all ECC mixtures corresponding to the ultimate flexural strength is summarized in Table 6. Figure 8 shows the flexural load-deflection behavior of all ECC mixtures. The flexural deflection capacity of the ECC beam reflects the ductile behavior of that ECC mixture [3]. The flexural test results obtained were fairly consistent with the uniaxial tensile behavior and in addition the correlation between the uniaxial strain and the flexural deflection was quite strong, which can be recognized from Table 6. It was observed that all of the ECC mixtures developed using SCMs and BA exhibited a deflection hardening behavior. From Figure 8, it can be understood that the substitution of SCMs in the ECC enhanced the deflection hardening behavior; particularly the deflection hardening behavior of mixtures was ECC-FASL outperformed as is shown in Figure 9. The mixtures ECC-FA, ECC-SL, and ECC-FASL increased their deflection capacity by 17.37%, 10.48%, and 26.27%, respectively, compared to the reference mixture. Comparing the mixtures ECC-FA and ECC-SL with one another, the mixture ECC-FA had the most beneficial effect on deflection capacity. The mixture ECC-FA enhanced its deflection capacity by 5.58%, compared to ECC-SL. The enhancement in deflection capacity is attributed to the improvement in workability resulting from improved fiber dispersion, which led to the improvement in deflection. Compared to the binary binding system, the mixture ECC-FASL exhibited higher flexural strength and deflection capacity. The

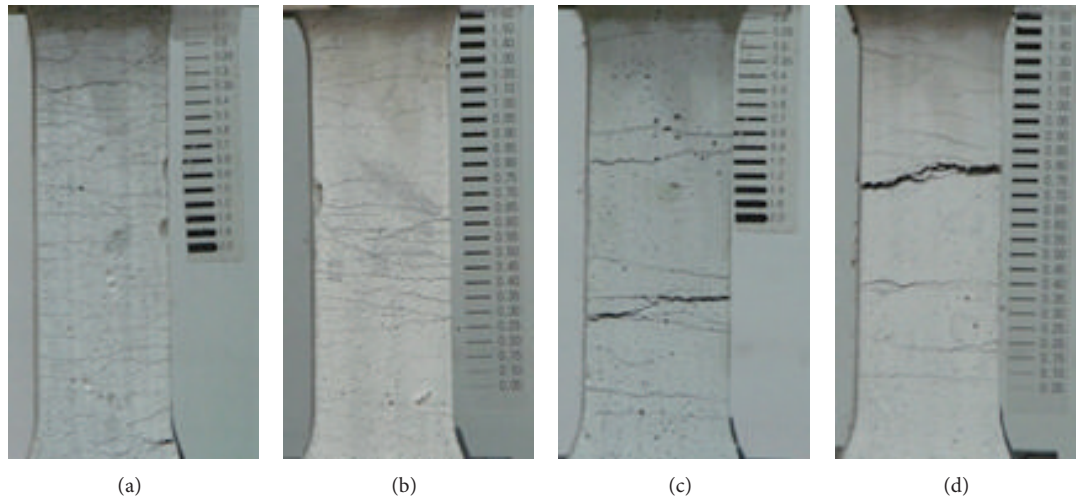


FIGURE 6: Crack behavior/pattern of ECC. (a) ECC-FASL, (b) ECC-FASL-BA10%, (c) ECC-FASL-BA20%, and (d) ECC-FASL-BA30%.

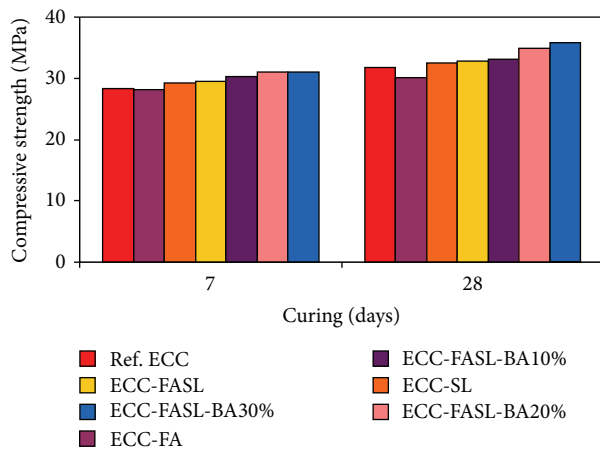


FIGURE 7: Compressive strength of all ECC mixtures and comparison.

mixture ECC-FASL enhanced its deflection capacity by 7.57% and 13.35%, compared to that of the mixtures ECC-FA and ECC-SL, respectively. As discussed earlier, the presence of the FA in the ternary ECC leads to an increase in frictional bond at the interface between PVA fibers and matrix and the presence of SL improved the fiber dispersion in the ECC. As a result the ECC developed using a ternary binding system exhibited a higher deflection capacity than that of the ECC developed using a binary binding system. It was observed that the substitution of BA decreases the deflection capacity of the ECC mixtures; in addition the deflection capacity was decreased with the increase in the substitution rate. However, the deflection capacity of the mixture FASL-BA10% was relatively similar to that of the mixture ECC-FASL and this mixture decreased its deflection capacity by only 17.67% compared to that of the ECC-FASL. The bigger particle size of the BA increased the matrix fracture toughness by increasing the tortuosity of the fracture path along the transition zone

between BA and cement paste. As a result, it decreased the deflection capacity and microcrack formation.

4. Conclusion

An attempt was made to develop the ecoefficient ECC using FA and SL as a binder and a BA as a fine aggregate. The effects of SCMs and BA aggregate on fresh concrete properties and mechanical properties were experimentally investigated through tests including direct tensile test, compressive strength test, and flexural strength test. Based on the results obtained from the seven various ECC mixtures the following conclusions can be made.

- (i) The substitution of SCMs had an advantageous effect on fresh concrete properties; significantly, the mixtures ECC-SL and ECC-FASL had slump flows that were increased by 12.03% and 7.88%, respectively, when compared to the reference mixture.
- (ii) The increased water absorption property of the BA increased the water demand in the ECC, and the irregular shape and big particle size of BA created more friction against the flow of ECC, leading to a decrease in workability with the increase in the BA substitution rate.
- (iii) The presence of deleterious substances in the ECC developed using FA, SL, and BA was very negligible; furthermore, the presence of deleterious substances in BA was reduced with the substitution in ECC.
- (iv) The substitution of FA and SL in ECC potentially enhanced the strain-hardening behavior of the ECC and mixtures ECC-FA and ECC-SL showed a strain capacity of 3.3% and 3.4%, respectively.
- (v) The ECC mixture developed using the combination of FA and SL had significantly improved axial strain and strength capacity compared to those of the individual ECC mixtures developed using FA and SL separately.

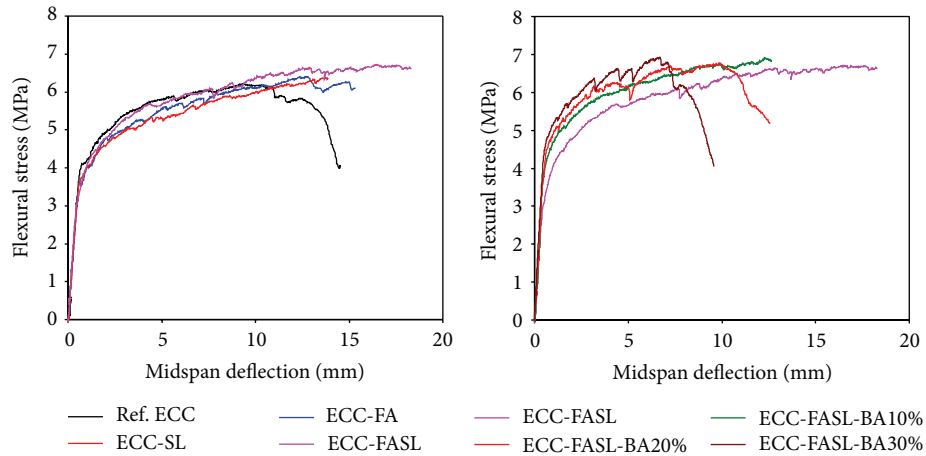


FIGURE 8: Flexural stress-midspan deflection behavior of all ECC mixtures and comparison.

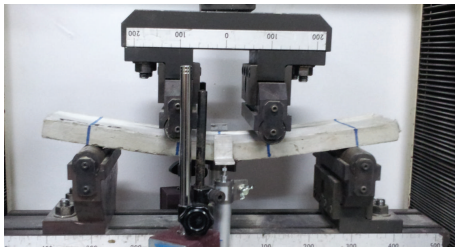


FIGURE 9: Flexural deflection of ECC-FASL mixture.

- (vi) The mixture ECC-FASL had strain capacity that was enhanced by 6.06% and 9.38% compared to the mixtures ECC-FA and ECC-SL, respectively, and it was inferred that the ductility and the strength capacity of the ECC can be improved by using a combination of different SCMs, particularly with the combination of FA and SL.
- (vii) The substitution of BA adversely affects the strain capacity of the ECC; moreover, the increase in the substitution rate of BA further reduces the strain capacity. However, mixture ECC-FASL-BA10% showed a strain value of 3.3%, which is only 6.06% less than the ECC-FASL.
- (viii) The substitution of SCMs did not affect the compressive strength of the ECC; moreover, the SCMs increased the fiber distribution in ECC and achieved a relatively equal compressive strength to the reference mixture. In addition, the substitution of BA increased the compressive strength of ECC.
- (ix) Compared to the reference mixture, the ECC mixture developed using SCMs showed an improved deflection capacity; however, the substitution of BA reduces the deflection capacity of the ECC beam. In addition the trend of deflection capacity was fairly similar to that of uniaxial tensile capacity.

- (x) Based on the test results, it is recommended that a combination of SCMs (12.5% FA and 12.5% SL) and the BA aggregate with the substitution rate of 10% can be effectively used in ECC preparation.

Conflict of Interests

The authors declare that there is no conflict of interests regarding the publication of this paper.

Acknowledgments

This work (2014-0750-01) was supported by research fund of Chungnam National University. The financial support is gratefully acknowledged.

References

- [1] X. Huang, R. Ranade, W. Ni, and V. C. Li, "Development of green engineered cementitious composites using iron ore tailings as aggregates," *Construction and Building Materials*, vol. 44, pp. 757–764, 2013.
- [2] Y. Zhu, Z. Zhang, Y. Yang, and Y. Yao, "Measurement and correlation of ductility and compressive strength for engineered cementitious composites (ECC) produced by binary and ternary systems of binder materials: fly ash, slag, silica fume and cement," *Construction and Building Materials*, vol. 68, pp. 192–198, 2014.
- [3] N. M. Altwaitir, M. A. Megat Johari, and S. F. Saiyid Hashim, "Flexural performance of green engineered cementitious composites containing high volume of palm oil fuel ash," *Construction and Building Materials*, vol. 37, pp. 518–525, 2012.
- [4] V. Saraswathy and H.-W. Song, "Corrosion performance of rice husk ash blended concrete," *Construction and Building Materials*, vol. 21, no. 8, pp. 1779–1784, 2007.
- [5] V. Saraswathy, S. Muralidharan, K. Thangavel, and S. Srinivasan, "Influence of activated fly ash on corrosion-resistance and strength of concrete," *Cement & Concrete Composites*, vol. 25, no. 7, pp. 673–680, 2003.

- [6] R. O. Lane and J. F. Best, "Properties and use of fly ash on Portland cement concrete," *Concrete International*, vol. 4, no. 7, pp. 81–92, 1982.
- [7] M. Şahmaran and V. C. Li, "Durability properties of micro-cracked ECC containing high volumes fly ash," *Cement and Concrete Research*, vol. 39, no. 11, pp. 1033–1043, 2009.
- [8] N.-Q. Feng, Y.-X. Shi, and T.-Y. Hao, "Influence of ultra-fine powder on the fluidity and strength of cement paste," *Advances in Cement Research*, vol. 12, no. 3, pp. 89–95, 2000.
- [9] Z. Yu, Y. Yang, X. Gao, H. Deng, and Y. Yao, "Mechanical properties of engineered cementitious composites with high volume fly ash," *Journal of Wuhan University of Technology*, vol. 24, pp. 166–170, 2009.
- [10] J.-K. Kim, J.-S. Kim, G. J. Ha, and Y. Y. Kim, "Tensile and fiber dispersion performance of ECC (engineered cementitious composites) produced with ground granulated blast furnace slag," *Cement and Concrete Research*, vol. 37, no. 7, pp. 1096–1105, 2007.
- [11] S. Wang and V. C. Li, "Engineered cementitious composites with high-volume fly ash," *ACI Materials Journal*, vol. 104, no. 3, pp. 233–241, 2007.
- [12] Ministry of Environment (Korea), *Solid Waste Process Test Methods*, 2007.
- [13] Ministry of Government Legislation (Korea), *Appendix 1 of the Enforcement Rule of the Wastes Control Act*, Ministry of Government Legislation (Korea), 2007.
- [14] H.-J. Kong, S. G. Bike, and V. C. Li, "Constitutive rheological control to develop a self-consolidating engineered cementitious composite reinforced with hydrophilic poly(vinyl alcohol) fibers," *Cement & Concrete Composites*, vol. 25, no. 3, pp. 333–341, 2003.
- [15] Korean Standards Association, *Standard Test Method for Compressive Strength of Concrete, KS F 2405*, Korean Standards Association, Seoul, Republic of Korea, 2010.
- [16] Korean Standards Association, *Method of Test for Flexural Strength of Concrete, KS F 2408*, Korean Standards Association, 2010.

Research Article

Application of a Neural Network Model for Prediction of Wear Properties of Ultrahigh Molecular Weight Polyethylene Composites

Halil Ibrahim Kurt and Murat Oduncuoglu

Technical Sciences, University of Gaziantep, 27310 Gaziantep, Turkey

Correspondence should be addressed to Halil Ibrahim Kurt; hiakurt@gmail.com

Received 7 December 2014; Revised 25 May 2015; Accepted 31 May 2015

Academic Editor: Togay Ozbakkaloglu

Copyright © 2015 H. I. Kurt and M. Oduncuoglu. This is an open access article distributed under the Creative Commons Attribution License, which permits unrestricted use, distribution, and reproduction in any medium, provided the original work is properly cited.

In the current study, the effect of applied load, sliding speed, and type and weight percentages of reinforcements on the wear properties of ultrahigh molecular weight polyethylene (UHMWPE) was theoretically studied. The extensive experimental results were taken from literature and modeled with artificial neural network (ANN). The feed forward (FF) back-propagation (BP) neural network (NN) was used to predict the dry sliding wear behavior of UHMWPE composites. Eleven input vectors were used in the construction of the proposed NN. The carbon nanotube (CNT), carbon fiber (CF), graphene oxide (GO), and wollastonite additives are the main input parameters and the volume loss is the output parameter for the developed NN. It was observed that the sliding speed and applied load have a stronger effect on the volume loss of UHMWPE composites in comparison to other input parameters. The proper condition for achieving the desired wear behaviors of UHMWPE by tailoring the weight percentage and reinforcement particle size and composition was presented. The proposed NN model and the derived explicit form of mathematical formulation show good agreement with test results and can be used to predict the volume loss of UHMWPE composites.

1. Introduction

Polymers have high elasticity, good process ability, and reasonable strength, so they can be called multifunctional materials. Polymer-based composites are widely used in various applications and many fields, including microelectronics, biomedical engineering, electrical devices, and filtration [1–5]. Polymer-based nanocomposites formed by adding a small amount of micro- and nanoparticles to the matrix have created great interest in engineering and science. Composites with nanoparticles display superior thermal, electrical, and mechanical properties [6–8]. The properties of the materials have been improved by adding fillers such as graphite nanosheets, CNTs, and boron nitride (BN) to polymer matrices [9–11].

UHMWPE is widely used as the matrix material in the production of polymer matrix nanocomposites. UHMWPE has so many excellent properties such as being light in weight, corrosion resistant, biocompatible, and self-lubricant. Due to

these special properties and several advantages, it has gained worldwide acceptance and is widely used in military, industrial, medical, and consumer applications involving wear and friction [12, 13]. UHMWPE is a complicated material, meaning that several factors can be responsible for wear. One method of increasing the wear resistance of UHMWPE is the adding of fiber fillers and nano- and microparticles in the composition and they are called UHMWPE composites. Theoretically, polymers can be strengthened by molecular alignment of the material. When sliding loads are applied to a specimen of UHMWPE, the molecular chains begin to straighten, be untangled, and align in load direction, and the strength tends to increase in this direction. UHMWPE composites can also be further engineered at a micro- or nanometer length scale by blending polymer powder resin with micro- or nanoparticles and fibers before consolidation. UHMWPE composites were reinforced by TiO₂, CNT, kaolin, CF, hydroxyapatite, Al₂O₃, zirconium particles [14–18], and so forth. The works have demonstrated that

the addition of optimum amount of nano- and microfibers and ceramic particles into UHMWPE would significantly affect the wear rate under sliding wear conditions.

Recently, the material properties with their own characteristics, applications, advantages, and limitations are important factors for designers and materials engineers. Due to UHMWPE's complex behaviors, finding an appropriate model for determining the wear properties of UHMWPE can be challenging. The effect of type and weight percentage of fibers and particles in composition and one of the operation parameters such as applied load and sliding speed on wear behavior of UHMWPE was investigated separately. In selecting additive materials, type and percentage for an application are important. The experimental determination of additives for desired wear behavior of UHMWPE composites is cost- and time-consuming. ANN modeling has been used to minimize the experimental study and predict the wear characteristics to establish a correlation between the wear properties and operation parameters of UHMWPE composites. Therefore, the main aim is to determine and understand the effect of type, size, and weight percentage of different reinforcement and variables in operation condition on dry sliding wear properties of UHMWPE composites.

2. Neural Network

The ANNs are a methodology in different applications of materials including prediction of tribological and mechanical properties and were used by many researchers [19–24]. Venkata Rao et al. [25] used ANN to predict surface roughness, tool wear, and amplitude of work piece vibration. They reported that the neural network can help in the selection of proper cutting parameters to reduce tool vibration and tool wear and reduce surface roughness. Gyurova and Friedrich [26] for the prediction of sliding friction and wear properties of polymer composites used ANN and stated that the prediction profiles for the characteristic tribological properties of the ANN exhibited very good agreement with the measured results. Li et al. [27] modeled the sliding wear resistance of the Ni–TiN coatings by using ANN. They explained that the proposed ANN model shows an error of approximately 4.2% and can effectively predict sliding wear resistance of Ni–TiN nanocomposite coatings.

An ANN can be defined as a massively parallel distributed processor storing experiential knowledge and making it available for use [28]. NN is a computational framework that is inspired by biological neural systems. Figure 1 shows the input layer, hidden layer, and the output layer in NN system [29]. It consists of a number of interconnected simple processing units called artificial neurons. The basic structure of an artificial neuron was shown in Figure 2. In ANN modeling, the networks include artificial neurons that consist of three main components, namely, weights, bias, and transfer function.

Each neuron receives inputs, attached with a weight w_i , which shows the connection strength for that input for each connection. Each input is multiplied by the corresponding weight of the neuron connection. Next, a bias (b_i) value is

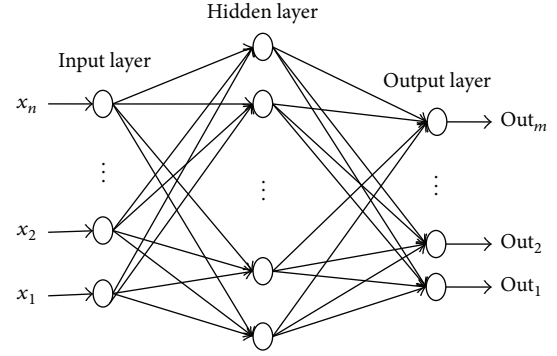


FIGURE 1: A typical neural network image.

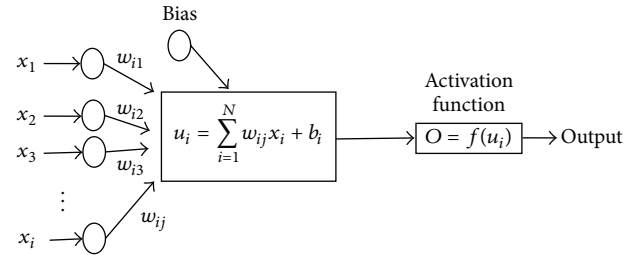


FIGURE 2: The basic structure of an artificial neuron [43].

added to the summation of inputs and corresponding weights (u) according to the following equation:

$$u_i = \sum_{j=1}^H w_{ij}x_j + b_i. \quad (1)$$

The summation u_i is converted as output with an activation (transfer) function, $F(u_i)$, yielding a value called the unit's "activation," as in the following formula:

$$O = f(u_i). \quad (2)$$

3. Results and Discussion

NNs are commonly classified according to training algorithms (supervised and unsupervised) and network topology (feedback and feed forward) [30]. BP learning algorithm (Levenberg-Marquardt (Trainlm)) is the most popular and effective supervised learning method used in this study [31, 32]. Sigmoid function, which joins curvilinear, linear, and constant behavior depending on the values of the input, is commonly used as transfer function in NNs [33, 34]. The weight loss of the composites was converted to volume loss, V , by dividing it with the specific composite density by the following formula [35]:

$$V = \frac{(W_1 - W_2)}{d}, \quad (3)$$

where $W_{1,2}$ is the weight loss before and after wear test, respectively, and d is the density of the composites. In an ANN model, each of the input and output variables was scaled

to fall into a range of 0 to 1, using the following scaling formula:

$$x_N = \frac{x - x_{\min}}{x_{\max} - x_{\min}}, \quad (4)$$

where x_N is the normalized value of the parameter x and x_{\max} and x_{\min} are the maximum and minimum values of this parameter, respectively. Output values resulted from ANN also in the range [0,1] and transformed to its equivalent values based on reverse method of normalization technique [36]. The unnormalized method is as

$$x = x_N (x_{\max} - x_{\min}) + x_{\min}. \quad (5)$$

An extensive literature survey has been performed for collecting the experimental data. Two main processing phases of NN include training and testing. The training process is the adjustment of weights and biases in order to obtain the output through applying a proper method. Hence, the experimental results were divided in two sets, training and testing sets. The training and testing data were randomly selected among experimental results as shown in the Appendix. The input (independent) variables are UHMWPE (wt.%), ZnO (wt.%), zeolite (wt.%), CNT (wt.%), CF (wt.%), GO (wt.%), wollastonite (wt.%), size of ZnO (μm) and zeolite (μm), load (N), and sliding speed (m/s), respectively. The output or dependent variable is volume loss (mm^3).

The network architecture and parameters affect the performance of NN. One of the most important duties in NN works is the determination of the numbers of layers and neurons in the hidden layers. In other words, the ANN parameters, such as the number of neurons in the input, network architecture, hidden layer, output layer, learning algorithm, and transfer function, are to be selected for developing an ANN model. There is no well-defined procedure to find the optimal parameter settings and network architecture. The trial and error approach with various numbers of neurons in one hidden layer was used to determine the number of neurons. It was observed that the optimal NN architecture with logistic sigmoid transfer function was 11–12–1 NN architecture. Figure 3 shows the optimal architecture of NN. In the present study, the NN model consists of three layers, which comprises an input layer, a hidden layer, and an output layer.

The performance of NN was evaluated by the correlation coefficient (R) as in the following expression:

$$R = \frac{\text{cov}(y_t, y'_t)}{\sqrt{\text{var}(y_t) \cdot \text{var}(y'_t)}}. \quad (6)$$

Mean absolute error (MAE) and mean square error (MSE) were used as error evaluation criteria in order to

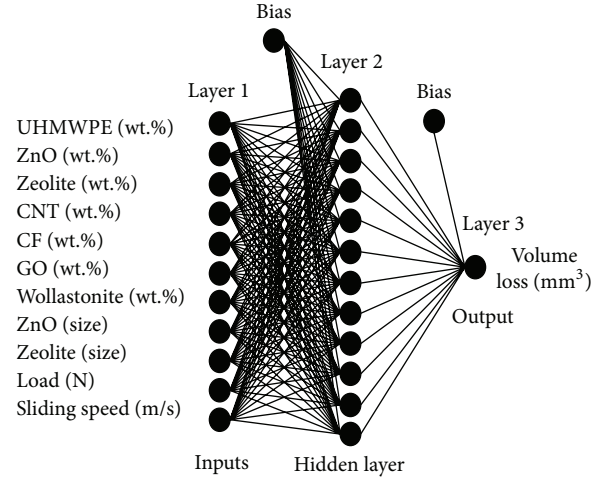


FIGURE 3: Optimal NN selection process.

TABLE 1: Statistical parameters of training and testing sets.

Datasets	R	MAE	MSE
Training set	0.9400	3.63	0.389
Testing set	0.9176	4.07	0.412

facilitate the comparisons between predicted values and desired values according to the following equations:

$$\text{MAE} = \frac{1}{N} \sum_{i=1}^N |t_i - \hat{t}_i|, \quad (7)$$

$$\text{MSE} = \left(\frac{1}{N} \sum_{i=1}^N |t_i - \hat{t}_i| \right)^2,$$

where N is the total number of the datasets and t_i and \hat{t}_i are the experimental value and predicted output value from the neural network model for a given input, respectively.

The statistical data for the training and testing sets were shown in Table 1. The correlation of NN model with the experimental data for these sets was also shown in Figures 4 and 5.

The correlation of coefficients in training and testing sets is 0.9400 and 0.9176 which means that the performance of network model is acceptable. MAE and MSE values of volume loss are 3.63 and 0.389 for training set and 4.07 and 0.412 for testing set. If the MSE reaches zero, the performance of model is regarded as being excellent [37]. Comparison between the test and predicted values shows that the prediction of the proposed NN model is in good agreement with the experimental data and all the errors are within acceptable ranges.

R^2 values of training and testing sets are 0.8837 and 0.842, respectively. R^2 value compares the accuracy of the model to the accuracy of a trivial assessment model. A high R^2 value ($R^2 = 1$) tells that all points lie exactly on the curve with no scatter and the results have the perfect correlation. It is clear that all the values are higher than 0.84.

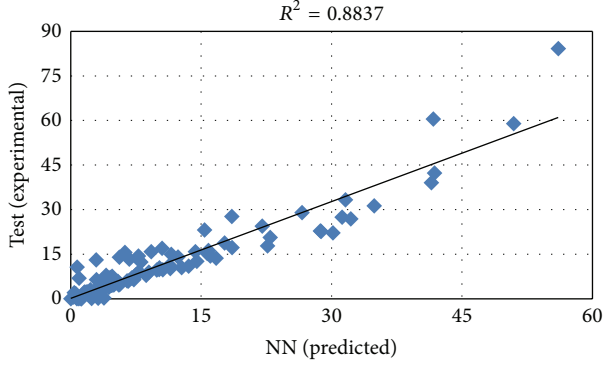


FIGURE 4: Correlation of NN and experimental data for training set.

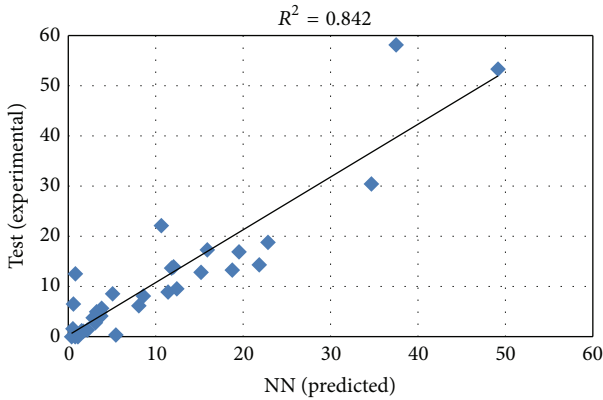


FIGURE 5: Correlation of NN and experimental data for testing set.

The wear rate of the composites is strongly influenced by many factors, such as the shape and content of reinforcement, operating conditions, the morphologies of surfaces, physical morphology between the matrix material and reinforcement, the bond strength at the matrix/reinforcement interface, and homogeneous distribution of reinforcement [38, 39]. It is difficult to find the effect of each factor on the wear volume loss of the composites and it needs extensive studies. In the current work, the operating parameters and weight percentages and sizes of reinforcement were quantified. Nevertheless, R and R^2 values of training set indicate that the learning ability of NN is well enough (Table 1 and Figure 4). The effects of the other parameters can be investigated in order to increase the prediction rate of the proposed NN model. It was concluded that the proposed NN model can predict the volume loss of UHMWPE composites containing different particles with size and weight percentages with high accuracy and reliability.

The sensitivity of wear volume loss of UHMWPE composites of each input variable from the minimum to the maximum was given in Figure 6. The sliding speed is an example of factors that can contribute to wear. Our theoretical results demonstrated that the sliding speed has the greatest effect on volume loss of UHMWPE among all input parameters. The different sliding speeds can result in different wear properties. The higher the loading speed is, the more the time UHMWPE will spend in the elastic deformation stage. It is clear that any change in sliding speed, load, UHMWPE

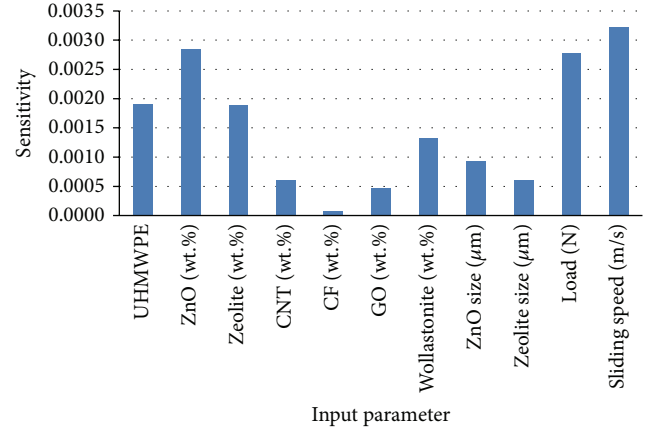


FIGURE 6: Sensitivity of input vectors.

(wt.%), ZnO (wt.%), and zeolite (wt.%) will be affected by the volume loss of UHMWPE in comparison to all the other input parameters.

4. Formulation of NN Model

The main focus is to obtain the explicit formulation of the volume loss as a function of input variables under limited conditions. The ANN models emerged as good candidates for mathematical wear models due to their capabilities in nonlinear behavior, learning from experimental data, and generalization [40]. Hutching's group [41] and Basavarajappa et al. [42] presented pioneering investigations of ANN techniques for predicting tribological parameters.

As a result, the wear behavior under various parameters was investigated to predict and analyze the relationship between the reinforcements and volume loss of UHMWPE composites. The volume loss (X) was determined by using the formula

$$X = 84.185617 * \left(\frac{1}{1 + e^{-v}} \right) + 0.212915, \quad (8)$$

where the parameters are

$$\begin{aligned} v = & (-2.1888) * \left(\frac{1}{1 + e^{-u1}} \right) + (1.5322) \\ & * \left(\frac{1}{1 + e^{-u2}} \right) + (5.8748) * \left(\frac{1}{1 + e^{-u3}} \right) \\ & + (4.2619) * \left(\frac{1}{1 + e^{-u4}} \right) + (-0.6620) \\ & * \left(\frac{1}{1 + e^{-u5}} \right) + (-2.9341) * \left(\frac{1}{1 + e^{-u6}} \right) \\ & + (-0.6885) * \left(\frac{1}{1 + e^{-u7}} \right) + (-0.6696) \\ & * \left(\frac{1}{1 + e^{-u8}} \right) + (0.9414) * \left(\frac{1}{1 + e^{-u9}} \right) \\ & + (-5.8760) * \left(\frac{1}{1 + e^{-u10}} \right) + (-6.0830) \\ & * \left(\frac{1}{1 + e^{-u11}} \right) + (-2.7599) * \left(\frac{1}{1 + e^{-u12}} \right) \\ & + (-0.7807), \end{aligned}$$

$$\begin{aligned}
u_1 &= (-0.7182 * A_1) + (-0.5842 * A_2) && + (0.6221 * A_9) + (-0.2125 * A_{10}) \\
&+ (-0.7211 * A_3) + (0.5435 * A_4) && + (-0.3791 * A_{11}) + (0.1155), \\
&+ (0.7793 * A_5) + (-0.1909 * A_6) \\
&+ (0.4002 * A_7) + (0.8474 * A_8) \\
&+ (-0.7288 * A_9) + (-0.2069 * A_{10}) \\
&+ (-1.9995 * A_{11}) + (-0.0394), \\
u_2 &= (0.7896 * A_1) + (-0.2539 * A_2) \\
&+ (0.1801 * A_3) + (-0.1505 * A_4) \\
&+ (0.0765 * A_5) + (-0.2878 * A_6) \\
&+ (0.1697 * A_7) + (0.5636 * A_8) \\
&+ (-0.0203 * A_9) + (-0.8914 * A_{10}) \\
&+ (1.9869 * A_{11}) + (-0.1818), \\
u_3 &= (-2.3087 * A_1) + (0.4084 * A_2) \\
&+ (0.4903 * A_3) + (-0.8781 * A_4) \\
&+ (-1.3043 * A_5) + (-0.9548 * A_6) \\
&+ (-0.6670 * A_7) + (2.7410 * A_8) \\
&+ (-2.1091 * A_9) + (3.2012 * A_{10}) \\
&+ (1.8193 * A_{11}) + (-3.4212), \\
u_4 &= (2.0533 * A_1) + (-3.2323 * A_2) \\
&+ (0.7227 * A_3) + (0.0295 * A_4) \\
&+ (-0.5151 * A_5) + (0.0588 * A_6) \\
&+ (-0.7574 * A_7) + (-0.2123 * A_8) \\
&+ (-0.6447 * A_9) + (4.5743 * A_{10}) \\
&+ (0.5803 * A_{11}) + (-0.8036), \\
u_5 &= (0.3405 * A_1) + (-0.2333 * A_2) \\
&+ (0.2794 * A_3) + (0.3565 * A_4) \\
&+ (0.4379 * A_5) + (-0.0345 * A_6) \\
&+ (-0.0986 * A_7) + (0.0275 * A_8) \\
&+ (0.6663 * A_9) + (-0.3537 * A_{10}) \\
&+ (-0.4749 * A_{11}) + (-0.2079), \\
u_6 &= (0.5510 * A_1) + (-2.2037 * A_2) \\
&+ (0.1234 * A_3) + (0.3718 * A_4) \\
&+ (0.3239 * A_5) + (0.5667 * A_6) \\
&+ (-0.2435 * A_7) + (-0.7447 * A_8) \\
&+ (1.1467 * A_9) + (-2.4374 * A_{10}) \\
&+ (0.0093 * A_{11}) + (0.0879), \\
u_7 &= (0.1883 * A_1) + (-0.4882 * A_2) \\
&+ (0.0982 * A_3) + (0.1593 * A_4) \\
&+ (-0.0599 * A_5) + (0.5295 * A_6) \\
&+ (0.3879 * A_7) + (-0.2778 * A_8) \\
&+ (0.7380 * A_1) + (0.0758 * A_2) + (0.4082 * A_3) \\
&+ (-0.0235 * A_4) + (0.2302 * A_5) \\
&+ (-0.1718 * A_6) + (0.0265 * A_7) \\
&+ (1.2521 * A_8) + (-0.4670 * A_9) \\
&+ (1.0054 * A_{10}) + (0.8061 * A_{11}) \\
&+ (0.5412), \\
u_8 &= (0.2707 * A_1) + (0.7648 * A_2) + (0.2012 * A_3) \\
&+ (-0.4448 * A_4) + (-0.5107 * A_5) \\
&+ (-0.2796 * A_6) + (-0.1827 * A_7) \\
&+ (0.1138 * A_8) + (-0.6849 * A_9) \\
&+ (0.4180 * A_{10}) + (0.2120 * A_{11}) \\
&+ (-0.4322), \\
u_9 &= (-1.8196 * A_1) + (0.3943 * A_2) \\
&+ (-0.3793 * A_3) + (-0.1015 * A_4) \\
&+ (-0.6886 * A_5) + (-0.0171 * A_6) \\
&+ (-0.0900 * A_7) + (2.7289 * A_8) \\
&+ (-0.3999 * A_9) + (-6.8627 * A_{10}) \\
&+ (1.5364 * A_{11}) + (-1.7102), \\
u_{10} &= (-0.0124 * A_1) + (-2.2261 * A_2) \\
&+ (-0.5712 * A_3) + (0.1810 * A_4) \\
&+ (0.7198 * A_5) + (-0.3316 * A_6) \\
&+ (0.4865 * A_7) + (-0.8473 * A_8) \\
&+ (-1.0742 * A_9) + (4.8908 * A_{10}) \\
&+ (-1.9057 * A_{11}) + (-0.4736), \\
u_{11} &= (-0.1888 * A_1) + (-2.3874 * A_2) \\
&+ (-0.1633 * A_3) + (0.2577 * A_4) \\
&+ (0.4452 * A_5) + (0.0305 * A_6) \\
&+ (0.0384 * A_7) + (-0.9836 * A_8) \\
&+ (0.0058 * A_9) + (-2.1195 * A_{10}) \\
&+ (2.0152 * A_{11}) + (-0.8806), \\
u_{12} &= (0.1883 * A_1) + (-0.4882 * A_2) \\
&+ (0.0982 * A_3) + (0.1593 * A_4) \\
&+ (-0.0599 * A_5) + (0.5295 * A_6) \\
&+ (0.3879 * A_7) + (-0.2778 * A_8)
\end{aligned}
\tag{9}$$

where $A_1, A_2, A_3, A_4, A_5, A_6, A_7, A_8, A_9, A_{10}$, and A_{11} are normalized values of UHMWPE, ZnO (wt.%), zeolite (wt.%), CNT (wt.%), CF (wt.%), GO (wt.%), wollastonite (wt.%), size of ZnO and zeolite (μm), load (N), and sliding speed (m/s), respectively.

Using derived formulation, the wear volume loss of UHMWPE composite with the size of $1\ \mu\text{m}$ and 5 wt.% ZnO

TABLE 2: Dataset used NN model.

Reference	UHMWPE	ZnO (wt.%)	Zeolite (wt.%)	CNT (wt.%)	CF (wt.%)	GO (wt.%)	Wollastonite (wt.%)	Load (N)	Sliding speed (m/s)	Volume loss (mm ³)
Chang et al. [44]	100	—	—	—	—	—	—	10	0,033	5,699
	95	5	—	—	—	—	—	10	0,033	3,093
	90	10	—	—	—	—	—	10	0,033	2,075
	85	15	—	—	—	—	—	10	0,033	2,329
	80	20	—	—	—	—	—	10	0,033	2,413
	95	5	—	—	—	—	—	10	0,033	3,781
	90	10	—	—	—	—	—	10	0,033	2,218
	85	15	—	—	—	—	—	10	0,033	1,962
	80	20	—	—	—	—	—	10	0,033	2,091
	100	—	—	—	—	—	—	20	0,033	13,333
	95	5	—	—	—	—	—	20	0,033	6,101
	90	10	—	—	—	—	—	20	0,033	6,440
	85	15	—	—	—	—	—	20	0,033	6,927
	80	20	—	—	—	—	—	20	0,033	6,541
	95	5	—	—	—	—	—	20	0,033	6,358
	90	10	—	—	—	—	—	20	0,033	4,150
	85	15	—	—	—	—	—	20	0,033	4,965
	80	20	—	—	—	—	—	20	0,033	4,611
	100	—	—	—	—	—	—	30	0,033	15,914
	95	5	—	—	—	—	—	30	0,033	10,225
	90	10	—	—	—	—	—	30	0,033	9,159
	85	15	—	—	—	—	—	30	0,033	8,582
	80	20	—	—	—	—	—	30	0,033	7,613
	95	5	—	—	—	—	—	30	0,033	7,905
	90	10	—	—	—	—	—	30	0,033	4,722
	85	15	—	—	—	—	—	30	0,033	7,172
	80	20	—	—	—	—	—	30	0,033	4,986
	100	—	—	—	—	—	—	10	0,368	22,151
	95	5	—	—	—	—	—	10	0,368	14,435
	90	10	—	—	—	—	—	10	0,368	13,094
	85	15	—	—	—	—	—	10	0,368	12,566
	80	20	—	—	—	—	—	10	0,368	10,723
	95	5	—	—	—	—	—	10	0,368	14,092
	90	10	—	—	—	—	—	10	0,368	9,874
	85	15	—	—	—	—	—	10	0,368	12,382
	80	20	—	—	—	—	—	10	0,368	8,096
	100	—	—	—	—	—	—	20	0,368	27,742
	95	5	—	—	—	—	—	20	0,368	18,818
	90	10	—	—	—	—	—	20	0,368	17,029
	85	15	—	—	—	—	—	20	0,368	15,631
80	20	—	—	—	—	—	20	0,368	13,993	
95	5	—	—	—	—	—	20	0,368	16,326	
90	10	—	—	—	—	—	20	0,368	12,665	
85	15	—	—	—	—	—	20	0,368	13,669	
80	20	—	—	—	—	—	20	0,368	11,312	
100	—	—	—	—	—	—	30	0,368	29,032	

TABLE 2: Continued.

Reference	UHMWPE	ZnO (wt.%)	Zeolite (wt.%)	CNT (wt.%)	CF (wt.%)	GO (wt.%)	Wollastonite (wt.%)	Load (N)	Sliding speed (m/s)	Volume loss (mm ³)
	95	5	—	—	—	—	—	30	0,368	22,255
	90	10	—	—	—	—	—	30	0,368	17,816
	85	15	—	—	—	—	—	30	0,368	17,347
	80	20	—	—	—	—	—	30	0,368	15,923
	95	5	—	—	—	—	—	30	0,368	17,271
	90	10	—	—	—	—	—	30	0,368	13,309
	85	15	—	—	—	—	—	30	0,368	15,324
	80	20	—	—	—	—	—	30	0,368	12,867
	100	—	—	—	—	—	—	10	1,022	23,226
	95	5	—	—	—	—	—	10	1,022	14,435
	90	10	—	—	—	—	—	10	1,022	13,952
	85	15	—	—	—	—	—	10	1,022	10,482
	80	20	—	—	—	—	—	10	1,022	9,543
	95	5	—	—	—	—	—	10	1,022	14,350
	90	10	—	—	—	—	—	10	1,022	13,666
	85	15	—	—	—	—	—	10	1,022	15,018
	80	20	—	—	—	—	—	10	1,022	9,704
	100	—	—	—	—	—	—	20	1,022	27,527
	95	5	—	—	—	—	—	20	1,022	31,277
	90	10	—	—	—	—	—	20	1,022	22,682
	85	15	—	—	—	—	—	20	1,022	20,657
	80	20	—	—	—	—	—	20	1,022	18,818
	95	5	—	—	—	—	—	20	1,022	26,895
	90	10	—	—	—	—	—	20	1,022	22,825
	85	15	—	—	—	—	—	20	1,022	24,458
	80	20	—	—	—	—	—	20	1,022	16,942
	100	—	—	—	—	—	—	30	1,022	53,333
	95	5	—	—	—	—	—	30	1,022	84,207
	90	10	—	—	—	—	—	30	1,022	58,958
	85	15	—	—	—	—	—	30	1,022	60,500
	80	20	—	—	—	—	—	30	1,022	58,171
	95	5	—	—	—	—	—	30	1,022	42,361
	90	10	—	—	—	—	—	30	1,022	39,067
	85	15	—	—	—	—	—	30	1,022	30,465
	80	20	—	—	—	—	—	30	1,022	33,348
Chang et al. [45]	100	—	—	—	—	—	—	10	0,209	2,800
	90	—	10	—	—	—	—	10	0,209	2,200
	80	—	20	—	—	—	—	10	0,209	2,200
	100	—	—	—	—	—	—	20	0,209	5,000
	90	—	10	—	—	—	—	20	0,209	3,600
	80	—	20	—	—	—	—	20	0,209	3,500
	100	—	—	—	—	—	—	30	0,209	5,900
	90	—	10	—	—	—	—	30	0,209	4,700
	80	—	20	—	—	—	—	30	0,209	4,700
	100	—	—	—	—	—	—	10	0,419	4,700
	90	—	10	—	—	—	—	10	0,419	3,900
	80	—	20	—	—	—	—	10	0,419	3,100

TABLE 2: Continued.

Reference	UHMWPE	ZnO (wt.%)	Zeolite (wt.%)	CNT (wt.%)	CF (wt.%)	GO (wt.%)	Wollastonite (wt.%)	Load (N)	Sliding speed (m/s)	Volume loss (mm ³)
	100	—	—	—	—	—	—	20	0,419	6,500
	90	—	10	—	—	—	—	20	0,419	6,000
	80	—	20	—	—	—	—	20	0,419	5,200
	100	—	—	—	—	—	—	30	0,419	8,100
	90	—	10	—	—	—	—	30	0,419	7,900
	80	—	20	—	—	—	—	30	0,419	6,200
	100	—	—	—	—	—	—	10	0,838	8,000
	90	—	10	—	—	—	—	10	0,838	5,900
	80	—	20	—	—	—	—	10	0,838	5,000
	100	—	—	—	—	—	—	20	0,838	9,800
	90	—	10	—	—	—	—	20	0,838	9,000
	80	—	20	—	—	—	—	20	0,838	7,000
	100	—	—	—	—	—	—	30	0,838	11,000
	90	—	10	—	—	—	—	30	0,838	10,500
	80	—	20	—	—	—	—	30	0,838	8,900
Zoo et al. [18]	100	—	—	—	—	—	—	5	0,300	0,376
	99,9	—	—	0,1	—	—	—	5	0,300	0,268
	99,8	—	—	0,2	—	—	—	5	0,300	0,134
	99,5	—	—	0,5	—	—	—	5	0,300	0,021
Dangsheng [14]	100	—	—	—	—	—	—	196	0,420	1,820
	95	—	—	—	5	—	—	196	0,420	1,400
	90	—	—	—	10	—	—	196	0,420	1,350
	85	—	—	—	15	—	—	196	0,420	1,110
	80	—	—	—	20	—	—	196	0,420	0,730
	70	—	—	—	30	—	—	196	0,420	0,590
Tai et al. [46]	100	—	—	—	—	—	—	5	0,090	0,043
	99,9	—	—	—	—	0,1	—	5	0,090	0,038
	99,7	—	—	—	—	0,3	—	5	0,090	0,033
	99,3	—	—	—	—	0,7	—	5	0,090	0,028
	99	—	—	—	—	1	—	5	0,090	0,028
	98	—	—	—	—	2	—	5	0,090	0,026
	97	—	—	—	—	3	—	5	0,090	0,025
Tong et al. [47]	100	—	—	—	—	—	—	120	0,530	1,73
	95	—	—	—	—	—	5	120	0,530	1,31
	90	—	—	—	—	—	10	120	0,530	1,2
	85	—	—	—	—	—	15	120	0,530	1,58
	80	—	—	—	—	—	20	120	0,530	1,8
	90	—	—	—	—	—	10	40	0,530	0,25
	90	—	—	—	—	—	10	80	0,530	0,7
	90	—	—	—	—	—	10	160	0,530	2,28

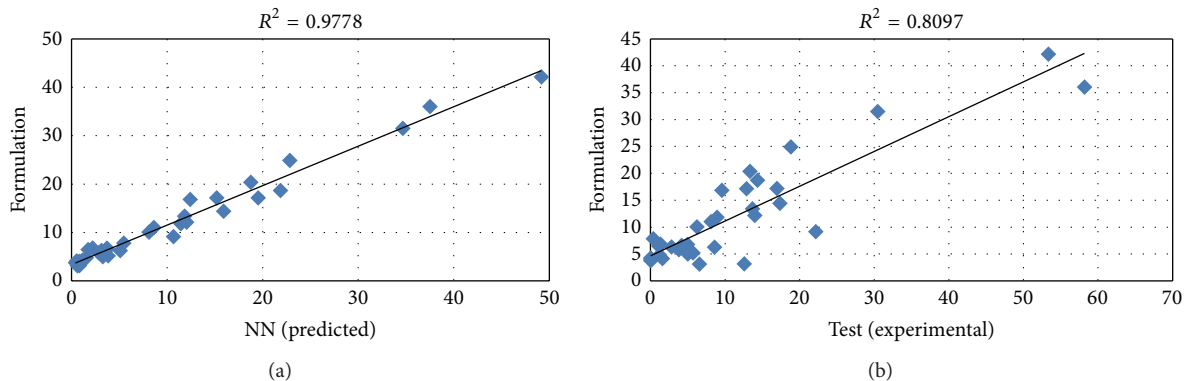


FIGURE 7: Correlation of (a) NN and formulation and (b) NN and testing set.

under 10 N load at a sliding speed of 0.033 m/s was determined as 3.093 mm^3 . In the same experimental conditions, to decrease the wear volume loss to $1.992 \pm 0.165 \text{ mm}^3$, the 1 wt.% of zeolite with the size of $45 \mu\text{m}$ was added according to the NN model theoretically. As a result, the wear volume loss formulation of UHMWPE was evaluated and the two volume loss values were calculated by using this formulation. Additionally, the correlation coefficients of the proposed equations were also evaluated. The correlations of NN, formulation, and experimental data were given in Figure 7.

It is clear that R^2 values of formulation and NN model and formulation and experimental results are 0.9778 and 0.8097, respectively. This means that the proposed NN model (formulation) can predict the volume loss of the composites with 80.97% accuracy.

5. Conclusion

This study proposes an approach of artificial neural network modeling for the wear volume loss in the prediction of UHMWPE composites with different fibers and particles and in various operating parameters. The proposed NN model shows good agreement with the experimental results. Therefore, the explicit mathematical function was derived from ANN models. In the accuracy of the well-trained ANN model, all R^2 values for training, testing, and formulation are bigger than 0.80 and the predicted model is of a high reliability rate. The mean absolute error for predicted values does not exceed 4.1%. The sensitivity analysis of the developed NN model demonstrated that sliding speed and applied load are the significant variables in affecting the volume loss. Hence, it was concluded that ANN is a successful and advantageous analytical tool for determining the properties of UHMWPE composites with considerable saving in cost and time.

Appendix

See Table 2.

Conflict of Interests

The authors declare that there is no conflict of interests regarding the publication of this paper.

References

- [1] Z.-M. Huang, Y.-Z. Zhang, M. Kotaki, and S. Ramakrishna, "A review on polymer nanofibers by electrospinning and their applications in nanocomposites," *Composites Science and Technology*, vol. 63, no. 15, pp. 2223–2253, 2003.
- [2] Y. Kim, H. Lee, S. Park, and X. Zhang, "Stress relaxation test of molding compound for MEMS packaging," in *Proceedings of the 13th InterSociety Conference on Thermal and Thermomechanical Phenomena in Electronic Systems (ITherm '12)*, pp. 290–296, IEEE, San Diego, Calif, USA, June 2012.
- [3] A. S. Luyt, J. A. Molefi, and H. Krump, "Thermal, mechanical and electrical properties of copper powder filled low-density and linear low-density polyethylene composites," *Polymer Degradation and Stability*, vol. 91, no. 7, pp. 1629–1636, 2006.
- [4] L. Woo, M. T. K. Ling, S. Y. Ding, and S. P. Westphal, "Effect of ionizing radiation on the thermal oxidative stability of medical polymers," *Thermochimica Acta*, vol. 324, no. 1-2, pp. 179–185, 1998.
- [5] S. Devasahayam and P. Yarlagadda, "Mechanics of polypropylene-seed-coat-fibres composites and polypropylene-wood fibres composites—a comparative study," *Procedia Engineering*, vol. 97, pp. 1915–1928, 2014.
- [6] B. S. Shim, J. Starkovich, and N. Kotov, "Multilayer composites from vapor-grown carbon nano-fibers," *Composites Science and Technology*, vol. 66, no. 9, pp. 1171–1178, 2006.
- [7] W. S. Lee and J. Yu, "Comparative study of thermally conductive fillers in underfill for the electronic components," *Diamond and Related Materials*, vol. 14, no. 10, pp. 1647–1653, 2005.
- [8] V. Choudhary and A. Gupta, "Polymer/carbon nanotube nanocomposites," in *Carbon Nanotubes—Polymer Nanocomposites*, chapter 4, pp. 65–90, InTech, Rijeka, Croatia, 2011.
- [9] W. Zhao, H. Wang, H. Tang, and G. Chen, "Facile preparation of epoxy-based composite with oriented graphite nanosheets," *Polymer*, vol. 47, no. 26, pp. 8401–8405, 2006.
- [10] S. Kemaloglu, G. Ozkoc, and A. Aytac, "Properties of thermally conductive micro and nano size boron nitride reinforced silicon

- rubber composites," *Thermochimica Acta*, vol. 499, no. 1-2, pp. 40-47, 2010.
- [11] X.-L. Xie, Y.-W. Mai, and X.-P. Zhou, "Dispersion and alignment of carbon nanotubes in polymer matrix: a review," *Materials Science and Engineering R: Reports*, vol. 49, no. 4, pp. 89-112, 2005.
- [12] S. M. Kurtz, *UHMWPE Biomaterials Handbook: Ultra High Molecular Weight Polyethylene in Total Joint Replacement and Medical Devices*, Elsevier Science, 2009.
- [13] P. S. M. Barbour, M. H. Stone, and J. Fisher, "A study of the wear resistance of three types of clinically applied UHMWPE for total replacement hip prostheses," *Biomaterials*, vol. 20, no. 22, pp. 2101-2106, 1999.
- [14] X. Dangsheng, "Friction and wear properties of UHMWPE composites reinforced with carbon fiber," *Materials Letters*, vol. 59, no. 2-3, pp. 175-179, 2005.
- [15] K. Plumlee and C. J. Schwartz, "Improved wear resistance of orthopaedic UHMWPE by reinforcement with zirconium particles," *Wear*, vol. 267, no. 5-8, pp. 710-717, 2009.
- [16] G. Guofang, Y. Huayong, and F. Xin, "Tribological properties of kaolin filled UHMWPE composites in unlubricated sliding," *Wear*, vol. 256, no. 1-2, pp. 88-94, 2004.
- [17] D. Xiong, J. Lin, D. Foan, and Z. Jin, "Wear of nano-TiO₂/UHMWPE composites radiated by gamma ray under physiological saline water lubrication," *Journal of Materials Science: Materials in Medicine*, vol. 18, no. 11, pp. 2131-2135, 2007.
- [18] Y.-S. Zoo, J.-W. An, D.-P. Lim, and D.-S. Lim, "Effect of carbon nanotube addition on tribological behavior of UHMWPE," *Tribology Letters*, vol. 16, no. 4, pp. 305-310, 2004.
- [19] H. K. Durmuş, E. Özkaya, and C. Meriç, "The use of neural networks for the prediction of wear loss and surface roughness of AA 6351 aluminium alloy," *Materials & Design*, vol. 27, no. 2, pp. 156-159, 2006.
- [20] H. Çetinel, H. Öztürk, E. Çelik, and B. Karlik, "Artificial neural network-based prediction technique for wear loss quantities in Mo coatings," *Wear*, vol. 261, no. 10, pp. 1064-1068, 2006.
- [21] Z. Zhang, K. Friedrich, and K. Velten, "Prediction on tribological properties of short fibre composites using artificial neural networks," *Wear*, vol. 252, no. 7-8, pp. 668-675, 2002.
- [22] A. P. Vassilopoulos, E. F. Georgopoulos, and V. Dionysopoulos, "Artificial neural networks in spectrum fatigue life prediction of composite materials," *International Journal of Fatigue*, vol. 29, no. 1, pp. 20-29, 2007.
- [23] H. I. Kurt and M. Oduncuoglu, "Formulation of the effect of different alloying elements on the tensile strength of the *in situ* Al-Mg₂Si composites," *Metals*, vol. 5, no. 1, pp. 371-382, 2015.
- [24] H. I. Kurt and M. Oduncuoglu, "Effects of temperature, time, magnesium, and copper on the wettability of Al/TiC system," *Mathematical Problems in Engineering*. In press.
- [25] K. Venkata Rao, B. S. N. Murthy, and N. Mohan Rao, "Prediction of cutting tool wear, surface roughness and vibration of work piece in boring of AISI 316 steel with artificial neural network," *Measurement*, vol. 51, no. 1, pp. 63-70, 2014.
- [26] L. A. Gyurova and K. Friedrich, "Artificial neural networks for predicting sliding friction and wear properties of polyphenylene sulfide composites," *Tribology International*, vol. 44, no. 5, pp. 603-609, 2011.
- [27] X. Li, Y. Zhu, and G. Xiao, "Application of artificial neural networks to predict sliding wear resistance of Ni-TiN nanocomposite coatings deposited by pulse electrodeposition," *Ceramics International*, vol. 40, no. 8, part A, pp. 11767-11772, 2014.
- [28] S. S. Haykin, *Neural Networks: A Comprehensive Foundation*, Prentice Hall, 1999.
- [29] M. Yurdakul and H. Akdas, "Modeling uniaxial compressive strength of building stones using non-destructive test results as neural networks input parameters," *Construction and Building Materials*, vol. 47, pp. 1010-1019, 2013.
- [30] R. Hecht-Nielsen, *Neurocomputing*, Addison-Wesley, 1990.
- [31] D. E. Rumelhart, G. E. Hinton, and R. J. Williams, "Learning internal representations by error propagation," in *Parallel Distributed Processing: Explorations in the Microstructure of Cognition*, E. R. David, L. M. James, and C. P. R. Group, Eds., vol. 1, pp. 318-362, MIT Press, 1986.
- [32] A. Cevik, M. A. Kutuk, A. Erklig, and I. H. Guzelbey, "Neural network modeling of arc spot welding," *Journal of Materials Processing Technology*, vol. 202, no. 1-3, pp. 137-144, 2008.
- [33] R. Roiger and M. Geatz, *Data Mining: A Tutorial-Based Primer*, Addison-Wesley, 2003.
- [34] D. T. Larose, "Neural Networks," in *Discovering Knowledge in Data*, pp. 128-146, John Wiley & Sons, 2005.
- [35] B. P. Chang, H. M. Akil, M. G. Affendy, A. Khan, and R. B. M. Nasir, "Comparative study of wear performance of particulate and fiber-reinforced nano-ZnO/ultra-high molecular weight polyethylene hybrid composites using response surface methodology," *Materials & Design*, vol. 63, pp. 805-819, 2014.
- [36] A. M. Hassan, A. Alrashdan, M. T. Hayajneh, and A. T. Mayyas, "Prediction of density, porosity and hardness in aluminum-copper-based composite materials using artificial neural network," *Journal of Materials Processing Technology*, vol. 209, no. 2, pp. 894-899, 2009.
- [37] Y. Sun, W. D. Zeng, X. M. Zhang, Y. Q. Zhao, X. Ma, and Y. F. Han, "Prediction of tensile property of hydrogenated Ti600 titanium alloy using artificial neural network," *Journal of Materials Engineering and Performance*, vol. 20, no. 3, pp. 335-340, 2011.
- [38] M. Sudheer, R. Prabhu, K. Raju, and T. Bhat, "Effect of filler content on the performance of epoxy/PTW composites," *Advances in Materials Science and Engineering*, vol. 2014, Article ID 970468, 11 pages, 2014.
- [39] A. Gupta, A. Kumar, A. Patnaik, and S. Biswas, "Effect of different parameters on mechanical and erosion wear behavior of bamboo fiber reinforced epoxy composites," *International Journal of Polymer Science*, vol. 2011, Article ID 592906, 10 pages, 2011.
- [40] A. Dolata-Grosz and J. Wiczorek, "Tribological properties of hybrid composites containing two carbide phases," *Archives of Materials Science and Engineering*, vol. 28, no. 3, pp. 149-155, 2007.
- [41] K. V. Mahendra and K. Radhakrishna, "Characterization of stir cast Al-Cu-(fly ash + SiC) hybrid metal matrix composites," *Journal of Composite Materials*, vol. 44, no. 8, pp. 989-1005, 2010.
- [42] S. Basavarajappa, G. Chandramohan, K. Mukund, M. Ashwin, and M. Prabu, "Dry sliding wear behavior of Al 2219/SiCp-Gr hybrid metal matrix composites," *Journal of Materials Engineering and Performance*, vol. 15, no. 6, pp. 668-674, 2006.
- [43] A. Cevik and I. H. Guzelbey, "Neural network modeling of strength enhancement for CFRP confined concrete cylinders," *Building and Environment*, vol. 43, no. 5, pp. 751-763, 2008.
- [44] B.-P. Chang, H. M. Akil, and R. B. M. Nasir, "Comparative study of micro- and nano-ZnO reinforced UHMWPE composites under dry sliding wear," *Wear*, vol. 297, no. 1-2, pp. 1120-1127, 2013.

- [45] B. P. Chang, H. M. Akil, and R. M. Nasir, "Mechanical and tribological properties of Zeolite-reinforced UHMWPE composite for implant application," *Procedia Engineering*, vol. 68, pp. 88–94, 2013.
- [46] Z. Tai, Y. Chen, Y. An, X. Yan, and Q. Xue, "Tribological behavior of UHMWPE reinforced with graphene oxide nanosheets," *Tribology Letters*, vol. 46, no. 1, pp. 55–63, 2012.
- [47] J. Tong, Y. Ma, and M. Jiang, "Effects of the wollastonite fiber modification on the sliding wear behavior of the UHMWPE composites," *Wear*, vol. 255, no. 1–6, pp. 734–741, 2003.

Research Article

High-Density Polyethylene and Heat-Treated Bamboo Fiber Composites: Nonisothermal Crystallization Properties

Yanjun Li,^{1,2} Lanxing Du,¹ Zhen Zhang,³ and Qinglin Wu³

¹School of Engineering, Zhejiang Agriculture and Forestry University, Lin'an 311300, China

²College of Materials Science and Engineering, Nanjing Forestry University, Long Pan Road, Nanjing 210037, China

³School of Renewable Natural Resources, Louisiana State University Agricultural Center, Baton Rouge, LA 70803, USA

Correspondence should be addressed to Qinglin Wu; qw@agcenter.lsu.edu

Received 19 December 2014; Accepted 23 February 2015

Academic Editor: Jian-Guo Dai

Copyright © 2015 Yanjun Li et al. This is an open access article distributed under the Creative Commons Attribution License, which permits unrestricted use, distribution, and reproduction in any medium, provided the original work is properly cited.

The effect of heat-treated bamboo fibers (BFs) on nonisothermal crystallization of high-density polyethylene (HDPE) was investigated using differential scanning calorimetry under nitrogen. The Avrami-Jeziorny model was used to fit the measured crystallization data of the HDPE/BF composites and to obtain the model parameters for the crystallization process. The heat flow curves of neat HDPE and HDPE/heat-treated BF composites showed similar trends. Their crystallization mostly occurred within a temperature range between 379 K and 399 K, where HDPE turned from the liquid phase into the crystalline phase. Values of the Avrami exponent (n) were in the range of 2.8~3.38. Lamellae of neat HDPE and their composites grew in a three-dimensional manner, which increased with increased heat-treatment temperature and could be attributed to the improved ability of heterogeneous nucleation and crystallization completeness. The values of the modified kinetic rate constant (K_f) first increased and then decreased with increased cooling rate because the supercooling was improved by the increased number of nucleating sites. Heat-treated BF and/or a coupling agent could act as a nucleator for the crystallization of HDPE.

1. Introduction

Heat treatment of bamboo material under oil, steam, or oxygen-deficient conditions presents a physical modification technique for altering properties of bamboo fibers (BFs) such as strength and durability. Heat-treated BFs have been shown to have somewhat reduced mechanical properties, unchanged shrinkage, and a lowered equilibrium moisture content [1, 2]. As heat-treatment temperature increased, the relative contents of hemicellulose and cellulose decreased and lignin content increased in the heat-treated bamboo material [2, 3]. Heat treatment was also shown to lead to better color stability compared with untreated bamboo [4, 5]. With respect to composites, high-density polyethylene (HDPE)/heat-treated BF composites showed lower water absorption rates and similar mechanical properties compared with those from untreated BF/HDPE composites [3]. In a more recent study related to the thermal decomposition behaviors of HDPE/heat-treated BF composites, Li et al. [6]

showed that the values of activation energy were between 225 and 236 kJ/mol and decreased with increasing heat-treatment temperature.

The crystallization properties of polymers have an enormous influence on the performance and processing properties of polymer-based composites [7–9]. The crystallization process includes two stages: nucleation and crystal growth. The nucleation stage produces nucleating sites, in which crystal grain is generated. The crystallization process includes homogeneous nucleation and heterogeneous nucleation. Homogeneous nucleation refers to the spontaneous crystallization of neat resins with changing temperatures. With respect to heterogeneous nucleation, additives mixed in the neat HDPE can help form nucleating sites, leading to a fast crystallization rate of HDPE and higher crystallization temperature [10]. Crystallization tests can be done in both isothermal and nonisothermal conditions [11, 12].

Recently, more attention has been paid to the crystallization properties of polymer in wood/natural fiber composites.

Some studies assert that fillers such as wood and/or other natural fibers play a role as a nucleator and therefore enhance crystallization rate and relative crystallinity, especially for polypropylene (PP) composites. In addition, surface properties of the fibers (e.g., roughness) and modification methods (e.g., using coupling agents to improve compatibility) can affect crystallization properties [13–15]. Mi et al. [16] showed the β -form crystallinity differences in the melting and crystallization processes of neat PP matrix and PP/BF composites from the heat flow curves. Another study contended that this β -form crystallinity was mainly determined by various inorganic fillers, which in turn influenced the properties of those composites, especially the thermal properties [17, 18]. For PP/BF composites, the increasing fiber loading decreased the melting enthalpy, crystallization enthalpy, and crystallinity; and the crystallization temperature increased with the addition of BFs [19]. Under a certain cooling rate, peak temperature had a relationship with the loading level of fillers, and the fillers presented a multinucleating effect [20, 21]. Phuong and Gilbert [22] investigated the crystallization kinetics of recycled PP/bamboo composites, and the results showed that the peak and onset temperatures of crystallization moved to a lower temperature with increasing cooling rate. This was because of the slower cooling rate that provided sufficient time to stimulate the crystallization at a high temperature [22]. Nonisothermal crystallization of neat high-density polyethylene (HDPE), wood flour (WF)/HDPE composite (WPC), virgin Kevlar fiber- (KF-) reinforced WPC (KFWPC), and grafted Kevlar fiber- (GKF-) reinforced WPC (GKFWPC) was investigated by means of differential scanning calorimetry and wide-angle X-ray diffraction [23]. The values of crystallization peak temperature, half-time of crystallization ($t_{1/2}$), and other kinetic parameters showed that the crystallizability followed the following order: FKFWPC > GKFWPC > HDPE > WPC. The X-ray diffraction data indicated that the crystalline thickness perpendicular to the reflection plane increased with the addition of KF. The results demonstrated that KF and GKF can act as nucleating agents and increase the crystallization rate of HDPE. Compared with GKF, KF is a more effective nucleating agent for HDPE. Though some of the aforementioned studies investigated the crystallization behavior of bamboo-based polymer composites, none of the published work has dealt with heat-treated bamboo material and the polymer crystallization process, according to our knowledge.

The objectives of this study were to investigate the effects of heat-treated BFs on the nonisothermal crystallization of HDPE and to acquire information about the characteristic parameters of HDPE's crystallization, which could help control the process of crystallization and analyze the properties of the resultant composites during processing.

2. Experimental

2.1. Raw Material and Preparation. Moso bamboo (*Phyllostachys edulis*) was used for this study. Green bamboo sections with diameters varying from 70 to 100 mm were

collected and cross cut and then sawn into strips. All strips were dried at $100 \pm 2^\circ\text{C}$ for 48 h to reduce their moisture content to about 6%. The strips were then randomly divided into three equal weight groups. One group was used as the control and the two other groups were subjected to heat treatment at 150 and 180°C for 2 h. All three groups were then hammer-milled, and the crushed material was screened to pass a 40-mesh screen.

High-density polyethylene (HDPE AD60-007 with MFR = 0.7 g/10 min at $190^\circ\text{C}/2.16\text{ kg}$, density = 0.96 g/cm^3) was provided by ExxonMobile Chemical Co. (Houston, TX, USA). MAPE (Epolene G2608 with MFR = 6–10 g/10 min at $190^\circ\text{C}/2.16\text{ kg}$, MF = 65,000 g/mol, and acid number = 8 mgKOH/g) from Eastman Chemical Co. (Kingsport, TN, USA) was utilized to increase compatibility between the fillers and the plastic matrix.

2.2. Composite Sample Preparation. Melt compounding of HDPE with other components (40 wt% BF, 58 wt% HDPE, and 2 wt% MAPE) was performed using an intermesh, counterrotating Brabender twin-screw extruder (Brabender Instruments Inc., Hackensack, NJ) with a screw speed of 40 rpm. The temperature profile of the barrels was 423–448–448–448–448 K. The extrudates were quenched in a cold water bath and then pelletized into granules, which were oven-dried at 373 K for 12 h and bagged for further testing.

2.3. DSC Test Procedure and Data Analysis. The crystallization behavior of HDPE in the composites was measured using a differential scanning calorimeter (TA DSC Q2000) under nitrogen. Samples of 5–6 mg were taken and placed in aluminum capsules and were heated from 313 K to 433 K at a rate of 10 K/min and then kept for 5 min at 433 K for eliminating their thermal and mechanical history before crystallization. Samples were then cooled at 2.5, 5, 10, 20, and 35 K/min, respectively.

The crystallinity levels (χ_c) of HDPE in the blends were evaluated as

$$\chi_c = \frac{\Delta H_{\text{exp}}}{\Delta H} \times \frac{1}{W_f} \times 100\%, \quad (1)$$

where ΔH_{exp} is the experimental enthalpy of crystallization, ΔH is the assumed enthalpy of crystallization of fully crystalline HDPE, and W_f is the weight fraction of HDPE in the blends. For fully crystalline HDPE, the heat of crystallization is 276 J/g [23]. The half-time of crystallinity ($t_{1/2}$) was determined using the χ_c value. The crystallization time (t) and crystallization temperature (T) are interrelated through the cooling rate φ as

$$t = \frac{T_o - T}{\varphi}. \quad (2)$$

The usual method for analyzing isothermal crystallization kinetics is the Avrami equation, which assumes that the relative crystallinity and crystallization time have the following mathematical relationship:

$$1 - X_t = \exp(-Kt^n), \quad (3)$$

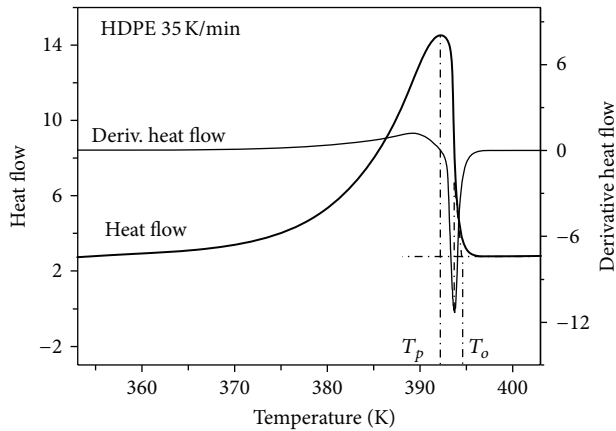


FIGURE 1: Determination of crystallization characteristic parameters of HDPE and its composites by using neat HDPE as an example (cooling rate = 35 K/min).

where n is the Avrami exponent, t is crystallization time, X_t is relative crystallinity, and K is the parameter for the crystallization rate. The parameter n shows the geometry of the growing crystals and nucleation process. Equation (3) can also be written as follows:

$$\log [-\ln (1 - X_t)] = \log K + n \log t. \quad (4)$$

The Jeziorny method is the modified Avrami equation for nonisothermal crystallization. The values of n and t do not have the same physical significance since the temperature is constantly reduced in isothermal crystallization. Therefore, it is assumed that the crystallization temperature is constant. Jeziorny [12] asserted that K should be modified because the cooling rate should be taken into consideration. The final equation is

$$\log K_J = \frac{\log K}{\varphi}, \quad (5)$$

where K_J is the corrected kinetic rate constant.

3. Results and Discussion

3.1. Nonisothermal Crystallization Behavior of Heat-Treated BFs and HDPE Blends. Figure 1 shows a typical plot of heat flow for neat HDPE. As temperature decreased (from the right side to the left side), the heat flow increased and reached a peak value and then gradually decreased. The obvious absorption peak indicated that HDPE turned from a liquid phase into a crystalline phase. Crystallization characteristic parameters were calculated from heat flow and derivative heat flow curves as shown in Figure 1. The extrapolated onset temperature of crystallization, T_o , was obtained by extrapolating the tangent line of the minimal inflection point on the heat flow curve and down to the baseline level of the heat flow axis. The peak temperature, T_p , was the maximum temperature on the heat flow curve.

Figure 2 shows a comparison of heat flow values of HDPE/heat-treated BF composites at different cooling rates,

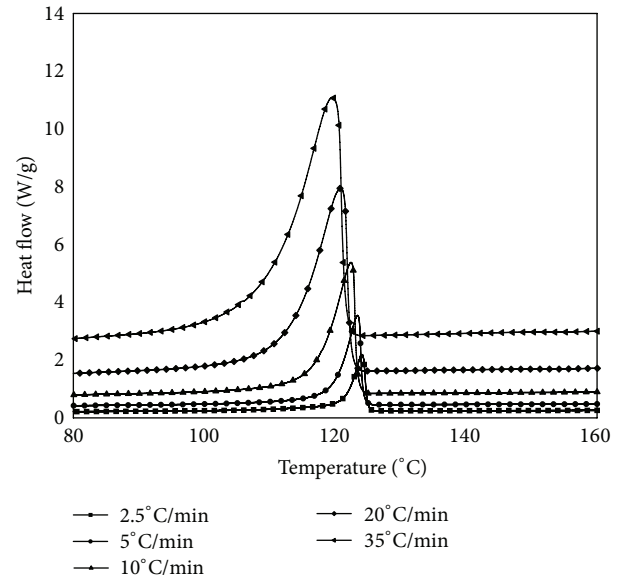


FIGURE 2: A comparison of heat flow curves of HDPE/heat-treated BF composites with heat-treated BFs at different cooling rates.

and Table 1 summarizes the calculated data values. The values of T_o and T_p of both HDPE and the composites reduced gradually, the shoulder of the curves was broadened, and the areas of the curves were enlarged. This is because the slower cooling rate provided better fluidity and diffusivity for the molecules to crystallize at high temperatures [23]. In contrast, faster cooling rates shortened the time for the arrangement of HDPE's molecules and decreased their ability to form the regular structure. Therefore, the faster cooling rate impeded crystallization of HDPE, and more supercooling was needed to reach the same crystallinity at higher cooling rate. The temperature gradient of the samples was presented from the inside outward. Therefore, the crystallization temperature at a lower cooling rate had to be lower in order to attain the same crystallization level. The absorption peak moved to a lower temperature with increasing crystallization time. Furthermore, crystallization properties weakened as the activation energy of HDPE decreased within the low surrounding temperature, which made the peak broaden.

Compared with the nonisothermal crystallization parameters of HDPE, the crystallization temperatures of HDPE/heat-treated BF composites (T_o and T_p) were slightly higher than those of HDPE. This was because of the enhancement effect of the crystallization and relaxation process of HDPE, which was caused by the fact that the addition of BFs and/or a coupling agent could weaken the interfacial interaction. This implies that the BFs could act as a nucleating agent in the HDPE matrix, which provided heterogeneous nucleation sites.

To exclude the influence of the cooling rate, T_o and T_p were obtained using a linear extrapolation to $\varphi = 0$ in the plots of cooling rate against temperature. The crystallinity level corresponding to $\varphi = 0$ was designated as the final crystallinity level. The χ_c values of HDPE and

TABLE 1: Nonisothermal crystallization parameters of HDPE and its composites.

Samples	Φ (K/min)	T_o (K)	T_p (K)	$t_{1/2}$ (min)	ΔH_{exp} (J·g ⁻¹)	X_c (%)	$X_c \varphi = 0$ (%)
HDPE	2.5	397.9	396.7	1.141	122.0	44.2	45.2
	5	397.3	396.7	0.652	126.8	45.9	
	10	396.3	395.0	0.411	121.1	43.9	
	20	395.5	393.7	0.263	122.5	44.4	
	35	394.2	392.2	0.194	116.8	42.3	
HDPE/heat-treated BF (373 K)	2.5	398.1	397.1	1.033	84.4	51.0	49.9
	5	397.4	396.4	0.585	80.6	48.6	
	10	396.5	395.4	0.378	78.1	47.1	
	20	395.5	393.8	0.253	75.2	45.4	
	35	394.6	392.6	0.192	73.6	44.5	
HDPE/heat-treated BF (423 K)	2.5	398.1	397.1	1.007	81.9	49.5	49.4
	5	397.4	396.4	0.596	79.4	48.0	
	10	396.5	395.4	0.373	76.7	46.3	
	20	395.5	393.9	0.253	73.6	44.4	
	35	394.3	391.9	0.207	67.9	41.0	
HDPE/heat-treated BF (453 K)	2.5	398.1	397.2	1.210	83.2	50.0	51.5
	5	397.3	396.4	0.657	78.7	47.5	
	10	396.6	395.4	0.368	74.0	44.7	
	20	395.5	395.3	0.262	70.8	42.7	
	35	394.7	392.7	0.183	70.1	42.3	

their composites (BFs with a heat-treatment temperature of 373 K, 423 K, and 453 K) were 45.2%, 49.9%, 49.4%, and 51.5%, respectively, which displayed an increasing trend as pretreatment temperatures for BFs increased. One possible reason might be that the addition of heat-treated BFs and/or the coupling agent promoted the nucleation of HDPE. A shorter time was needed to acquire higher crystallinity of the blends, leading to better properties. Another cause could be the interaction between the heat-treated BFs and neat HDPE. It should be pointed out that BF itself is a complex polymer made of cellulose, hemicellulose, and lignin. After heat treatment, the orientation of cellulose molecule chains in the amorphous region could be somewhat improved; the noncrystalline region rearranged to form the crystalline region, and then the bridging reaction might take place in the noncrystalline regions.

Relative crystallinity-crystallization time data were obtained based on the crystallinity-temperature data (Figure 3(a)) and using cooling rate data (Figure 3(b)). The crystallization time of 373 K BF-reinforced HDPE composites decreased significantly as the cooling rate increased. The curve between crystallization time and relative crystallinity had an approximate "S" shape, and the size and shape of the "S" were largely affected by the cooling rate. The parameter $t_{1/2}$ is the half-time of relative crystallinity (from 0 to 50%), which is determined by the driving force for the crystal growth. Figure 3(b) shows that $t_{1/2}$ was less than the medium value of the crystallization time. This was because the HDPE crystallized much faster at the beginning of the crystallization process. The $t_{1/2}$ value was reduced as the cooling rate increased. At the same cooling rate, values of $t_{1/2}$ of heat-treated HDPE/heat-treated BF composites were

slightly lower than those of HDPE. This indicates that BF (and/or the coupling agent) accelerated the crystallization rate of HDPE. Thus, the BF could act as a nucleating agent in the HDPE matrix. However, there was no distinguished trend among the $t_{1/2}$ values of various HDPE/heat-treated BF composites.

3.2. Crystallization Kinetics of Heat-Treated BFs and HDPE Blends. Typical plots of $\log[-\ln(1 - X_t)]$ against $\log(t)$ are presented in Figure 4 (composites that contain 373 K heat-treated BF as an example). The left side of the x -axis indicates the early period of crystallization and the right side showed the late period of crystallization. As shown in Figure 4, in the early period of crystallization, the relationship between $\log[-\ln(1 - X_t)]$ and $\log(t)$ displayed positive linear trends. At the beginning of crystallization, HDPE molecules crystallized around nucleating sites with freedom in a sufficient space. Toward the end of crystallization, lamellae began to grow from the nucleating sites and their size increased. The lamellae squeezed and collided, which restrained crystal growth in all directions and thus affected the nucleating pathway. The initial data with a higher linearity were used to calculate the parameters n and K_j . Nonisothermal kinetic parameters of the heat-treated BF-reinforced HDPE composites are listed in Table 2.

The values of n reflected the dimensions of the crystal growth, which were in a range of 0~4. A value of n closer to 4 indicates more complete crystallization. Table 2 shows that the n values of neat HDPE and its composites decreased with increased cooling rates, and thus the degree of crystallization of HDPE lamellae reduced. The values of n were not integers

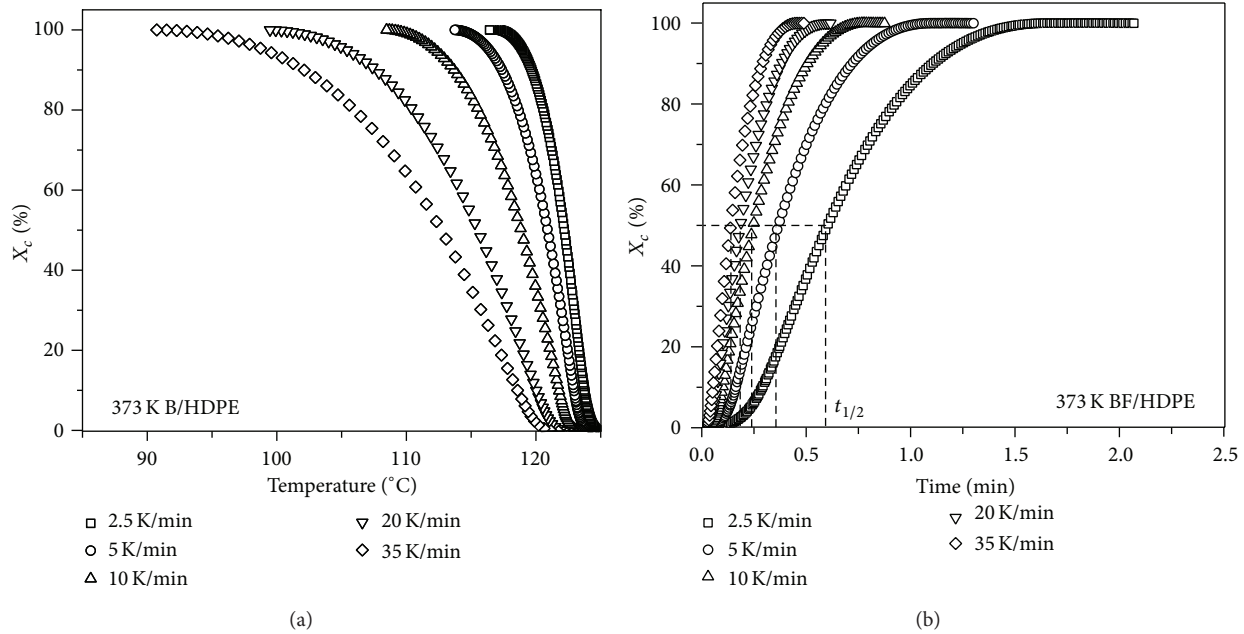


FIGURE 3: (a) Curves of relative crystallinity for HDPE/heat-treated BF composites (BF with a heat-treatment temperature of 373 K) versus temperature. (b) Curves of relative crystallinity for HDPE/heat-treated BF composites (BF with a heat-treatment temperature of 373 K) versus time.

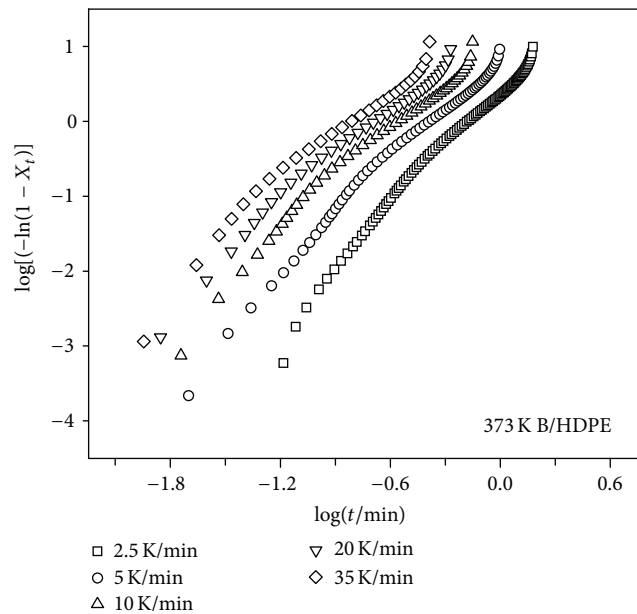


FIGURE 4: Plots of $\log[-\ln(1 - X_c)]$ versus $\log(t)$ for HDPE/heat-treated BF composites (BF with a heat-treatment temperature of 373 K).

as a result of various nucleating pathways brought about by heterogeneous nucleation. The average value of n for neat HDPE was 2.87, while the average values of BF-HDPE composites that contain 373 K, 423 K, and 453 K heat-treated BF were 2.96, 2.87, and 2.88, respectively. This demonstrated that crystals in both neat HDPE and the composites primarily

grew in a three-dimensional manner, and the BFs and/or coupling agent enhanced heterogeneous nucleation and caused more complete crystallization, which could be attributed to the nucleating effect of BFs and the compatibilizing effect exerted by the coupling agent. However, heat treatment slightly reduced the values of n , which were close to those of the neat HDPE. Perhaps the heat treatment reduced the surface polarity of bamboo, though further investigation is needed.

K_f reflected the nonisothermal parameters of the crystallization rate with a modified cooling rate. With increasing cooling rate, the values of K_f first increased and then decreased. This is because supercooling was improved by the increased cooling rate to enhance the nucleating sites. The shortened distances between different molecules facilitated the completion of crystallization and boosted crystallization rate. The K_f values of HDPE/heat-treated BF composites were slightly higher than those of neat HDPE.

4. Conclusions

- (1) Differential scanning calorimetry under nitrogen was used to investigate the crystallization processes of neat HDPE and the resultant BF-HDPE composites. The heat flow curves of neat HDPE and heat-treated BF-HDPE composites had similar trends. Crystallization of the materials mostly occurred within a temperature range between 379 K and 399 K. With increased cooling rate, the peak temperatures of these composites moved to lower temperature values and the peaks became broadened due to the

TABLE 2: Nonisothermal kinetic parameters at different relative crystallization of HDPE and its composites based on the Jeziorny model.

Samples	$\varphi/K/\text{min}$	N	$\log K$	R^2	$\log K_j$	K_j	R^2
HDPE	2.5	2.96	0.47	2.95	0.19	1.54	0.9999
	5	3.1	1.42	26.23	0.28	1.92	0.9995
	10	2.88	1.82	65.68	0.18	1.52	0.9999
	20	2.74	2.31	202.19	0.12	1.30	0.9988
	35	2.65	2.65	446.34	0.08	1.19	0.9982
373 K BF/HDPE	2.5	3.05	0.67	4.65	0.27	1.85	0.9990
	5	2.96	1.35	22.5	0.27	1.86	0.9992
	10	2.89	1.94	87.54	0.19	1.56	0.9996
	20	2.93	2.44	275.99	0.12	1.32	0.9993
	35	2.98	2.9	795.39	0.08	1.21	0.9945
423 K BF/HDPE	2.5	3.3	0.86	7.33	0.35	2.22	0.9996
	5	2.8	1.16	14.53	0.23	1.71	0.9987
	10	2.68	1.75	56.02	0.17	1.50	0.9973
	20	2.68	2.11	128.54	0.11	1.27	0.9994
	35	2.89	2.63	422.02	0.08	1.19	0.9995
453 K BF/HDPE	2.5	2.56	0.4	2.49	0.16	1.44	0.9991
	5	2.33	0.74	5.49	0.15	1.41	0.9964
	10	3.38	2.44	273.11	0.24	1.75	0.9993
	20	3.16	2.66	455.38	0.13	1.36	0.9990
	35	2.96	2.96	911.61	0.08	1.21	0.9997

increased cooling rate that improved supercooling and decreased crystallization temperature.

- (2) Values of the Jeziorny model parameter n were in the range of 2.8~3.38. Crystal lamellae of neat HDPE and the resulting composites grew in a three-dimensional manner, which increased with increasing BF heat-treatment temperature. This indicates that the addition of BFs and/or a coupling agent was helpful for improving the ability of heterogeneous nucleation and crystallization completeness. The values of the Jeziorny model parameter K_j increased and then decreased when the cooling rate increased because supercooling was improved by the increased cooling rate.
- (3) Heat-treated BFs and/or coupling agent could act as a nucleator for the nucleation of HDPE polymer in the composites.

Conflict of Interests

The authors declare that there is no conflict of interests regarding the publication of this paper.

Acknowledgments

The authors are grateful for the support of the Zhejiang Agriculture and Forestry University Forestry Engineering Discipline Open Fund, the Key Project of the Chinese Ministry of Education (no. 201090) and the Project of the

Science Technology Department of Zhejiang Province (nos. 2010C12021 and 2010R50023-05).

References

- [1] O. Shinji, T. Hitoshi, and N. Ryusuke, "Mechanical properties of heat-treated natural fibers," *Journal of the Society of Materials Science, Japan*, vol. 51, no. 10, pp. 1164–1168, 2002.
- [2] Y. J. Bao, *Research on the main chemical components, physical and mechanical properties of bamboo after thermal treatment [M.S. thesis]*, Northeast Forestry University, Harbin, China, 2009.
- [3] F. Q. Zhou, *Study on preparation and properties of heat-treated bamboo/polyethylene composites [M.S. thesis]*, Fujian Normal University, Fuzhou, China, 2009.
- [4] Y. M. Zhang, Y. L. Yu, and W. J. Yu, "Discoloration of heat-treated bamboo material," *China Wood Industry*, vol. 23, no. 5, pp. 5–7, 2009.
- [5] L. Qin, *Effect of thermo-treatment on physical, mechanical properties and durability of reconstituted bamboo lumber [Ph.D. dissertation]*, Chinese Academy of Forestry, 2010.
- [6] Y. J. Li, L. X. Du, C. Kai, R. Z. Huang, and Q. Wu, "Bamboo and high density polyethylene composite with heat-treated bamboo fiber: thermal decomposition properties," *BioResources*, vol. 8, no. 1, pp. 900–912, 2013.
- [7] R. Kumari, H. Ito, M. Takatani, M. Uchiyama, and T. Okamoto, "Fundamental studies on wood/cellulose-plastic composites: effects of composition and cellulose dimension on the properties of cellulose/PP composite," *Journal of Wood Science*, vol. 53, no. 6, pp. 470–480, 2007.
- [8] A. Nourbakhsh and A. Ashori, "Fundamental studies on wood-plastic composites: effects of fiber concentration and mixing

- temperature on the mechanical properties of poplar/PP composite," *Polymer Composites*, vol. 29, no. 5, pp. 569–573, 2008.
- [9] M. Chaharmahali, M. Tajvidi, and S. K. Najafi, "Mechanical properties of wood plastic composite panels made from waste fiberboard and particleboard," *Polymer Composites*, vol. 29, no. 6, pp. 606–610, 2008.
- [10] P. Wang, J. Liu, W. Yu, and C. X. Zhou, "Isothermal crystallization kinetics of highly filled wood plastic composites: effect of wood particles content and compatibilizer," *Journal of Macromolecular Science, Part B: Physics*, vol. 50, no. 12, pp. 2271–2289, 2011.
- [11] M. Avrami, "Kinetics of phase change. I: general theory," *The Journal of Chemical Physics*, vol. 7, no. 12, pp. 1103–1112, 1939.
- [12] A. Jeziorny, "Parameters characterizing kinetics of nonisothermal crystallization of poly(ethylene-terephthalate) determined by DSC," *Polymer*, vol. 19, no. 10, pp. 1142–1144, 1978.
- [13] S. Borysiak, "Determination of nucleating ability of wood for non-isothermal crystallization of polypropylene," *Journal of Thermal Analysis and Calorimetry*, vol. 88, no. 2, pp. 455–462, 2007.
- [14] H. Bouafif, A. Koubaa, P. Perré, A. Cloutier, and B. Riedl, "Wood particle/high-density polyethylene composites: thermal sensitivity and nucleating ability of wood particles," *Journal of Applied Polymer Science*, vol. 113, no. 1, pp. 593–600, 2009.
- [15] A. P. Mathew, K. Oksman, and M. Sain, "The effect of morphology and chemical characteristics of cellulose reinforcements on the crystallinity of polylactic acid," *Journal of Applied Polymer Science*, vol. 101, no. 1, pp. 300–310, 2006.
- [16] Y. Mi, X. Chen, and Q. Guo, "Bamboo fiber-reinforced polypropylene composites: Crystallization and interfacial morphology," *Journal of Applied Polymer Science*, vol. 64, no. 7, pp. 1267–1273, 1997.
- [17] J. Liu, G. B. Tang, G. J. Qu, H. R. Zhou, and Q. Guo, "Crystallization of rare earth oxide-filled polypropylene," *Journal of Applied Polymer Science*, vol. 47, no. 12, pp. 2111–2116, 1993.
- [18] L. Jingjiang, W. Xiufen, and G. Qipeng, " β -crystalline form of wollastonite-filled polypropylene," *Journal of Applied Polymer Science*, vol. 41, no. 11-12, pp. 2829–2835, 1990.
- [19] S.-Y. Lee, S.-J. Chun, G.-H. Doh, I.-A. Kang, and K.-H. Paik, "Influence of chemical modification and filler loading on fundamental properties of bamboo fibers reinforced polypropylene composites," *Journal of Composite Materials*, vol. 43, no. 15, pp. 1639–1657, 2009.
- [20] T. McNally, P. Pötschke, P. Halley et al., "Polyethylene multi-walled carbon nanotube composites," *Polymer*, vol. 46, no. 19, pp. 8222–8232, 2005.
- [21] H. Xia, Q. Wang, K. Li, and G.-H. Hu, "Preparation of polypropylene/carbon nanotube composite powder with a solid-state mechanochemical pulverization process," *Journal of Applied Polymer Science*, vol. 93, no. 1, pp. 378–386, 2004.
- [22] N. T. Phuong and V. Gilbert, "Non-isothermal crystallization kinetics of short bamboo fiber-reinforced recycled polypropylene composites," *Journal of Reinforced Plastics and Composites*, vol. 29, no. 17, pp. 2576–2591, 2010.
- [23] R. X. Ou, C. Guo, Y. Xie, and Q. Wang, "Non-isothermal crystallization kinetics of Kevlar fiber-reinforced wood flour/HDPE composites," *BioResources*, vol. 6, no. 4, pp. 4547–4565, 2011.

Research Article

Carbon Fiber Composites of Pure Polypropylene and Maleated Polypropylene Blends Obtained from Injection and Compression Moulding

**D. Pérez-Rocha,¹ A. B. Morales-Cepeda,¹ F. Navarro-Pardo,^{1,2}
T. Lozano-Ramírez,¹ and P. G. LaFleur³**

¹*Instituto Tecnológico de Ciudad Madero, División de Estudios de Posgrado e Investigación, Juventino Rosas y Jesús Urueta, Colonia Los Mangos, 89440 Ciudad Madero, TAMPS, Mexico*

²*Instituto Tecnológico de Querétaro, División de Estudios de Posgrado e Investigación, Avenida Tecnológico s/n, Esquina Gral. Mariano Escobedo, Colonia Centro Histórico, 76000 Santiago de Querétaro, QRO, Mexico*

³*École Polytechnique de Montréal, Chemical Engineering Department, P.O. Box 6079, Station Centre-Ville, Montreal, QC, Canada H3C 3A7*

Correspondence should be addressed to A. B. Morales-Cepeda; abmoralesc@itcm.edu.mx

Received 22 March 2015; Accepted 21 May 2015

Academic Editor: Jian-Guo Dai

Copyright © 2015 D. Pérez-Rocha et al. This is an open access article distributed under the Creative Commons Attribution License, which permits unrestricted use, distribution, and reproduction in any medium, provided the original work is properly cited.

A comparative study of the mechanical performance of PP and PP/PP-g-MAH blends reinforced with carbon fibre (CF) obtained by two different moulding techniques is presented. Three filler contents were used for fabricating the composites: 1, 3, and 5 pph (parts per hundred). The crystallisation behaviour of the composites was studied by differential scanning calorimetry. Morphological and structural features of these samples were observed by atomic field microscopy and Fourier-transform infrared spectroscopy, respectively. Mechanical properties of the injection and compression moulded composites were evaluated by means of tensile and impact resistance tests. The fracture surface of the impacted samples was observed by scanning electron microscopy. The processing method had a noticeable effect on the results obtained in these tests. Young's modulus was enhanced up to 147% when adding 5 pph CF to a PP matrix when processed by compression moulding. Addition of PP-g-MAH and CF had a favourable effect on the tensile and impact strength properties in most samples; these composites showed improved performance as the filler content was increased.

1. Introduction

Polypropylene possesses an attractive combination of mechanical properties which can be further improved by the modification of this polymer in order to obtain polymer blends and also by the incorporation of reinforcing fillers [1–3]. Grafting maleic anhydride (MAH) into the PP molecular segments is a common approach for the modification of this polymer. Maleated PP (PP-g-MAH) can be used as a nucleating agent or compatibiliser for blends and composites [2–4]. Polymer blending is a very important technique in the industrial practice and it is mainly used to achieve properties that are more advantageous than those of the individual components [1, 5].

The miscibility between PP and PP-g-MAH has been studied by several authors. Depending on the molecular weight and MAH content in PP, the blending can either cocrystallise or phase separate; this in turn will influence the mechanical properties of PP/PP-g-MAH blends [6, 7]. Furthermore, isothermal crystallisation of PP/PP-g-MAH blends confirmed that there is a correlation between the crystallisation rate and the resulting morphologies [6]. Other authors have also shown that the thermodynamic properties of PP/PP-g-MAH blends have improved the mechanical responses depending on the content of the compatibiliser [8, 9]. Additionally, the mechanical properties of polymers are found to be strongly dependent on the processing technique [7]. They can impart different morphologies and

crystal structures in semicrystalline polymers [5, 10–12]. Moulding techniques are widely used in the plastic industries where injection and compression moulding are typically used for obtaining a variety of products. Another approach for improving the mechanical properties of polymers is by the addition of reinforcement fillers, such as those based on carbon [9–12]. Carbon fibre (CF) reinforced polymer composites have demonstrated having many applications in diverse fields due to their ability to obtain a synergetic effect when combining toughness of the thermoplastic polymer with the stiffness and strength of carbon fibres [12]. Carbon based composites can be found in the high technology sector, which includes aerospace and the automotive industries, including engineering components such as bearings, gears, fan blades, and chassis structures. Due to the importance of these composites and the high number of applications PP moulded parts have in the industry, this paper presents the influence of CF on the tensile and impact strength of PP and PP-g-MAH/PP blends. Furthermore, to our knowledge, this is the first study that shows the effects of these composites when moulded by two different methods, injection and compression moulding, and the behaviour that the PP-g-MAH has when rigid fillers are added to PP.

2. Experimental Methods

2.1. Materials. PP homopolymer XH1760 was supplied by Indelpro (Mexico) with a melt flow index of 3 g/10 min at 230°C/2.16 kg. The material was a commercially stabilized polymer without any further additives, especially without nucleating agents. Polybond 3200 with a melt flow of 115 g/10 min at 230°C/2.16 kg obtained from Chemtura was employed as PP-g-MAH compatibiliser. AGM-99 milled CF produced from PAN with a mean length of 150 microns and a diameter of 8 microns were obtained from Asbury Carbons and used as received.

2.2. Sample Preparation. A twin-screw corotating Brabender Plasti-Corder was used to prepare the PP composites and composite blends (PP/PP-g-MAH) which contained 5 pph PP-g-MAH. The screw speed was 60 rpm and they were compounded at $200 \pm 10^\circ\text{C}$ during 10 min. The polymer and polymer blends were reinforced with CF at three different contents: 1 pph, 3 pph, and 5 pph. These composites were moulded using compression and injection compounding. A Beutelspacher single screw extruder at a screw speed of 50 rpm and temperature profile set from 175°C in the feed section to 190°C at the die was used to prepare the extruded samples. The compounds were fabricated by a Sumitomo injection machine at a moulding temperature of 200°C. The compression moulded samples were prepared at 200°C and 5 tons for 5 min in a Carver press which was followed by cold pressing at 5 tons for 10 min.

2.3. Characterisation Techniques. Fourier-transform infrared (FTIR) spectroscopy was carried out on Perkin Elmer Spectrum 100 spectrometer with an ATR device. The sample films were analysed by atomic field microscopy (AFM) in tapping

mode using an Innova Veeco microscope. Differential scanning calorimetry (DSC) studies were conducted on a Q2000 TA Instrument. All samples weighed approximately 6 mg and were sealed within aluminium pans. The samples were heated from -30 to 200°C and maintained at this temperature for 1 min and then they were cooled down to -30°C to be equilibrated at 1 min; both heating and cooling rates were conducted at $10^\circ\text{C}/\text{min}$. Subsequently, a similar procedure was done at $50^\circ\text{C}/\text{min}$.

Compression moulded samples ($1.5 \times 3 \times 9 \text{ mm}^3$) and injection moulded samples ($3 \times 3 \times 9 \text{ mm}^3$) were subjected to tensile test using an Instron 3365 Universal Materials testing machine at room temperature using a crosshead speed of 5 mm/min and a 5 kN full-scale load cell. All results presented are the average values of three measurements. Izod impact tests were done following ASTM D256 using CEAST Izod pendulum impact tester using a nominal hammer energy of 2 J, and measurements were done in ten samples. Morphology analysis of the impacted areas was made by scanning electron microscopy (SEM) using a JEOL JSM-7600TFE microscope at 2 kV accelerating voltage.

3. Results and Discussion

Extruded composites obtained from the Brabender Plasti-Corder were analysed by calorimetry in order to see the crystallisation properties of these samples. Table 1 shows the resulting melting and the crystallisation temperatures (T_m and T_c , resp.) obtained from the melting and crystallisation curves during the first ($10^\circ\text{C}/\text{min}$) and second ($50^\circ\text{C}/\text{min}$) run. All samples presented a melting temperature $\sim 160^\circ\text{C}$ corresponding to the presence of α -crystals. More evident changes were found in the crystallisation thermograms, where at low cooling rate crystallisation started at higher temperatures, because there was more time to overcome the nucleation energy barriers while at high cooling rate the nuclei became active at lower temperatures. Furthermore, addition of CF led to an increase in the crystallisation temperature as the filler content was increased in those samples containing PP-g-MAH as compatibiliser, indicating its addition favoured the formation of nuclei due to a synergistic effect with the CF. This could be related to the incorporation of PP-g-MAH which is well known for increasing the flow properties, therefore favouring the dispersion of the CF in the PP matrix which allowed the composite blends to crystallise in a smaller time. The crystallisation temperature was increased up to 7°C for the sample obtained from PP/PP-g-MAH and containing 5 pph CF.

According to the fusion enthalpy values included in Table 1, there were noticeable differences between the first and the second run of the samples and also between the composites obtained from the pure PP or the PP/PP-g-MAH blend. Additionally, incorporation of carbon fibres also had an effect in the crystallinity of the samples. The considerable differences between the first and the second value are related to the recrystallisation process during the second run conducted at higher rate. As explained previously, this allowed the crystallisation of the sample at higher temperature and

TABLE 1: Crystallisation properties of the samples.

Sample	Heating and cooling rate					
	T_m , C	10 C/min T_c , C	ΔH_m , J/g	T_m , C	50 C/min T_c , C	ΔH_m , J/g
Pure PP	156.45	116.07	91.21	158.75	107.12	75.97
1 pph CF	161.41	116.12	78.78	160.1	105.47	61.34
3 pph CF	158.62	117.1	74.5	157.84	107.19	60.06
5 pph CF	157.58	118.66	72.77	156.53	109.73	58.94
PP/PP-g-MAH	156.42	113.24	72.99	158.03	103.99	70.83
1 pph CF	157.58	118.66	90.77	156.53	109.73	59.94
3 pph CF	157.09	118.46	83.53	159.43	110.01	62.93
5 pph CF	159.37	119.48	75.38	159.69	111.05	64.12

applying this higher cooling rate after the first melting also restricted the amount of crystals to be nucleated and caused a lower degree of crystallinity. The crystallinity degree can be calculated from the enthalpies of fusion (ΔH_m) using the following equation: $X_c = 100(\Delta H_m/\Delta H_0)$, where ΔH_m is the enthalpy of fusion of the samples obtained from the integration of DSC melting curves and ΔH_0 is the enthalpy of fusion of 100% crystalline polypropylene taken as 209 J/g [9]. Samples containing pure PP had a higher percentage of crystallinity (44%) compared to those obtained from the PP/PP-g-MAH blend (35%). It is well known that PP-g-MAH has lower degree of crystallinity; therefore, this could be an explanation to the crystallinity reduction in the samples obtained from the blends [13]. Interestingly, addition of CF in the blends has been shown to improve this property, especially at lower content of this reinforcing material. On the other hand, addition of CF to the pure PP matrix was not favourable for the crystallinity of the samples.

AFM was employed to investigate the surface morphologies of the samples; Figure 1 contains the images of this analysis. Lee et al. found that iPP and PP-g-MAH exhibited different surface morphologies [14]. The features found by them agree well with the relatively smooth surface of PP-g-MAH displayed in Figure 1(a). Carbonyl groups in MAH have been related to promote heterogeneous nucleation; therefore, small sized spherulites may have been developed in this sample which could not be noticeable in our samples [15]. On the other hand, the rest of the samples clearly showed spherulitic morphology. The PP/PP-g-MAH sample displayed large spherulites with dimensions ranging from 20 to 40 μm ; see Figure 1(b). In addition, as displayed in Figure 1(c), incorporation of CF exhibited smaller spherulites as seen in 1 pph CF/PP; their dimensions are within 10–20 μm , and this can be explained by the impingement of neighbouring spherulites by the CF subsequently truncating these structures in their contact regions and stopping their growth. Interestingly, CF/PP/PP-g-MAH sample (Figure 1(d)) also showed a decrease in spherulite size which is not as evident as the previous sample due to the reduction on the surface roughness attributed to the incorporation of MAH. The few parallel trenches and small defects were originated from the film manufacturing process.

TABLE 2: FTIR peak assignments of iPP.

Peak position, cm^{-1}	Vibrational modes
810	$\gamma(\text{CH}_2)$
841	$\nu(\text{CH}_2)$
900	$\gamma(\text{CH}_3)$
970	$\gamma(\text{CH}_3), \nu(\text{C}-\text{C})$
1000	$\gamma(\text{CH}_3), \nu(\text{C}-\text{CH}_3)$
1170	$\nu(\text{C}-\text{C})$
1380	$\delta(\text{CH}_3)$ asymmetrical
1455	$\delta(\text{CH}_3)$ symmetrical
2840	$\nu(\text{CH}_2)$ symmetrical
2920	$\nu(\text{CH}_2)$ asymmetrical
2950	$\nu(\text{CH}_3)$ asymmetrical

Key: γ : rock, ν : stretch, and δ : bend.

Figure 2 shows the FTIR spectra of PP/PP-g-MAH, 5 pph CF/PP, and 5 pph CF/PP/PP-g-MAH. The peaks located within the 800–1300 cm^{-1} range are characteristic of the stretching and bending vibrations of the hydrocarbon structure of PP. Table 2 details more information regarding this area [2, 16, 17]. The peak located at $\sim 1730 \text{ cm}^{-1}$ is due to the C=O stretch of carboxylic acid of hydrolysed anhydride [18]. Samples containing the compatibiliser show this peak which is associated with the maleic anhydride from the PP-g-MAH.

Figures 3 and 4 show Young's modulus values of the CF composites. In the compression moulded samples, addition of 5 pph CF enhanced this property up to 77% in the composites obtained from pure PP, as seen in Figure 3. On the other hand, when PP-g-MAH was blended into the PP matrix, Young's modulus was increased to a lower degree (12% enhancement at the highest CF content). Addition of 1 pph CF to PP/PP-g-MAH decreased slightly the stiffness of the compression moulded composites, accompanied by an increase in tensile strength, as it will be seen in the next section. Nevertheless, at higher CF content, the modulus was improved, indicating that the content of the filler was high enough to favour this property imparting rigidity to the polymer matrix. In a similar trend as described previously, the reinforcement effect provided by CF was superior in

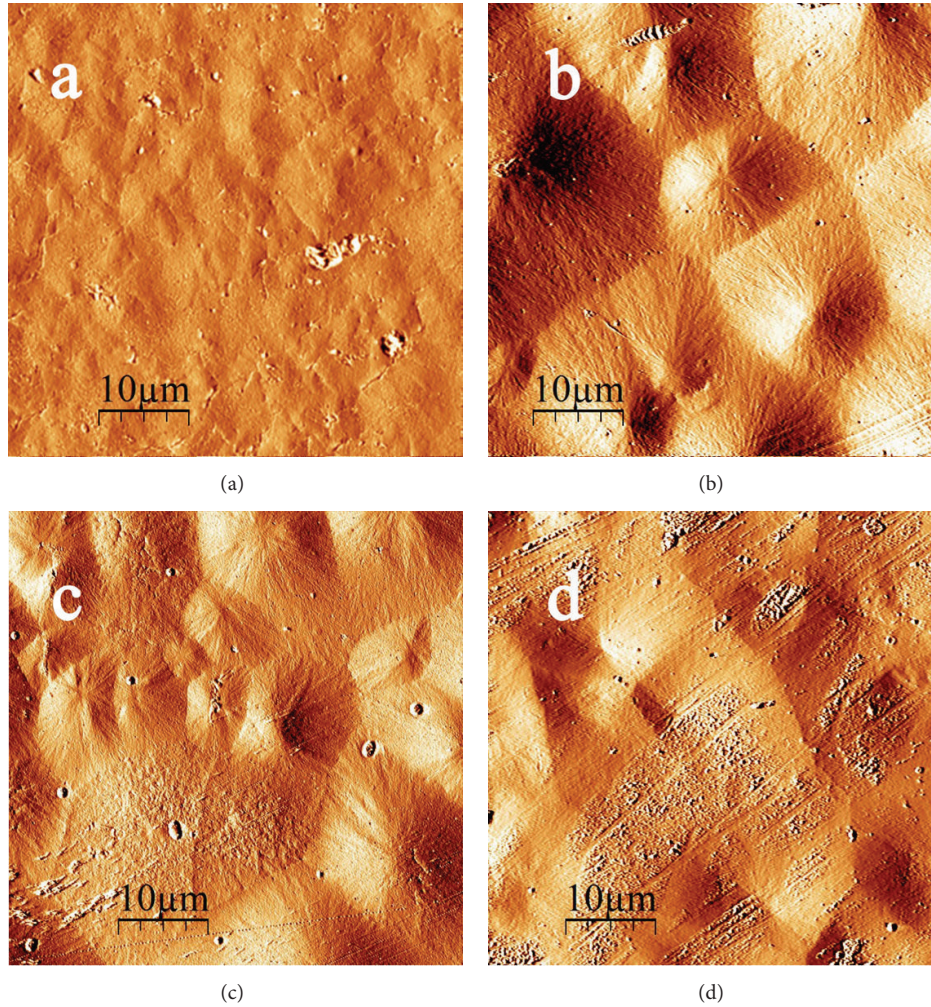


FIGURE 1: AFM images of (a) PP-g-MAH, (b) PP/PP-g-MAH, (c) 1 pph CF/PP, and (d) 1 pph CF PP/PP-g-MAH.

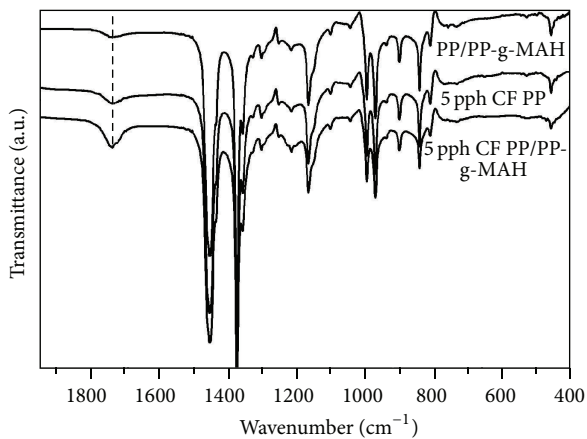


FIGURE 2: FTIR of the extruded samples.

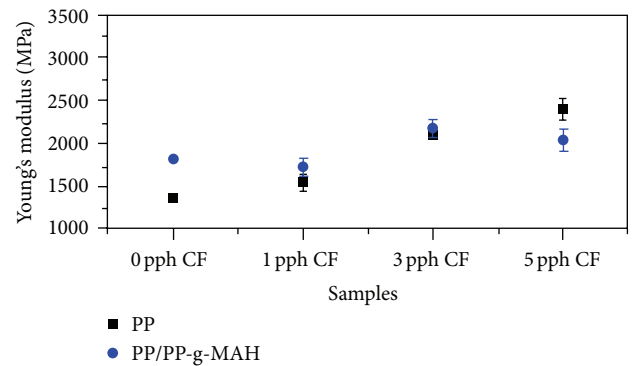


FIGURE 3: Young's modulus of compression moulded samples.

the injection moulded samples containing pure PP. Young's modulus showed an increased response upon incorporation of CF in the PP matrix. This property was enhanced up

to 147% when adding 5 pph CF, as displayed in Figure 4. Regarding the composites obtained from the PP/PP-g-MAH blend, the incorporation of CF is favoured to the stiffness of all the injection moulded samples. Young's modulus was increased up to 35% for the highest CF content.

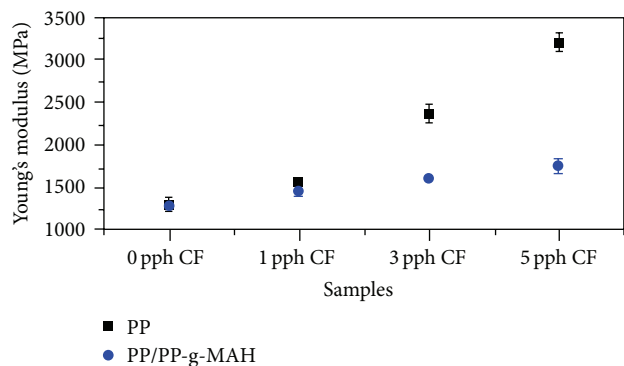


FIGURE 4: Young's modulus of injection moulded samples.

TABLE 3: Tensile strain at break of the compression moulded composites.

Sample	Elongation, %	Std. error
PP	1160.45	53.27
1 pph CF	661.09	87.94
3 pph CF	12.83	1.55
5 pph CF	11.86	2.98
PP/PP-g-MAH	114.88	11.03
1 pph CF	143.28	60.27
3 pph CF	11.64	4.84
5 pph CF	12.06	3.79

The results show the different behaviour that PP-g-MAH can provide when compounded by two different techniques, which is more evident for the injection moulded samples. In the compression moulded samples, the PP/PP-g-MAH blend showed superior modulus at 0 and 1 pph CF content, as compared to pure PP, and this was associated with a brittle behaviour of the samples, resulting in a large reduction of elongation, which is further reduced by a higher content of CF, as displayed in Table 3. A more noticeable difference in the modulus of the samples was found in the injection moulded samples. From Figure 4, it is clearly seen that this property is greatly affected when adding the maleated PP to the PP matrix. Remarkably, this reduction in the modulus is accompanied by a moderate increase of the elongation of the samples and the values are kept even at high loading of the reinforcing filler (see Table 4), indicating the PP-g-MAH had a plasticizer effect in the blend when the composites were obtained by this technique. Järvelä et al. have shown that, at a suitable ratio of PP to PP-g-MAH (similar to that used in this work), the latter had a plasticising function when compounded by injection moulding [19].

Addition of rigid fillers usually restricts the chain mobility of polymer molecules. Since the chains cannot move freely, the strain at break is reduced with increasing CF content, which explains the elongation behaviour found in the compression moulded samples. This behaviour is in agreement with the study conducted by Karsli and Aytac [9]. On the contrary, elongation values were superior in the injection moulded samples. Furthermore, incorporation of the CF

TABLE 4: Tensile strain at break of the injection moulded composites.

Sample	Elongation, %	Std. error
PP	1016.58	54.30
1 pph CF	1195.763333	27.55
3 pph CF	1212.49	30.97
5 pph CF	984.97	2.70
PP/PP-g-MAH	1288.83	64.79
1 pph CF	1236.52	25.17
3 pph CF	871.73	136.53
5 pph CF	994.10	79.73

TABLE 5: Yield strength of the compression moulded composites.

Sample	Strength, MPa	Std. error
PP	38.82	1.21
1 pph CF	38.26	2.14
3 pph CF	44.16	1.13
5 pph CF	43.27	0.80
PP/PP-g-MAH	37.42	0.41
1 pph CF	44.43	1.30
3 pph CF	40.31	0.56
5 pph CF	42.68	1.72

showed only a slight decrease in this property, indicating a synergistic behaviour between the filler and the matrix, and this is further favoured by the addition of PP-g-MAH as shown in Table 4. This synergistic effect will be better seen in the values of impact strength.

From the above mentioned results, it is noticeable that the performance obtained by the samples processed by injection moulding stands out when compared with compression moulded composites. The different behaviour between both processes upon the incorporation of CF can be explained in terms of the orientation of the polymer chains and the filler. Injection moulding allows the polymer chains and CF to orientate parallel to the flow direction, which is not the case for the compression moulding process. The injection moulding samples were tested in the flow direction thus favouring the elongation response; this explains the large difference between the elongation responses of both processes.

Table 5 shows that the tensile strength was slightly improved in the compression moulded composites. The highest enhancement of this property was accomplished by the addition of 1 pph CF in the PP/PP-g-MAH blend, resulting in a 20% increase. Table 6 displays that the injection moulded samples did not show noticeable increases; these results indicate that CF contributed mainly to the stiffness of the composites. However, addition of CF to the PP samples showed a good mechanical performance based on the reinforcing effect seen by improving the modulus and also by maintaining the tensile strain close to that of the pure polymer.

Plastic deformation of the polymer matrix is the main energy absorbing process in impact tests [20]. Since injection

TABLE 6: Yield strength of the injection moulded composites.

Sample	Strength, MPa	Std. error
PP	61.64	1.42
1 pph CF	60.21	1.67
3 pph CF	60.16	1.02
5 pph CF	57.98	0.72
PP/PP-g-MAH	55.59	1.22
1 pph CF	59.46	1.62
3 pph CF	49.34	4.73
5 pph CF	49.73	2.70

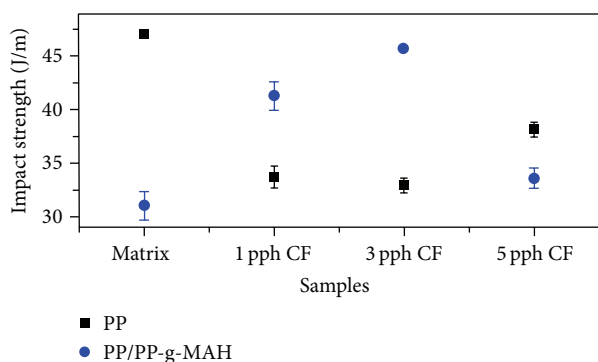


FIGURE 5: Izod impact test values of the injection moulded samples.

moulded samples showed a longer plasticity region, these samples were studied in order to see the effect of the CF and PP-g-MAH on the impact strength of the composites. Figure 5 shows that the composites based on the PP matrix had lower values of impact strength and at higher content of the reinforcing filler this property was improved slightly. The drop of this property with addition of CF could have been by the restriction of chain mobility due to this rigid filler and to the poor interfacial bonding between the filler and the polymer matrix and also due to the creation of stress region concentrations around the carbon fibres that required less energy to initiate the cracking propagation and the resulting microcracks propagated, therefore reducing the resistance to impact [9, 21]. However, when increasing the CF content, some of the energy was absorbed by the filler thus increasing the resistance to impact.

Figure 6 displays a lower value on the impact strength upon addition of PP-g-MAH to the PP matrix which can be explained in the following manner: addition of the compatibiliser caused more boundaries in the PP chains and fracture probably initiated and propagated from these defects when the samples were impacted. This can be related to phase separation of PP/PP-g-MAH blends and it could also explain the lower stiffness of the blend samples when compared to those obtained from only PP. Jiang et al. also found that PP-g-MAH brought about more defects in crystals which might be another reason for the reduced mechanical properties in the blends. Addition of PP-g-MAH was expected to increase the impact strength of the samples, as it has been already found in other studies [22]. This was noticeable at 1 and 3 pph CF

(see Figure 6). At these CF contents, the increased resistance to impact could be attributed to a similar absorbing energy filler behaviour that was explained earlier. This could not be maintained at the higher CF loading and the number of voids around the fibres accounts for the inferior resistance to impact.

SEM micrographs of the polymer and composite fracture surfaces are included in Figure 6. These images show that PP matrix attained poor wetting behaviour on the CF in the absence of compatibiliser. Some of the defective areas attributed to CF/polymer debonding are highlighted in the circled areas of the PP composites. Furthermore, in these composites, the crack propagation resulting from the fillers is shown by arrows, explaining the reduced resistance to impact behaviour achieved in Izod tests. On the other hand, in the PP/PP-g-MAH based composites, the number of debonded CF decreased, especially at lower filler content. Crack propagation of the sample obtained from the blend and reinforced with 5 pph CF is also highlighted by arrows; this feature agrees with the reduced impact strength compared to the rest of the composites.

4. Conclusions

Incorporation of PP-g-MAH has been shown to provide an advantageous effect when used as a compatibiliser in CF composites according to the DSC results which showed higher crystallisation temperatures and also higher degree of crystallinity achieved when compared to those composites based only on a PP matrix. Additionally, composites obtained by compression moulding achieved higher stiffness when the polymer blend was used and with the addition of low content of CF; on the other hand, a reduction in the modulus and a dramatic drop in the elongation of the samples were observed at higher CF content. The mechanical performance in the injection moulded composites differed more noticeably between the samples obtained from pure PP and the PP/PP-g-MAH blend. It was found that addition of CF greatly enhanced the modulus in the composites obtained from the former and the impact strength was reduced compared to the matrix. While the composites obtained from the PP/PP-g-MAH blend had a modest increase in the stiffness by the addition of CF up to the highest loading used in this work and also maintained the values of tensile strain, in these samples, the impact strength was improved with the incorporation of the filler when compared to the unreinforced sample. Impact strength was reduced in the composites obtained from the pure polymer, indicating stress region concentrations around fillers contributed mainly to this response. An absorbing energy filler behaviour was obtained in the samples prepared from the polymer blends as displayed by their enhanced impact strength.

Conflict of Interests

The authors declare that there is no conflict of interests regarding the publication of this paper.

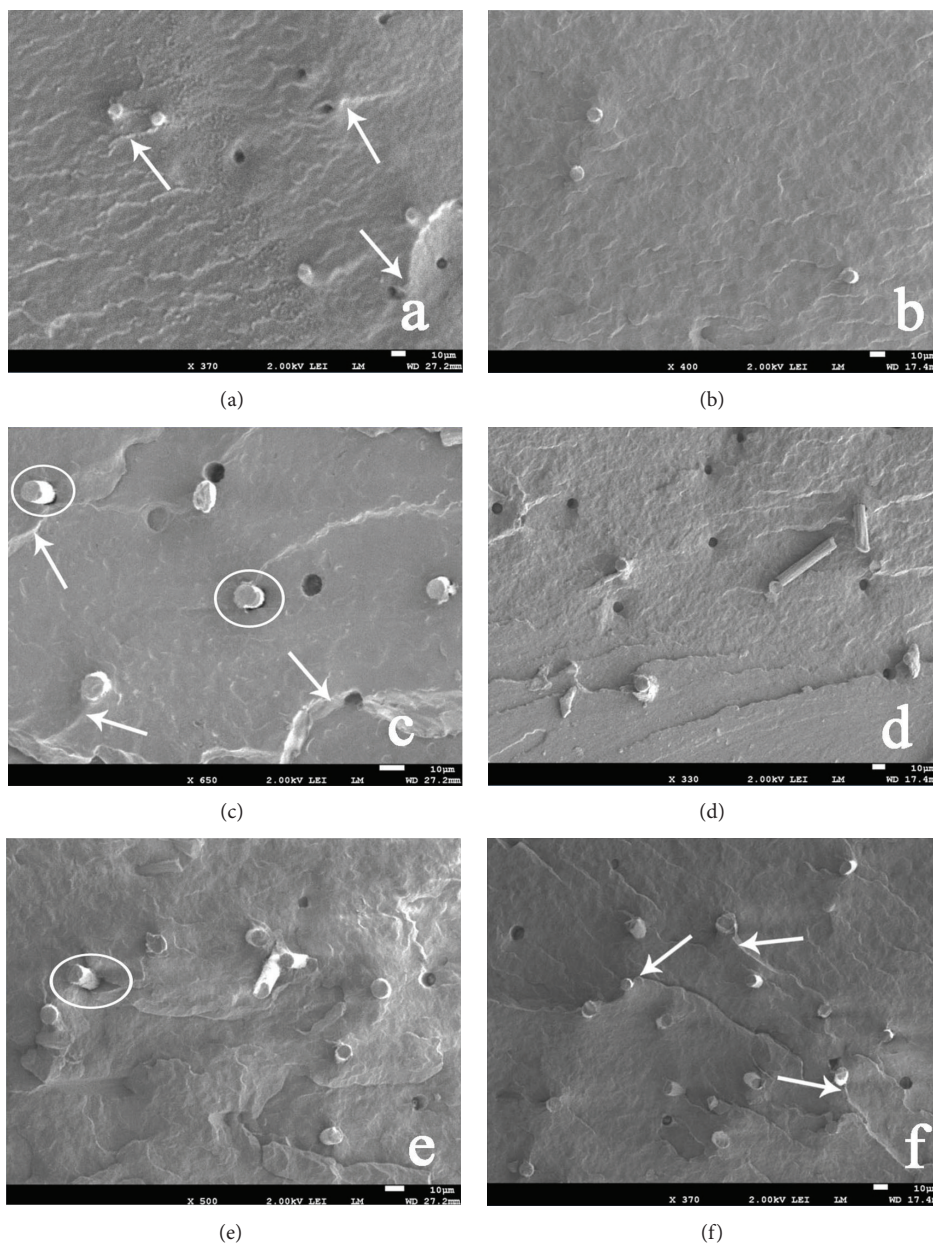


FIGURE 6: SEM images of the impacted samples: (a) 1 pph CF/PP, (b) 1 pph CF/PP/PP-g-MAH, (c) 3 pph CF/PP, (d) 3 pph CF/PP/PP-g-MAH, (e) 5 pph CF/PP, and (f) 5 pph CF/PP/PP-g-MAH.

Acknowledgments

D. Pérez-Rocha wants to thank CONACYT for Scholarship no. 387175 and PROMEP for the support received. The authors are grateful to Asbury Graphite Mills for their kind donation of carbon fibres and to Indelpro for their kind donation of polypropylene (XH1760).

References

- [1] A. Menyhárd and J. Varga, "The effect of compatibilizers on the crystallisation, melting and polymorphic composition of β -nucleated isotactic polypropylene and polyamide 6 blends," *European Polymer Journal*, vol. 42, no. 12, pp. 3257–3268, 2006.
- [2] J. G. Martínez-Colunga, S. Sánchez-Valdés, L. F. Ramos-Devalle et al., "Simultaneous polypropylene functionalization and nanoclay dispersion in PP/Clay nanocomposites using ultrasound," *Journal of Applied Polymer Science*, vol. 131, no. 16, Article ID 40631, 2014.
- [3] Y. Olivares-Maldonado, E. Ramírez-Vargas, S. Sánchez-Valdés et al., "Effect of organoclay structure characteristics on properties of ternary PP-EP/EVA/nanoclay blend systems," *Polymer Composites*, vol. 35, no. 11, pp. 2241–2250, 2014.
- [4] S. Sánchez-Valdes, J. Méndez-Nonell, L. F. Ramos de Valle et al., "Effect of different amine modified clays on the compatibility and clay dispersion of polypropylene nanocomposites," *e-Polymers*, vol. 9, no. 1, pp. 1499–1514, 2014.

- [5] M. Xie, J. Chen, and H. Li, "Morphology and mechanical properties of injection-molded ultrahigh molecular weight polyethylene/polypropylene blends and comparison with compression molding," *Journal of Applied Polymer Science*, vol. 111, no. 2, pp. 890–898, 2009.
- [6] K. Cho, F. Li, and J. Choi, "Crystallization and melting behavior of polypropylene and maleated polypropylene blends," *Polymer*, vol. 40, no. 7, pp. 1719–1729, 1999.
- [7] N. C. A. Razak, I. M. Inuwa, A. Hassan, and S. A. Samsudin, "Effects of compatibilizers on mechanical properties of PET/PP blend," *Composite Interfaces*, vol. 20, no. 7, pp. 507–515, 2013.
- [8] P. Järvelä, L. Shucaï, and P. Järvelä, "Dynamic mechanical properties and morphology of polypropylene/maleated polypropylene blends," *Journal of Applied Polymer Science*, vol. 62, no. 5, pp. 813–826, 1996.
- [9] N. G. Karsli and A. Aytac, "Effects of maleated polypropylene on the morphology, thermal and mechanical properties of short carbon fiber reinforced polypropylene composites," *Materials and Design*, vol. 32, no. 7, pp. 4069–4073, 2011.
- [10] F. Navarro-Pardo, J. Laria, T. Lozano et al., "Shear effect in beta-phase induction of polypropylene in a single screw extruder," *Journal of Applied Polymer Science*, vol. 130, no. 4, pp. 2932–2937, 2013.
- [11] F. Navarro-Pardo, A. L. Martínez-Hernández, V. M. Castaño et al., "Influence of 1D and 2D carbon fillers and their functionalisation on crystallisation and thermomechanical properties of injection moulded nylon 6,6 nanocomposites," *Journal of Nanomaterials*, vol. 2014, Article ID 670261, 13 pages, 2014.
- [12] M. A. López-Manchado, J. Biagiotti, and J. M. Kenny, "Comparative study of the effects of different fibers on the processing and properties of polypropylene matrix composites," *Journal of Thermoplastic Composite Materials*, vol. 15, no. 4, pp. 337–353, 2002.
- [13] D. H. Kim, D. P. Fasulo, R. W. Rodgers, and R. D. Paul, "Structure and properties of polypropylene-based nanocomposites: effect of PP-g-MA to organoclay ratio," *Polymer*, vol. 48, no. 18, pp. 5308–5323, 2007.
- [14] S. H. Lee, M. Balasubramanian, and J. K. Kim, "Dynamic reaction inside co-rotating twin screw extruder. I. Truck tire model material/polypropylene blends," *Journal of Applied Polymer Science*, vol. 106, no. 5, pp. 3193–3208, 2007.
- [15] S. N. Sathe, S. Dew, S. S. Rao, and K. V. Rao, "Relationship between morphology and mechanical properties of binary and compatibilized ternary blends of polypropylene and nylon 6," *Journal of Applied Polymer Science*, vol. 61, no. 1, pp. 97–107, 1996.
- [16] M. S. Sevegney, R. M. Kannan, A. R. Siedle, and P. A. Percha, "FTIR spectroscopic investigation of thermal effects in semi-syndiotactic polypropylene," *Journal of Polymer Science Part B: Polymer Physics*, vol. 43, no. 4, pp. 439–461, 2005.
- [17] D. S. Muratov, D. V. Kuznetsov, I. A. Ilinykh et al., "Thermal conductivity of polypropylene-based composites with multiwall carbon nanotubes with different diameter and morphology," *Journal of Alloys and Compounds*, vol. 586, no. 1, pp. S440–S442, 2014.
- [18] M. F. Diop and J. M. Torkelson, "Maleic anhydride functionalization of polypropylene with suppressed molecular weight reduction via solid-state shear pulverization," *Polymer*, vol. 54, no. 16, pp. 4143–4154, 2013.
- [19] P. Järvelä, L. Shucaï, and P. Järvelä, "Dynamic mechanical properties and morphology of polypropylene/maleated polypropylene blends," *Journal of Applied Polymer Science*, vol. 62, no. 5, pp. 813–826.
- [20] W. C. J. Zuiderduin, C. Westzaan, J. Huétink, and R. J. Gaymans, "Toughening of polypropylene with calcium carbonate particles," *Polymer*, vol. 44, no. 1, pp. 261–275, 2002.
- [21] S. Borysiak, "Fundamental studies on lignocellulose/polypropylene composites: effects of wood treatment on the transcrystalline morphology and mechanical properties," *Journal of Applied Polymer Science*, vol. 127, no. 2, pp. 1309–1322, 2013.
- [22] Z.-Y. Zhao, W.-W. Yao, R.-N. Du et al., "Effect of molecular weight of PDMS on morphology and mechanical properties of PP/PDMS blends," *Chinese Journal of Polymer Science*, vol. 27, no. 1, pp. 137–143, 2009.

Research Article

Parametric Study on Dynamic Response of Fiber Reinforced Polymer Composite Bridges

Woraphot Prachasaree,¹ Attapon Sangkaew,¹
Suchart Limkatanyu,¹ and Hota V. S. GangaRao²

¹Department of Civil Engineering, Prince of Songkla University, Hat Yai, Songkhla 90112, Thailand

²Constructed Facilities Center, Benjamin M. Statler College of Engineering and Mineral Resources, West Virginia University, Morgantown, WV 26505, USA

Correspondence should be addressed to Woraphot Prachasaree; pworaphot@eng.psu.ac.th

Received 16 May 2015; Accepted 24 August 2015

Academic Editor: Jian-Guo Dai

Copyright © 2015 Woraphot Prachasaree et al. This is an open access article distributed under the Creative Commons Attribution License, which permits unrestricted use, distribution, and reproduction in any medium, provided the original work is properly cited.

Because of high strength and stiffness to low self-weight ratio and ease of field installation, fiber reinforced polymer (FRP) composite materials are gaining popularity as the materials of choice to replace deteriorated concrete bridge decks. FRP bridge deck systems with lower damping compared to conventional bridge decks can lead to higher amplitudes of vibration causing dynamically active bridge deck leading serviceability problems. The FRP bridge models with different bridge configurations and loading patterns were simulated using finite element method. The dynamic response results under varying FRP deck system parameters were discussed and compared with standard specifications of bridge deck designs under dynamic loads. In addition, the dynamic load allowance equation as a function of natural frequency, span length, and vehicle speed was proposed in this study. The proposed dynamic load allowance related to the first flexural frequency was presented herein. The upper and lower bounds' limits were established to provide design guidance in selecting suitable dynamic load allowance for FRP bridge systems.

1. Introduction

Fiber reinforced polymer (FRP) composites have increasingly been accepted for use in civil and military infrastructure systems. In general, fiber reinforced polymer (FRP) composites are a combination of fiber reinforcement and polymer matrix. Normally, FRP composites also contain fillers and additives to modify and enhance material properties. Compared to conventional construction materials such as steel and concrete, FRP composite materials have high specific ratios of stiffness and strength per unit self-weight in addition to excellent corrosion resistance leading to longer service life. Over the past half-century numerous applications in many diverse fields such as aerospace, aircraft, marine and offshore, mechanical industries, renewable energy harvesting application, sport, medical applications and automotive (e.g., utility poles for electrical and communication utility, rapidly deployable housing, pipeline for sewage and sea-water applications, FRP turbine blades for wind energy, cold water pipe

for ocean thermal energy conversion, and chimneys/flues in harsh environmental applications) have been noted [1]. However, many applications in infrastructure have been launched since the 1990s. FRP composite materials with various shapes are being used to strengthen and even retrofit structural members. One of the most attractive applications is to replace old deteriorated conventional concrete bridge deck with lightweight FRP deck system. Currently, modern bridge designs to upgrade or even in new bridge construction, with lighter FRP composite structural members are being used for longer span and heavier vehicles. Thus, dynamic response becomes one of the most important issues concerning the design and installation of FRP bridges. In general, the dynamic response under moving loads can induce higher structural responses on FRP bridge decks than in static response conditions. Previous studies [2–4] on FRP bridges under dynamic loads have been limited. From experimental field testing, the dynamic responses of three FRP bridges in West Virginia, United States of America, were evaluated for

TABLE 1: Mechanical properties of laminates for ProDeck4 and ProDeck8.

FRP deck	Laminate	E_{11} (10^4 MPa)	E_{22} (10^4 MPa)	G_{12} (10^4 MPa)	ν_{12}	Tensile strength (MPa)
ProDeck4	CDBM 3415	3.84	0.94	0.47	0.27	350
	DDBM 4015	3.88	0.95	0.46	0.28	330
	Roving	4.24	1.04	0.25	0.28	—
ProDeck8	CDBM 3415	3.38	0.58	0.24	0.26	350
	CDB 400	3.59	0.61	0.29	0.26	310
	Roving	3.45	0.59	0.24	0.26	—

natural frequency, damping, and dynamic load allowance. The measured dynamic load allowances were found to be as high as 0.93 when compared with the typical design value of 0.33 [2]. The dynamic study on FRP bridges also showed that the sectional configuration of bridge decks has seriously accentuated the superstructure dynamic responses when compared with conventional bridges [3]. Earlier researchers have established that the dynamic response of FRP bridge system is most sensitive to vehicle speed and types with observed dynamic load allowance of 0.71 [4]. From extensive review, it is also found that most dynamic load allowance equations provided in bridge design standards [5–16] are applicable to conventional bridges, but not for FRP bridge deck stiffened superstructure systems.

The objective of this study is to investigate the dynamic response such as natural frequencies and dynamic load allowances for design purposes. The influences of bridge geometry, vehicle speed, and positions on the dynamic response are also evaluated herein. As mentioned above, there is little progress in the dynamic responses on FRP deck-stringer bridge systems. The present study is expected to fill the gap partially and to analyze and design FRP bridge deck stiffened superstructural systems by conducting the above-mentioned parametric study. Since the field study of dynamic behavior of FRP bridge deck systems is expensive and time consuming, the parametric study as a function of bridge deck type and vehicle parameters has been carried out using finite element analysis.

2. Multi-Cellular FRP Bridge Decks

In this study, two different FRP bridge decks, commercially known as ProDeck4 and ProDeck8, were modeled for their dynamic responses. Their structural performance and design issues were comprehensively evaluated [17–19]. The dynamic response in this study is presented as a sequel to static response of the two FRP bridge decks. Both ProDeck4 and ProDeck8 are developed to sustain AASHTO (American Association of State Highway and Transportation) HS25 truck load.

These FRP decks are produced by pultrusion method. In general, the predominant fibers in applications of structural members are glass, carbon, and organic fiber with a thermoset resin used for the pultrusion process. However, glass fibers (particularly E glass fibers) combined with polyester or vinyl ester resins become the most common uses for FRP bridge decks. The multicellular shaped low-profile FRP ProDeck4 is

made of E-glass fiber and vinyl ester resin. Fiber architectures of ProDeck4 were designed with three main laminates as (1) warp triaxial fabrics (combined with glass mat) known as CDBM 3415 ($0^\circ/45^\circ/-45^\circ/\text{CSM}$); (2) weft triaxial fabrics (combined with glass mat) known as DDBM 4015 (multidirectional fabric laminate ($45^\circ/90^\circ/-45^\circ/\text{CSM}$)); and (3) continuous strand rovings. CDBM and DDBM laminates are a stitch bonded composite fabric combining double bias ($45^\circ/-45^\circ$) piles with warp (0°) or (90°) into a single multidirectional fabric for CDBM or DDBM, respectively. Also, each laminate fabric is combined with a continuous glass mat for enhancing thermomechanical properties.

Similarly, three different laminates of ProDeck8 are (1) CDBM 3415 (multidirectional fabric laminate with orientation and stacking sequence ($0^\circ/45^\circ/-45^\circ/\text{CSM}$)); (2) biaxial fabrics known as CD400 (bidirectional fabric laminate of $45^\circ/-45^\circ$); and (3) continuous strand roving. ProDeck8 module has a rectangular cross section with a diagonal stiffener. Both ProDeck 4 and ProDeck8 have fiber volume fraction of approximately 50 percent. The laminated fabrics of both FRP bridge decks continue from the flange to web and then again to the flange. The high elongation polymer used for both FRP decks was vinylester resin. Typically, FRP composite materials exhibit thermomechanical properties of varying magnitudes in different directions. Thus, the component stiffness of FRP deck modules can be determined using the interaction properties of constitutive materials in each composite layer. The mechanical properties of FRP deck modules to model ProDeck4 and ProDeck8 deck systems are given in Table 1. In addition, fiber architecture and laminate stacking sequence of both FRP deck modules are presented in Figure 1.

3. Bridge Configurations

In this study, two-lane FRP decks and steel stringer bridges were modeled to perform the dynamic responses of the superstructure system. Multicellular FRP decks (ProDeck4 and ProDeck8) and H-shape wide flange steel stringers were assembled together for all bridge superstructure models. The width of the bridge models was chosen to be a constant 9.50 m in width for two traffic lanes. Two different span lengths (12 and 18 m) of single span bridge systems were selected with steel wide flange stringer size of $W36 \times 150$. The various steel stringer spacings were considered to be 1.22, 1.83, and 2.24 m for modeling with 7, 5, and 4 steel stringers, respectively, with typical arrangement as shown in Figure 2.

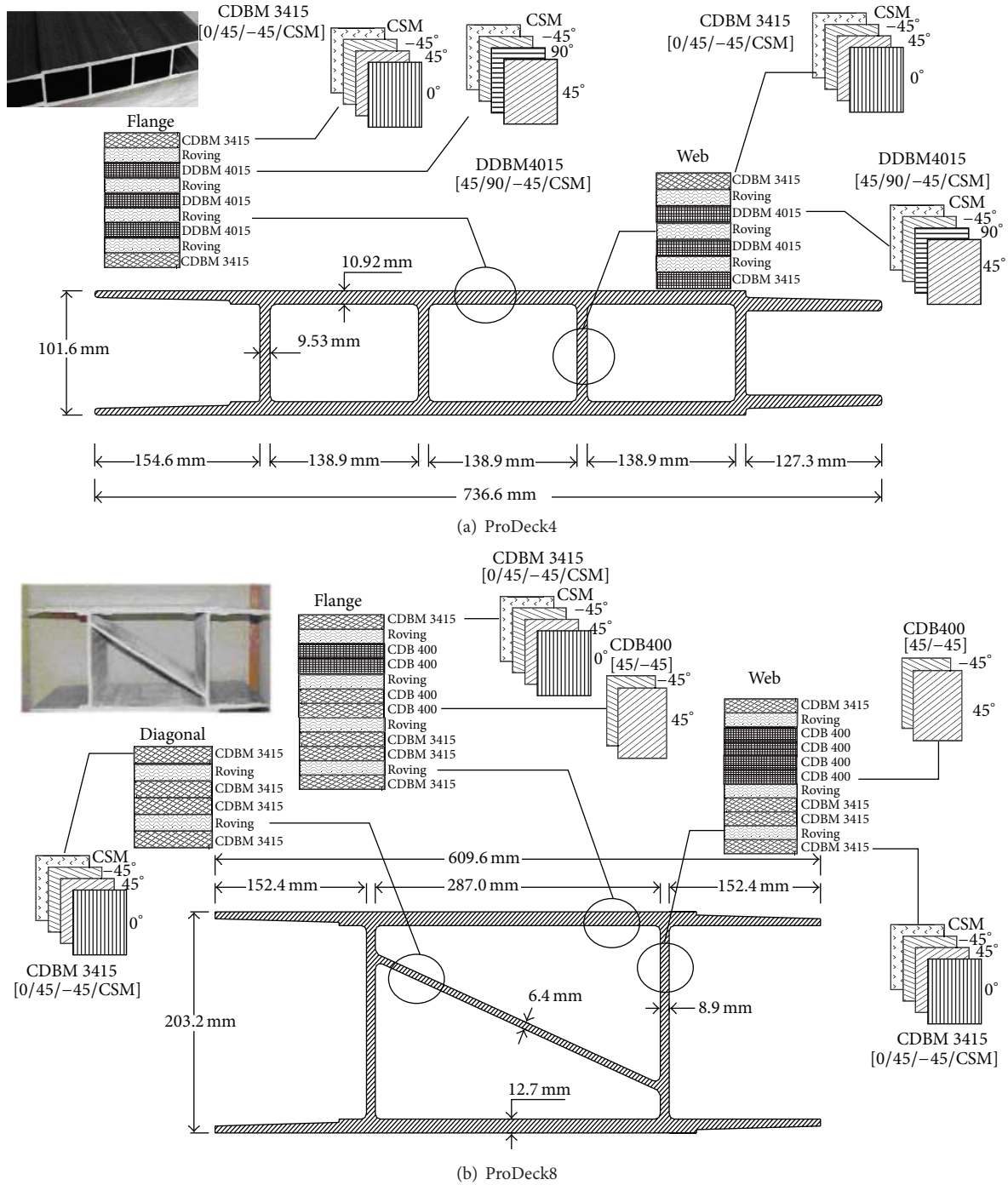


FIGURE 1: Fiber architecture and stacking sequence.

4. Loading Patterns

In general, the dynamic response of bridge superstructure models depends on many factors, including vehicular loading patterns, bridge configurations, road surface conditions, and vehicle speeds. Three different dynamic loading patterns were simulated as follows:

Loading pattern 1 (Case A): a single truck travels along the bridge span.

Loading pattern 2 (Case B): two trucks travel along the span in the same direction.

Loading pattern 3 (Case C): two trucks travel along the span in the opposite direction.

To evaluate maximum dynamic deflection and observe critical vehicle speed, the truck loading speed is varied between 20 km/hr and 100 km/hr with an interval 20 km/hr. The AASHTO HS25 trucks were selected to simulate the design truck loading conditions. In addition, there are six different

TABLE 2: Bridge model parameters.

Bridge model	Parameters								
	Deck type	Bridge length	Traffic direction*	Speed (km/hr)	Number of stringers	W_{total} (m)	$W_{traffic}$ (m)	S (m)	d (m)
G7					7 (W36 × 150)			1.22	0.91
G5	P4, P8	12, 18 m	↑, ↑↑, and ↓↓	20, 40, 60, 80, and 100	5 (W36 × 150)	10.10	9.14	1.83	0.91
G4					4 (W36 × 150)			2.24	1.21

Note. * Traffic direction: ↑ a single truck travels along the bridge span, ↑↑ two trucks travel along the span in the same direction, and ↓↓ two trucks travel along the span in the opposite direction. P4 = ProDeck4, P8 = ProDeck8.

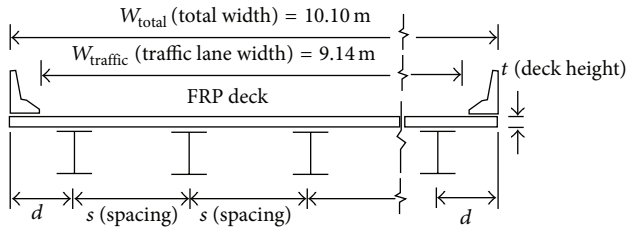


FIGURE 2: Typical bridge model configuration.

bridge geometry models evaluated with three (truck) loading patterns. For loading pattern 1 (1-truck loading), three loading positions are follows: (1) left wheel is placed directly over the centerline of the exterior stringer (A-1); (2) left wheel is placed directly over the centerline of the first interior stringer (A-2); and (3) truck loading is placed on the middle of the traffic width (A-3). The two truck loadings (loading patterns 2 and 3) consisted of the same loading positions as case of one truck loading; that is, (4) left wheel of the left truck is placed directly located on the centerline of the exterior stringer (B-1, C-1), (5) left wheel of the left truck is placed directly over the centerline of the first interior stringer (B-2, C-2); and (6) center line between both trucks corresponds to the center line of the traffic width (B-3, C-3). Totally, nine subcases of (truck) loading conditions were investigated for each bridge model. All bridge models and design truck loading conditions are demonstrated and summarized in Table 2 and Figure 3.

5. Finite Element Modeling

A general purpose finite element modeling and analysis package, ANSYS [20], with a pre- and postprocessor program was employed herein for dynamic analysis of FRP bridge deck system. Bridge superstructure geometry, nodes, elements, and element meshes were automatically generated by ANSYS. Generally, the truck loading conditions are well below the critical stress leading to nonlinear geometry and material behavior of bridge system models [21]. Thus, the finite element models based on linear elastic analysis are adopted in this parametric study. The load-deflection response of a single ProDeck4 module is presented in the Appendix. ProDeck4 and ProDeck8 are modeled using orthotropic laminated shell elements (SHELL93 [20]). Eight-node SHELL93 element had six degrees of freedom at each node (translations in the nodal x , y , and z directions and rotations about the nodal x -, y -, and z -axes). FRP deck models are assembled using two main components as (1) flange and (2) web portions. The

material properties of FRP deck models are shown in Table 1. The fiber orientation in each layer of a laminate is followed by the fiber architecture as shown in Figure 1. The web and flange steel stringer are modeled using the quadrilateral isotropic shell elements. A bilinear stress and strain relation of Grade 36 steel with elastic modulus of 200 GPa is used for steel stringers. All parts of the finite element FRP deck and steel stringer models are bonded together. The interaction at the FRP deck and stringer interfaces is modeled as having 100% structural composite and noncomposite actions in all FRP bridge deck system models. For 100% compositeness, the interface between FRP deck and steel stringer model is completely connected; thus, 100% structural composite action at the model interface is attained. In order to develop noncomposite behavior, the interface or link elements are introduced between FRP bridge deck and steel stringers as shown in Figure 4. The high vertical stiffness compared with in-plane transverse stiffness of the interface or link element can be used for this purpose. The boundary conditions were assigned to be roller type (constrained in bridge x and z directions) and pinned (constrained in bridge x , y , and z directions) at the end of steel stringers. The finite element models of FRP bridge decks with steel stringers developed following the above principles were made to investigate the dynamic responses under HS-25 truck loading conditions.

Structural damping in superstructure models includes material and structural damping. In general, most of the steel wide flange stringer bridges inherently have little variation in damping, especially if the deck is made of concrete. Thus, damping is not a main parameter to control the responses of a bridge [22]. However, accurate damping is needed for structural evaluation of accurate dynamic responses. It is found that low self-weight and low damping (0.5% from field data and previous studies [2, 3, 23]) can lead to excessive vibration of an FRP deck-steel stringer bridge. Therefore, the damping ratio of 0.5% was also employed in this parametric study. For dynamic truck loading simulation, AASHTO HS25 (see Figure 5) that resembles a semitrailer truck was selected for a vehicular load. The front axle is 44 kN, positioned 4300 mm behind the drive axle that is 178 kN, and the rear trailer axle is also 178 kN and is located at a distance of 4300 mm. To simulate a moving truck, subroutine programs of the load step method were imposed on the finite element program package. In this method, truck axles on a bridge model will move forward with a constant distance for each stepping-time increment as demonstrated in Figure 6. The number of discrete time instants depends on length of bridge span. To incorporate bridge surface roughness, the power spectral

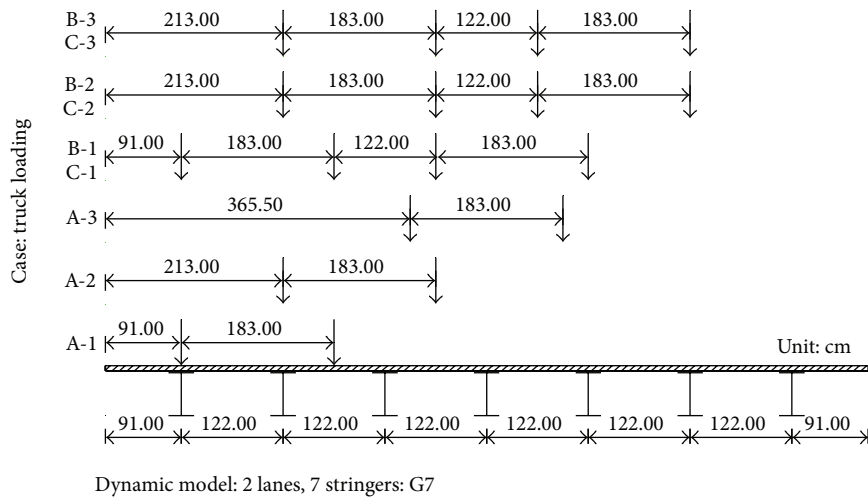
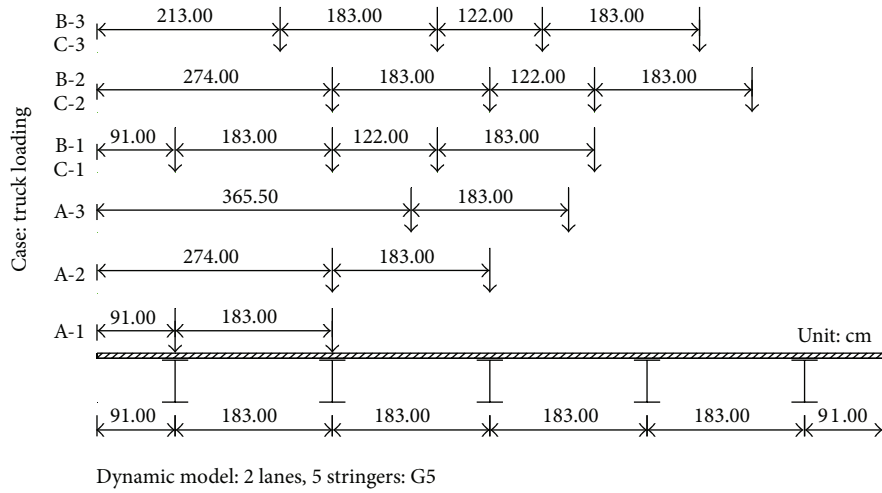
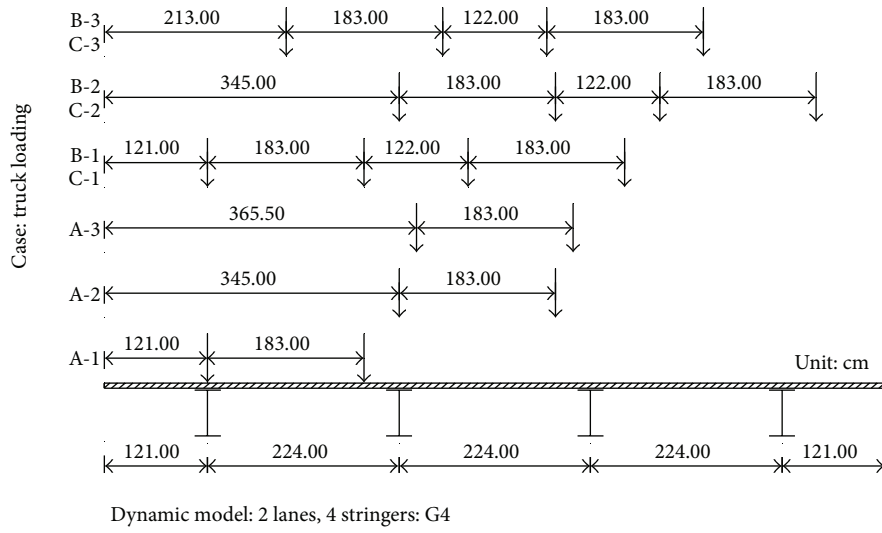


FIGURE 3: Summary of bridge models and design truck loading conditions.

TABLE 3: Comparison between finite element and experimental results for FRP deck systems.

Method	Load case	Applied load (kN)	Average max. Deflection (cm)		Relative deflection (cm)
			Stringer	FRP deck	
Experimental		89.0	0.170	1.199	1.029
Finite element			0.067	1.078	1.011
Experimental		89.0	0.106	0.146	0.040
Finite element			0.079	0.117	0.038
Experimental		177.9	0.170	0.516	0.346
Finite element			0.115	0.445	0.330

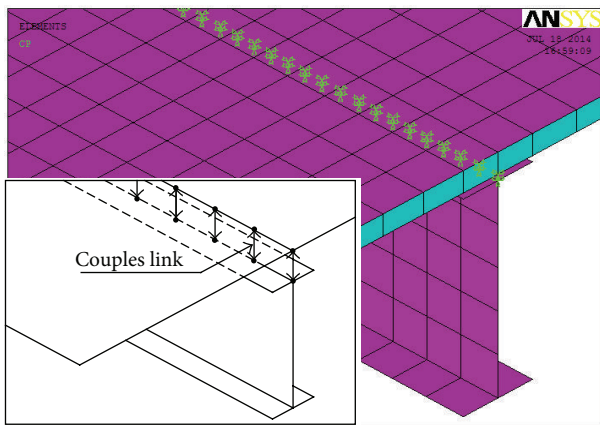


FIGURE 4: Link between deck and steel.

density function (PSD) was used for this purpose [24], since the bridge surface profiles are simply assumed to be random. In this study, the bridge surface roughness for good surface condition with roughness coefficient of $15(10^{-6}) \text{ m}^3/\text{cycle}$ was simulated using gap elements to interconnect with shell elements of FRP bridge models.

6. Verification of Finite Element Models

In this section, finite element bridge models were validated and calibrated through the experimental data [25, 26]. Finite element bridge models were further verified by FRP deck-stringer bridge system under AASHTO HS25 truck load and experimental modal analysis. The static load results and frequencies obtained from laboratory experiments were compared with the analytical results. For static load results, two different FRP deck-steel stringer systems were conducted under static wheel loads as follows: (1) FRP bridge deck was simply placed on two stringers with 3450 mm spacing and (2) FRP bridge deck was positioned on three stringers with equal spacing of 1730 mm. Three different loading cases were performed to validate structural responses. Based on this study, the relative deflection of FRP deck systems was in agreement with the finite element results as shown in Table 3. The finite element results showed that the maximum differences in the relative deflection response comparing with the experimental results [25, 26] were less than 5 percent. It is obvious that the structural stiffness of FRP bridge deck

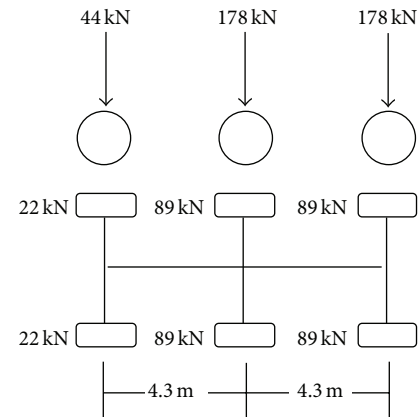


FIGURE 5: AASHTO HS25 semitrailer truck.

system decreases with increases in stringer spacing, that is, fewer stringers. It was observed that the relative deflection of loading Case 1 was higher than the deflection limit 0.2% of stringer spacing (center to center). The warping and lateral torsional effects of steel stringers are attributed to high stresses and strains in the FRP deck flange, that is, global stiffness reduction of the FRP deck system.

For modal analysis, bridge deck finite element models were evaluated using block Lanczos method. The frequencies and mode shapes obtained from finite element results are summarized and compared with the experimental results [25, 26] as shown in Figure 7. The finite element mode shapes and modal ordering were in agreement with the modes from the experimental data and the modal analysis. The percent difference between finite element and experimental results was ranged from 2 to 6 percent for FRP ProDeck8 bridge models and from 5 to 20 percent for FRP ProDeck4 bridge models. For ProDeck4 bridge models, a consistent difference may indicate an error in material properties such as inaccuracy in the data (e.g., material density) in the finite element model. It was observed that torsional mode was found to be the first mode shape in both the finite element and experimental results as the dominant mode. The lowest frequency of finite element first mode correlated with the lower torsional stiffness of FRP deck models. The material data using finite element models were obtained from the individual deck modules, and the plate action of FRP deck system was not accounted for in this finite element analysis. The plate action in FRP deck system under torsional

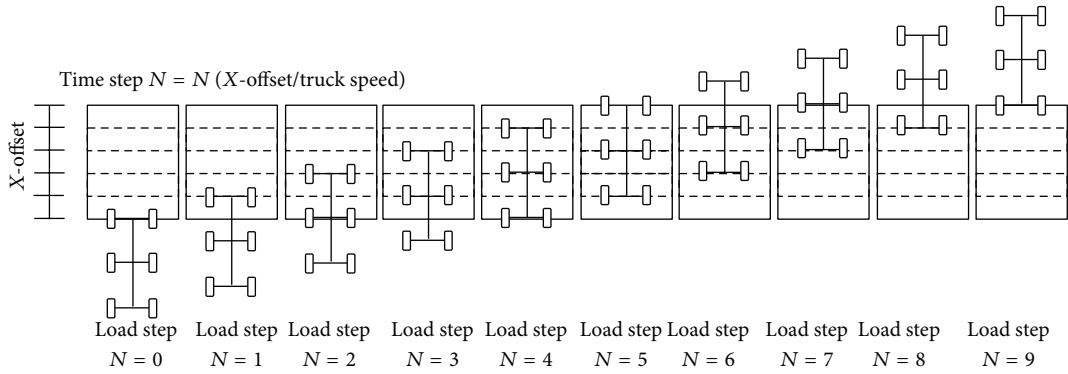


FIGURE 6: Simulation of moving truck using the load-step method.

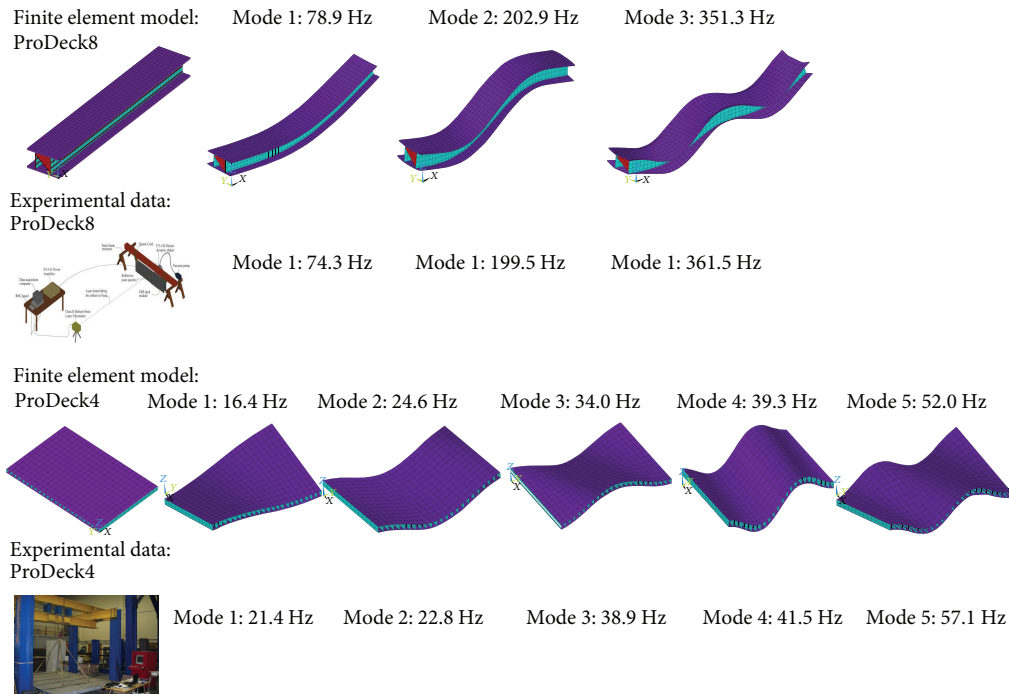


FIGURE 7: Frequencies and mode shapes of FRP composite decks.

and/or in-plane loadings is approximately about 20% higher than an individual deck module without plate action (i.e., only beam effect). However, in case of an isotropic system (conventional materials), the plate action was about twice that of a beam. The lower plate action in FRP composite systems was attributed to lower Poisson's effect in the transverse direction compared to the longitudinal direction [19].

7. Dynamic Load Allowance (DLA)

Studying the dynamic effect of bridge models is tied to accurate determination of dynamic load allowance (DLA). Reviews of various design codes were reported for conventional highway bridges [22, 27, 28]. Disagreement on the dynamic load allowance results from different codes and studies were found due to various uncertainties in input parameters. Arguments on the dynamic load allowance

evaluation have been inconclusive particularly in FRP bridge systems. The dynamic load allowance of FRP bridges was evaluated using the parametric study in this study. From the most rational approaches based on the theory of structural dynamics, the dynamic load allowance can be defined as the maximum instantaneous dynamic response divided by the maximum static response developed [2]. In this definition, both the maximum dynamic and static responses were found in the different locations through truck loading at different time intervals. The dynamic load allowance using deflection and strain calculation was commonly determined as given in the following equations, respectively:

$$DLA = \frac{(D_{d \max} - D_{s \max})}{D_{s \max}}, \tag{1}$$

$$DLA = \frac{(\epsilon_{d \max} - \epsilon_{s \max})}{\epsilon_{s \max}}, \tag{2}$$

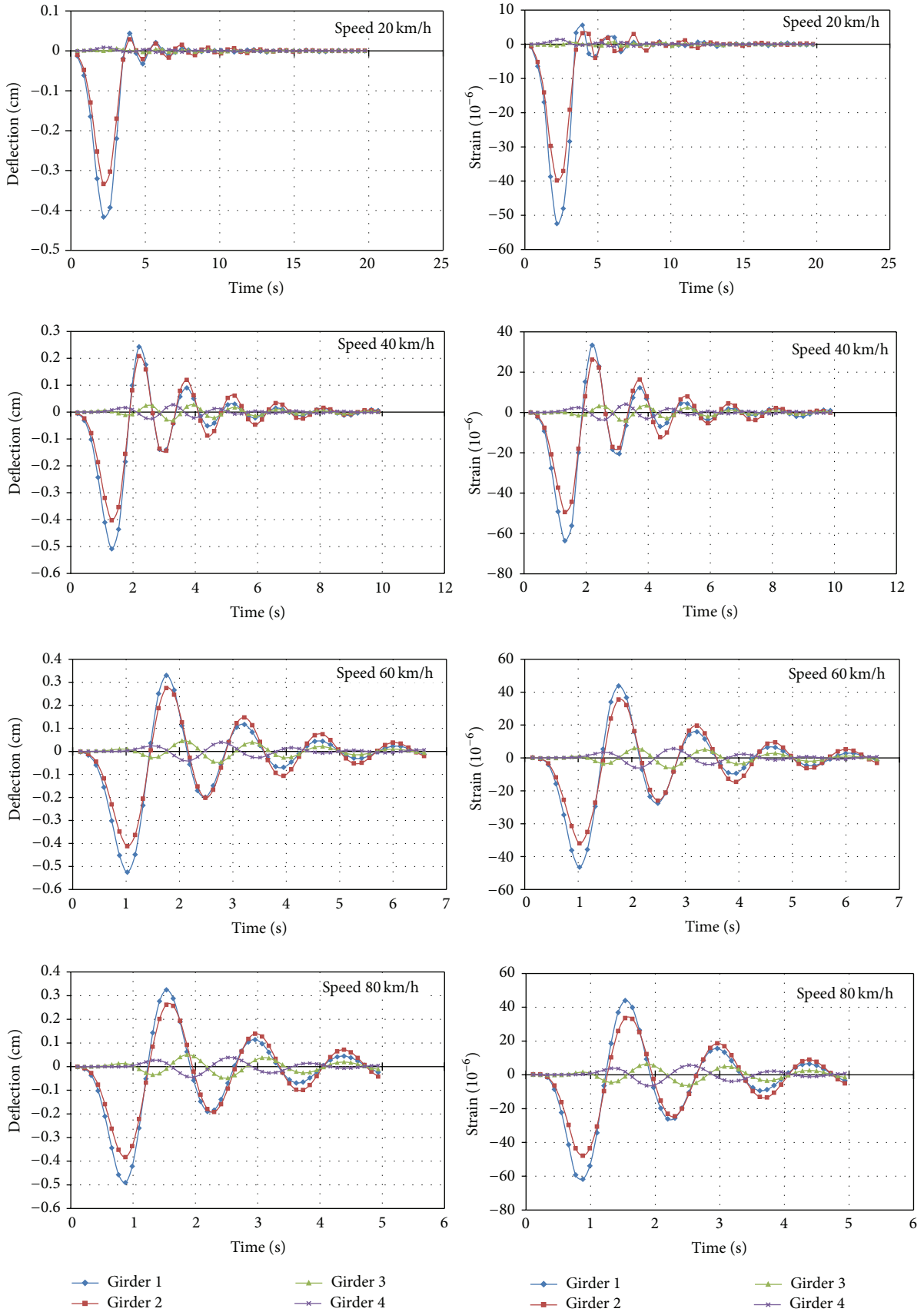


FIGURE 8: Continued.

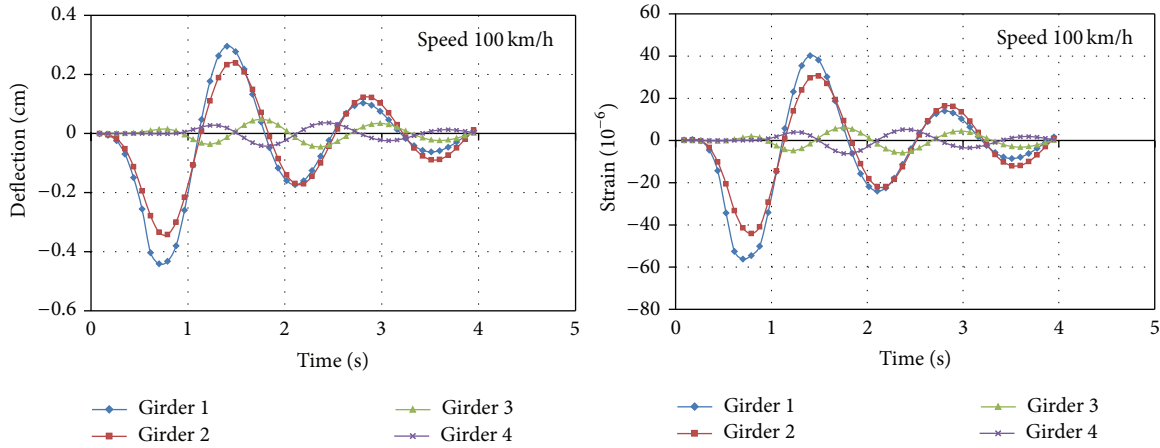


FIGURE 8: Time history of dynamic deflection and strain: FRP bridge (P4G4L12).

where $D_{d\max}$ is the maximum dynamic deflection, $D_{s\max}$ is the maximum static deflection, $\varepsilon_{d\max}$ is the maximum strain under the truck loading at traveling speed, $\varepsilon_{s\max}$ is the maximum static strain under the truck loading.

8. Parametric Study

The parameters affecting the dynamic load allowance can be classified into two different main sources as (1) bridges including damping, frequency, and road surface profiles and (2) vehicles including speed, vehicle mass, damping, and tyre conditions. In general, the major parameters such as natural frequency, vehicle speed, bridge geometry and stiffness, and road surface dominate the dynamic responses of bridge models. In the following parametric study, a total of 648 FRP deck-steel stringer bridge models (composite and noncomposite cases) were investigated through finite element simulation. The dynamic load allowance in the present study was correlated with the previous research data [2–16, 22, 29] obtained from fields, laboratory experiments, and analytical methods. Four parameters as (1) stringer spacing, (2) bridge span, (3) bridge deck, and (4) truck speed were mainly considered under cases of truck loading and a specific surface road condition as mentioned above. From analytical simulation, the time history of the dynamic deflection and strain at the midspan of the FRP bridge deck system model P4G4L12 (refer to Table 2: ProDeck4 bridge models with 4 steel stringers of 12 m span length) are presented as shown in Figure 8.

Accounting for three different cases of trucks and positions (Cases A, B, and C as in Figure 3) on the bridge models, investigations were conducted to understand variations in dynamic load allowance factor. The results showed that only one truck traveling over the bridge under a specific road surface condition affects the dynamic load allowance more than other load cases. The exterior stringer under the traffic lane experiences the greatest responses of both deflection and strain. Also, the dynamic load allowance provided by only one truck loading at the midtransverse bridge span is larger than that by the same truck at different positions. Since the

maximum static response increases with the increase in the number of truck loadings, the maximum dynamic response slightly increases for the same number of truck loadings. The dynamic response results of FRP bridge models correspond to the previous study on concrete slab bridges [22] and Ontario Highway Bridge Design Code (OHBD) [9]. The dynamic load allowance introduced by OHBD [9] was provided as a function of the number of axles per span; that is, lower number of axles per span gives higher dynamic load allowance.

For the effect of vehicle speed, the vehicle speed ranging from 20 km/hr to 100 km/hr with an interval of 20 km/hr was simulated using the time step method. To investigate the effect of different vehicle speed, dynamic responses at the same truck position (see the time history of the dynamic deflection in Figure 8) were considered for this purpose. It was clearly observed that the absolute dynamic deflection at the same truck loading position gradually increases with an increase in the truck loading speeds to 60 km/hr. When the truck speed is higher than 60 km/hr, the dynamic deflection decreases. Therefore, the higher truck speed may not increase the dynamic response of the FRP bridge models. The truck speed causing the maximum dynamic deflection at the same truck loading position can be defined as the critical speed or resonant speed. In our theoretical study, the critical speed or resonant effect of moving loads on bridges [29] is presented in terms of the fundamental frequency of the bridge, vehicle speed, and vehicle axle spacing. Originally, this critical speed was developed for railway bridges under a series of moving loads. As mentioned before [29], the critical speed is particularly applicable for short span bridges due to multi-axle vehicular loads considered as a series of moving loads. However, FRP bridges are significantly lighter than conventional bridges with low self-weight and damping, which may lead to excessive bridge dynamic response leading to loss of accuracy in critical speed determination. In addition, different trucks have different critical speeds resulting in bridge dynamic response as highest. The relations between the dynamic load allowance and truck speeds are illustrated in Figure 9. It was found that the truck speed of 40 km/hr and 60 km/hr results in the highest dynamic load allowance for different bridge spans. The finite element analytical results in

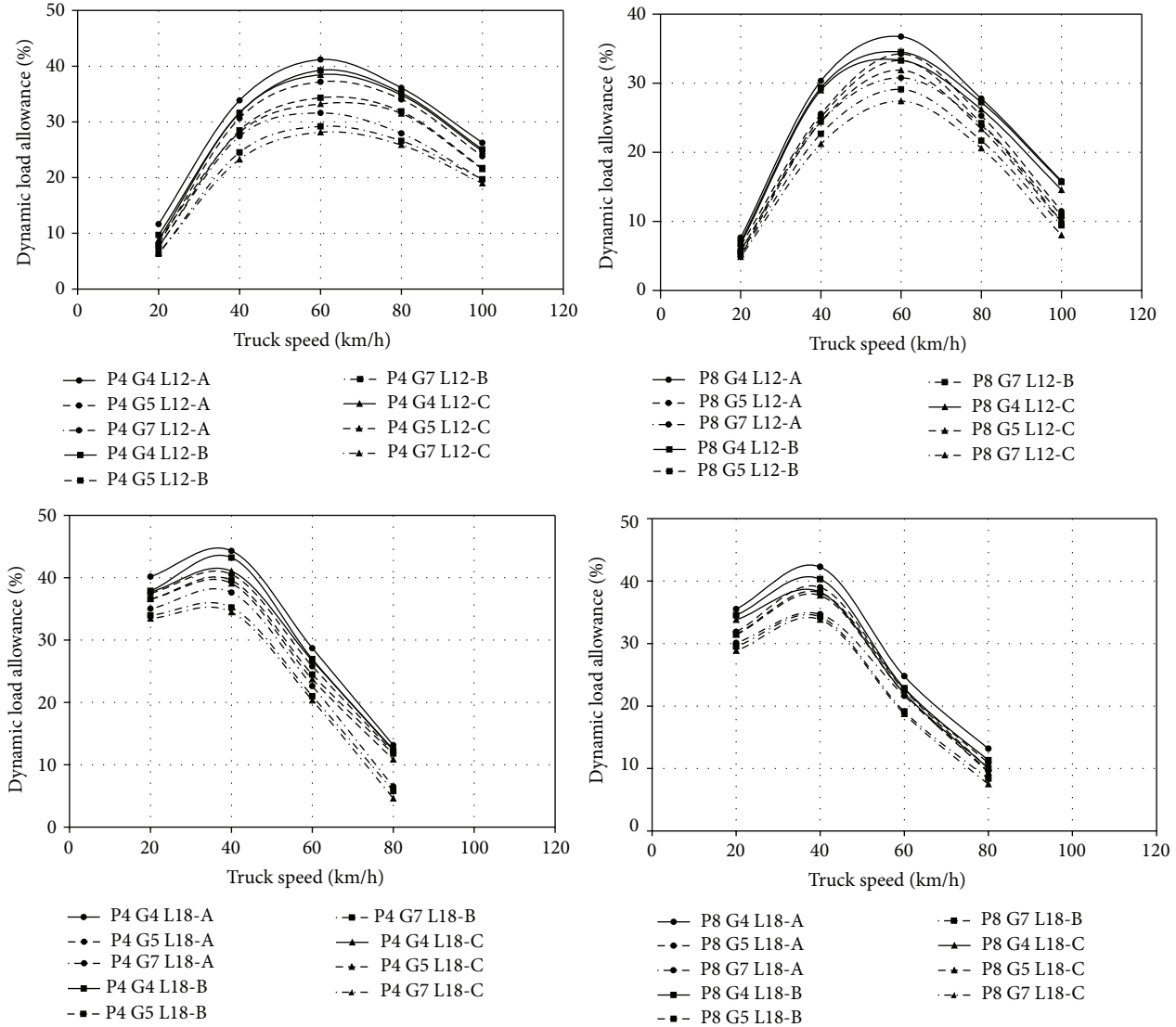


FIGURE 9: Relations between truck speeds and DLA.

this study were compared with the dynamic load allowance and speed provided by the Federal Highway Administration (FHWA 1995) [30]. It indicated that the trend of the dynamic load allowance is similar to that of FHWA (1995) [30]. It should be noted that the maximum dynamic load allowance occurs at lower vehicle speeds when the length of FRP bridge span increases due to an increase of bridge fundamental frequency. From various specifications [5–16], it is seen that the dynamic load allowance based on a bridge span length underestimates the values for the FRP bridges by about 25% as shown in Table 4. The dynamic load allowance and stinger spacing relations are shown in Figure 10. The dynamic load allowance tended to decrease as the span length of the bridge increases while the dynamic load allowance decreased with increase in span length.

9. Simplified Dynamic Load Allowance

From our results, better prediction of the dynamic load allowance for FRP bridges may be accomplished by

considering several parameters as natural frequency, span length, and vehicle speed. The dynamic load allowance can be presented in terms of an allowance (β) for initial vibrations of vehicle coming onto the bridge and the effects (α) from a smoothly rolling mass crossing a stringer as given in (3). Equation (3) is based on the previous study proposed by Walker and Veletsos [31]. The dynamic load allowance can be directly determined by adding effects of initial oscillations (β) and a smoothly rolling mass crossing a beam (α) together. By using DLA data (finite element results) with bridge and vehicle parameters, the allowance factor (β) can be estimated for simplified dynamic load allowance equation. Thus, the upper and lower bounds dynamic load allowance can be developed using this simplified equation with varying bridge frequency:

$$DLA = \beta + \alpha \text{ or}$$

$$DLA = \beta + \frac{V}{(2Lf)}, \tag{3}$$

TABLE 4: Dynamic load allowance of various specifications.

Specification	Dynamic load allowance	Span length	
		12 m	18 m
AASHTO 1998 [5]	0.33	0.33	0.33
AASHTO 2007 [6]	$50/(125 + L)$, L in ft	0.30	0.27
BS5400 [7]	0.25	0.25	0.25
JRAS [8]	$20/(50 + L)$, L in m	0.32	0.29
OHBDC [9]	0.4 for one axle	0.40	0.40
France (modified 1989) [10]	$0.8/(1 + 0.2L)$, L in m	0.24	0.17
DIN 1072-1987 [11]	$0.4 - 0.008L$, L in m	0.30	0.26
Norm NEM 1008 [13]	$40/(100 + L)$, L in m	0.36	0.34
Australia NAASRA 1989 [14]	$50/(125 + L) \leq 0.3$, L in ft	0.30	0.27
Switzerland SIA160 [15]	$0.05(L + 100)/(L + 10)$, L in m	0.25	0.21
Korea KBDS [16]	$15/(40 + L) \leq 0.3$, L in m	0.29	0.26
Parametric study (note: results from ProDeck4 and ProDeck8 models)	0.4 (average for 12–18 m)		

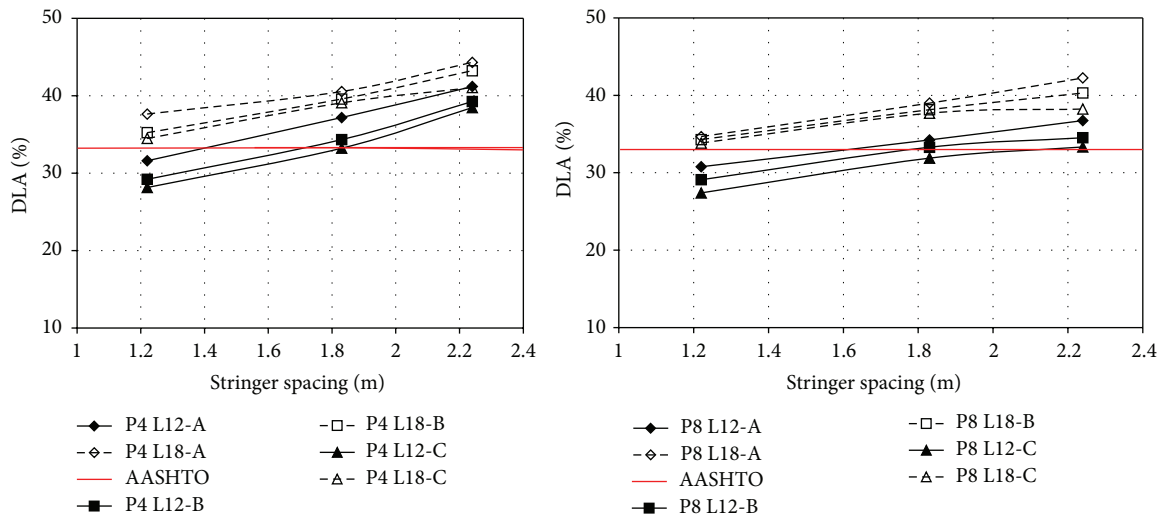


FIGURE 10: Relations between stringer spacing and DLA.

where V is a truck speed (m/s), L is a span length (m), and f is the first flexural frequency (Hz).

Based on this parametric study (the first flexural frequency of the finite element models is equal to 3.5 Hz), the allowance (β) for initial vibrations of a vehicle onto the FRP bridges was evaluated and suggested to be 0.30. Alternatively, the dynamic load allowance of the FRP bridges may be determined using $0.3 + V/(2Lf)$ for the bridge length of 10–20 m. For example, the relation between dynamic load allowance and bridge span based on (3) is presented and compared with the standard codes of practice as shown in Figure 11.

Lack of accurate data leads to having a more conservative dynamic load allowance value for design purposes. The simplified dynamic load allowance using the first major frequency of FRP bridge models was developed herein. The results from various parameters in (3) are used to arrive at both the upper and lower limits of the dynamic load allowance as shown in Figure 12. These upper and lower

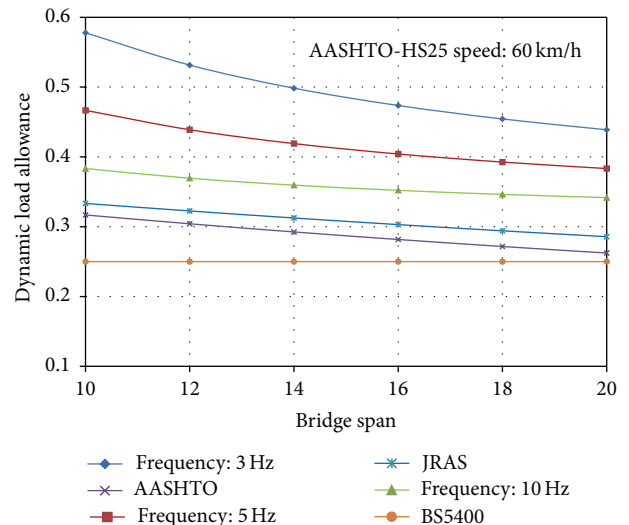


FIGURE 11: DLA with different bridge frequency and span length.

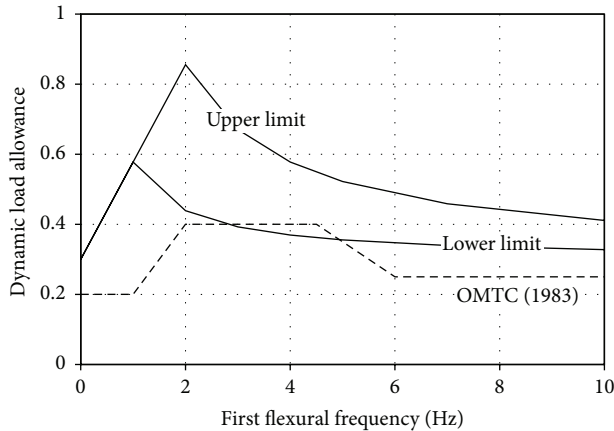


FIGURE 12: Relation between DLA and frequency.

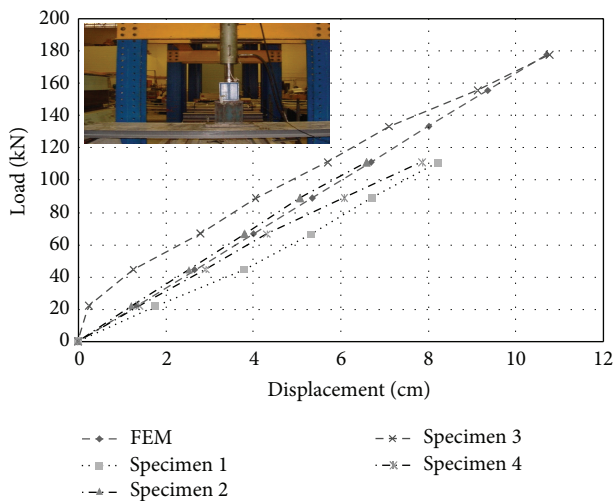


FIGURE 13: Load-deflection response of a single ProDeck4 module.

bounds were established as preliminary design guidelines. It should be noted that the upper and lower bounds of the dynamic load allowance are based on the dynamic response of FRP bridge models as mentioned in this study.

10. Conclusions

The present study has aimed at investigating dynamic responses of FRP bridge systems. A total of 648 FRP bridge models in different bridge configurations and load patterns were simulated using finite element analysis. The dynamic responses of FRP bridge models with noncomposite structural action between FRP deck and a stringer are higher than those with 100% structural composite action. The trend of the dynamic load allowance with various vehicle speeds is similar to that given by FHWA (1995). From standard specifications [5–16], the dynamic load allowances may not be an accurate representation of the field and analytical data for FRP bridge systems. The dynamic load allowance based on current design specifications underestimates the values for FRP bridges by about 25%. A more accurate prediction of the dynamic load allowance for FRP bridges is proposed herein by accounting

for realistic input parameters such as a natural frequency, span length, and vehicle speed. The dynamic load allowance equation in terms of an allowance (β) for initial vibrations of vehicle and the factor (α) about a smoothly rolling mass was developed. The simplified dynamic load allowance using the first major frequency was established. Both the upper and lower bounds of the dynamic load allowance are suggested as a design guidance for FRP bridges with span length ranging from 10 to 20 m.

Appendix

Component level: load and deflection response of a single ProDeck4 module is presented (see Figure 13).

Conflict of Interests

The authors declare that there is no conflict of interests regarding the publication of this paper.

Acknowledgments

This study was partially supported by Structural Engineering and Applied Mechanics (STREAM) Research Group under Grant ENG-51-2-7-11-022-S, Department of Civil Engineering, Faculty of Engineering, Prince of Songkla University, Hat Yai, Songkhla, Thailand. The authors would also like to thank anonymous reviewers for their valuable and constructive comments.

References

- [1] I. M. Daniel and O. Ishai, *Engineering Mechanics of Composite Materials*, Oxford University Press, Oxford, UK, 2nd edition, 2006.
- [2] S. Aluri, C. Jinka, and H. V. S. GangaRao, "Dynamic response of three fiber reinforced polymer composite bridges," *Journal of Bridge Engineering*, vol. 10, no. 6, pp. 722–730, 2005.
- [3] Y. Zhang and C. S. Cai, "Load distribution and dynamic response of multi-girder bridges with FRP decks," *Engineering Structures*, vol. 29, no. 8, pp. 1676–1689, 2007.
- [4] M. J. Robinson and J. B. Kosmatka, "Dynamic response of a light-weight composite bridge," in *Proceedings of the 8th International Conference on Structural Dynamics (EURODYN '11)*, pp. 1430–1437, Leuven, Belgium, July 2011.
- [5] American Association of State Highway and Transportation Officials (AASHTO), *Standard Specifications for Highway Bridges*, American Association of State Highway and Transportation Officials (AASHTO), Washington, DC, USA, 1998.
- [6] American Association of State Highway and Transportation Officials (AASHTO), *LRF Bridge Design Specification*, SI Unit, American Association of State Highway and Transportation Officials (AASHTO), Washington, DC, USA, 3rd edition, 2007.
- [7] *BS5400, Concrete and Composite Bridge Part 2: Specification for Loads*, British Standards Institution, London, UK, 1978.
- [8] Japan Road Association's Specification (JRAS), *Part 1: Common Specifications for Highway Bridges*, Japan Road Association (JRA), Tokyo, Japan, 1996.
- [9] OHBDC, *Ontario Highway Bridges Design Code*, Highway Engineering Division, Ministry of Transportation and Communications, Ontario, Canada, 1983.

- [10] Ontario Ministry of Transportation (OMT), *Ontario Highway Bridges Design Code*, Highway Engineering Division, Ontario, Canada, 3rd edition, 1991.
- [11] *Cahier des Prescriptions Communes Applicable aux Marches de Travaux Publis Relevant des Services de l'Equipement*, Ministere de l'Equipement et du Logement, Ministere des Transports, Paris, France, 1973.
- [12] Deutsche Industire Normen (DIN 1072), *Road and Footbridges: Design Loads*, Deutsche Industire Normen (DIN), Berlin, Germany, 1983.
- [13] *NEN 1008: Voorschriften voor het Ontwerpen van Stalen Bruggen (VOSB 1963)*, NNI, 1963.
- [14] NAASRA, *Bridge Waterways Hydrology and Design*, National Association of Australia State Road Authorities, Sydney, Australia, 1989.
- [15] *SI160: Einwirkungen auf Tragwerke*, Entwurf, Schweizerischer Ingenieur- und Architektenverein, Zürich, Switzerland, 1988.
- [16] Korea Bridge Design Specifications (KBDS), *Roadway Standard Specification Codes*, Korea Roadway Transportation Association (KRTA), Ministry of Land, Transport and Maritime Affairs, 2005.
- [17] W. Prachasaree, P. Sookmanee, S. Limkatanyu, and H. V. S. Gangarao, "Simplified load distribution factors for fiber reinforced polymer composite bridge decks," *Baltic Journal of Road and Bridge Engineering*, vol. 8, no. 4, pp. 271–280, 2013.
- [18] W. Prachasaree, H. V. S. Gangarao, and V. Shekar, "Performance evaluation of FRP bridge deck under shear loads," *Journal of Composite Materials*, vol. 43, no. 4, pp. 377–395, 2009.
- [19] W. Prachasaree, H. V. S. Gangarao, and V. Shekar, "Performance evaluation of FRP bridge deck component under torsion," *Journal of Bridge Engineering*, vol. 11, no. 4, Article ID 006604QBE, pp. 430–442, 2006.
- [20] ANSYS, *ANSYS Release 9.0 Documentation, Version 9.0*, Swanson Analysis Systems, 2004.
- [21] B. Wan, D. C. Rizos, M. F. Petrou, and K. A. Harries, "Computer simulations and parametric studies of GFRP bridge deck systems," *Composite Structures*, vol. 69, no. 1, pp. 103–115, 2005.
- [22] National Cooperative Highway Resaerch Program (NCHRP), *Dynamic Impact Factors for Bridges, Synthesis 266*, National Acedemy Press, Washington, DC, USA, 1998.
- [23] M. Chiewanichakorn, A. J. Aref, and S. Alampalli, "Dynamic and fatigue response of a truss bridge with fiber reinforced polymer deck," *International Journal of Fatigue*, vol. 29, no. 8, pp. 1475–1489, 2007.
- [24] C. J. Dodds and J. D. Robson, "The description of road surface roughness," *Journal of Sound and Vibration*, vol. 31, no. 2, pp. 175–183, 1973.
- [25] C. S. Jinka, *Dynamic response evaluation of fiber reinforced composite bridge decks and bridges [M.S. thesis]*, Department of Civil Engineering, West Virginia University, Morgantown, WV, USA, 2003.
- [26] S. Aluri, *Updating low-profile FRP deck FE model using experimental modal analysis [M.S. thesis]*, Department of Mechanical Engineering, West Virginia University, Morgantown, WV, USA, 2006.
- [27] B. Bakht and S. G. Pinjarkar, "Review of dynamic testing of highway bridges," *Transportation Research Record*, vol. 1223, pp. 93–100, 1989.
- [28] L. Deng, Y. Yu, Q. Zou, and C. S. Cai, "State-of-the-art review of dynamic impact factors of highway bridges," *Journal of Bridge Engineering*, vol. 20, no. 5, Article ID 04014080, 2015.
- [29] J. Li and M. Su, "The resonant vibration for asimply supported girder bridge under high-speed trains," *Journal of Sound and Vibration*, vol. 224, no. 5, pp. 897–915, 1999.
- [30] Federal Highway Administration (FHWA), *Load and Resistance Factor Design for Highway Bridges*, FHWA, Washington, DC, USA, 1995.
- [31] W. H. Walker and A. S. Veletsos, "Response of simple-span highway bridges to moving vehicles," *Bulletin Experiment Station 124*, College of Engineering, University of Illinois, Champaign, Ill, USA, 1966.